NASA Contractor Report 4640

Damage-Mitigating Control of a Reusable Rocket Engine for High Performance and Extended Life

Asok Ray and Xiaowen Dai

GRANT NAG3-1240
JANUARY 1995

National Aeronautics and
Space Administration

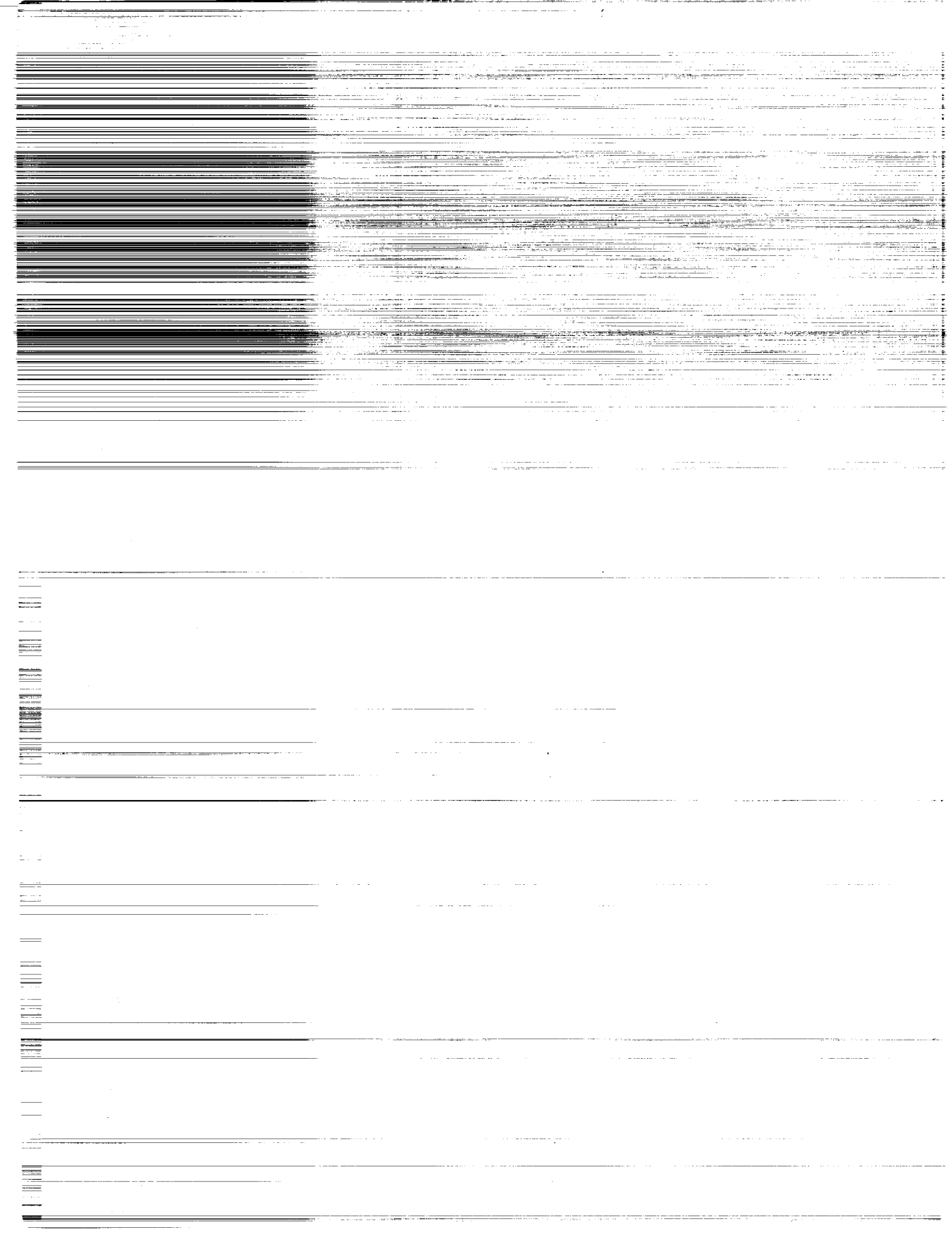

NASA Contractor Report 4640

Damage-Mitigating Control of a Reusable Rocket Engine for High Performance and Extended Life

Asok Ray and Xiaowen Dai
The Pennsylvania State University
Mechanical Engineering Department

Prepared for
Lewis Research Center
under Grant NAG3–1240

National Aeronautics and
Space Administration
Office of Management
Scientific and Technical
Information Program
1995

A Report entitled

DAMAGE-MITIGATING CONTROL OF A REUSABLE ROCKET ENGINE FOR HIGH PERFORMANCE AND EXTENDED LIFE

Prepared for

NASA Lewis Research Center
under Grant Number: NAG3-1240

by

Asok Ray and Xiaowen Dai
Mechanical Engineering Department
The Pennsylvania State University
University Park, PA 16802

Subject Terms: Life Extending Control; Damage modeling; Creep; Creep ratcheting; Fatigue; Optimization

ABSTRACT

The goal of damage mitigating control in reusable rocket engines is to achieve high performance with increased durability of mechanical structures such that functional lives of the critical components are increased. The major benefit is an increase in structural durability with no significant loss of performance. This report investigates the feasibility of damage mitigating control of reusable rocket engines. Phenomenological models of creep and thermo-mechanical fatigue damage have been formulated in the state-variable setting such that these models can be combined with the plant model of a reusable rocket engine, such as the Space Shuttle Main Engine (SSME), for synthesizing an optimal control policy. Specifically, a creep damage model of the main thrust chamber wall is analytically derived based on the theories of sandwich beam and viscoplasticity. This model characterizes progressive bulging-out and incremental thinning of the coolant channel ligament leading to its eventual failure by tensile rupture. The objective is to generate a closed form solution of the wall thin-out phenomenon in real time where the ligament geometry is continuously updated to account for the resulting deformation. The results are in agreement with those obtained from the finite element analyses and experimental observation for both Oxygen Free High Conductivity (OFHC) copper and a copper-zirconium-silver alloy called NARloy-Z. Due to its computational efficiency, this damage model is suitable for on-line applications of life prediction and damage mitigating control, and also permits parametric studies for off-line synthesis of damage mitigating control systems. The results are presented to demonstrate the potential of life extension of reusable rocket engines via damage mitigating control. The control system has also been simulated on a testbed to observe how the damage at different critical points can be traded off without any significant loss of engine performance. The research work reported here is built upon concepts derived from the disciplines of Controls, Thermo-Fluids, Structures, and Materials. The concept of damage mitigation, as presented in this report, is not restricted to control of rocket engines. It can be applied to any system where structural durability is an important issue.

TABLE OF CONTENTS

LIST OF TABLES

LIST OF FIGURES

NOMENCLATURE

English

A	area or valve position, cross sectional area, constant in viscoplastic model
a	deviatoric back stress
a_{11}, b_{11}, d_{11}	coefficients in stiffness matrix
b, c	constant in fatigue damage model
B	back stress
C	constant, constant in fatigue damage model
C_p	constant pressure specific heat
C_v	constant volume specific heat
d	thickness of the core of sandwich beam
d_1, d_2	distance between the centroids of the thin faces to the beam mid-plane in the sandwich beam model
D	diameter, damage measure, drag stress
D_0	material constant
E	Young's modulus
f	friction coefficient
F	function in viscoplastic model
g	gravity
G G_0	function or material constant in viscoplastic model
h	inelastic material constant
h_c	convective heat transfer coefficient
H	enthalpy, inelastic material constant
H_{PMP}	pump head
Head	pump pressure head
I	moment of inertia
I_2	square of ℓ_2 norm of the deviatoric back stress
J_2	square of ℓ_2 norm of the effective stress
k	specific heat ratio, heat conductivity, Boltzmann constant
K, K_0	function or material constant in viscoplastic model
K'	material parameter in fatigue damage model
l	half length of the beam
l, m, n, p, r,	dimension s of vectors and matrices
L	length, limiting value of the back stress
m	material parameters
M	Mach number, bending moment,
M, R, Q, S	weighting matrices
n, n'	material parameters
N	tensional force, total number of steps in the optimization problem
MR	O_2 / H_2 mixture ratio
p	distributed force per unit length
P	pressure

$\mathbf{q}$	structural output vector of the structural model
Q	volume flow rate, activity energy
Q_h	heat flux rate
r	recovery function in the viscoplastic model
R	characteristic gas constant
RA	effective area ratio
S	turbopump speed, deviatoric stress, material constant
t	time
T	absolute temperature
u	axial displacement
$\mathbf{u}$	input vector of the plant model
v	velocity
$\mathbf{v}$	damage state vector
V	power, volume
W	mass flow rate
w	mid-plane radial deflection, weight in fatigue damage model
x, y, z	Cartesian coordinate
$\mathbf{x}$	state vector of the plant model
X	torque
$\mathbf{y}$	output vector of the plant model
Z	Zener- Hollomom parameter

Greek

α	coefficient of thermal expansion, back stress
α	natural upper bound of the valve position
β	damage rate constraint vector
β	material parameter
δ	damage, linear fatigue damage
δ_1, δ_2	radial deflection of the two faces of the ligament
ε	normal strain
γ	parameter in nonlinear fatigue damage model
Φ	function
ϕ	curvature angle in the sandwich beam
η	efficiency, dummy variable in the integration
κ	mid-plane curvature
θ	thickness of each face in the sandwich beam
Θ	thermal diffusivity function,
ϑ	actual thickness of the coolant channel ligament
ρ	density
$\bar{\rho}$	averaged density
Γ	damage accumulation constraint vector
σ	stress
Σ	effective stress

τ	thinning of the ligament, shear stress, torque, time constant
υ	velocity of the fluid
Ω	angular speed of the turbopump shaft
ξ	dummy variable in the integration
ΔP_{PMP}	pump pressure rise

Subscript

1	coolant side surface of the coolant channel ligament
2	hot-gas side surface of the coolant channel ligament
a	amplitude, ambient
B	close-out wall
c	accumulated damage
Creep	creep damage on the main thrust chamber
e	exit section, elastic part
f	final point, fluid
g	gas
gw	gas to wall
H_2	H_2 turbine fatigue damage
ideal	for ideal gas
in	inlet
k	instant of time
m	mean value, melting point
N	final state in the discretized setting of the optimization problem
o	initial value, reference point, reaction load
out	outlet
O_2	O_2 turbine fatigue damage
p	plastic part
r	reference point, damage rate
ref	reference point
ss	steady state
t	throat section
w1	hot-side wall
w2	cold-side wall
w	wall
wf	wall to fluid (coolant)
ww	wall to wall

Superscript

E	equivalent sandwich beam model
e	elastic part
o	mid-plane
R	rectangular beam model
p	plastic part
th	thermal part

CHAPTER 1

INTRODUCTION

The concept of Damage Mitigating Control (DMC), also known as life extending control (Lorenzo and Merrill, 1991a), has been recently introduced by Ray et al. (1994a, 1994b), and Ray and Wu (1994a) for structural durability of complex thermo-mechanical systems such as spacecraft, aircraft, and power plants. The key idea of this DMC concept is extension of the service life of critical plant components while simultaneously maximizing the plant performance. Potential benefits of DMC include the following:

- Plant performance enhancement without overstraining the mechanical structures;
- Life extension of the plant with increased reliability, availability and durability;
- Reduction of plant operational cost via predictive maintenance and diagnostics;
- Risk reduction in the integrated control-structure-materials systems design.

However, the traditional approach to decision and control systems synthesis for thermo-mechanical systems, which is often based upon the assumption of invariant damage characteristics of materials, may lead to either of the following events:

- Less than achievable performance due to overly conservative design;
- Unexpected failures and drastic reduction of the useful life span due to over-straining of mechanical structures.

For example, the original design goal of the Space Shuttle Main Engine (SSME) was specified for 55 flights before any major maintenance, but the current practice is to disassemble the engine after each flight for maintenance (Lorenzo and Merrill, 1991b). A major concern in the control systems design and plant operations is to assure reliable and satisfactory long term performance. From these perspectives, damage mitigating control systems need to be synthesized by taking performance, mission objectives, service life, and maintenance and operational costs into consideration in order to achieve high performance and extended service life. A major goal of the control system is then to achieve an optimum trade-off between performance and structural durability of the critical plant components. The challenge here is to characterize the thermo-mechanical behavior of structural materials for life prediction in conjunction with dynamic performance analysis of the thermo-fluid process, and then utilize this information in a mathematically and computationally tractable form for synthesizing algorithms of robust control, diagnostics and prognostics, and risk assessment in complex mechanical systems.

Although a significant amount of research has been conducted in each of the individual areas of structural and thermo-fluid analysis, life prediction of materials, and synthesis of decision and control systems, integration of these disciplines for optimal design of complex thermo-mechanical systems has not apparently received much attention. As the science and technology of materials continue to evolve, methodologies for analysis and design of thermo-mechanical systems must have the capability of easily incorporating an appropriate representation of material properties, structural behavior, and thermo-fluid dynamics in the control systems analysis and synthesis procedure. In view of integrated structural and flight control of advanced aircraft, Noll et al. (1991) have pointed out the need for interdisciplinary research in the fields of active control technology and structural integrity, specifically fatigue life assessment and aero-servo-elasticity. This report attempts to formulate a unified methodology for damage mitigating control systems synthesis for reusable rocket engines such as the SSME. However, this concept of damage mitigation is not restricted to reusable rocket engines; it can be applied to any system where structural durability is an important issue.

1.1 Literature Review

This section presents the literature review for each of the following interdisciplinary research areas, namely, thermo-fluid dynamic modeling of rocket engines including the SSME, structural and damage modeling of the main thrust chamber, and synthesis of damage mitigating control systems.

1.1.1 Dynamic Modeling of a Reusable Rocket Engine

Finite-dimensional modeling has been recognized as a valuable tool for predicting dynamic performance of complex thermo-mechanical systems such as rocket engines, turbojet or turbofan engines, and electric power plants at a macroscopic level. For complex process dynamics, it is important to have a plant model which is computationally tractable and predicts transient performance with sufficient accuracy for the purpose of control systems synthesis. Both wide-range nonlinear models and piece-wise linear models are useful for different applications.

A nonlinear model representing the dynamic characteristics of the Space Shuttle Main Engine (SSME) has been developed by Rockwell (1989). Due to its size and complexity, however, this nonlinear model is not readily adaptable for synthesis of control and diagnostics systems. Linear dynamic models of the SSME at several different operating points were generated by Duyar et al (1990, 1991) using system identification techniques. However, applications of piece-wise linear models are limited in the sense that these models are only accurate in the vicinity of the operating points. The interpolation or extrapolation away from these operating points may yield unacceptable inaccuracy and possible discontinuity leading to performance degradation or instability of the control system.

To circumvent the difficulties of the above two approaches, namely, complexity of a high order nonlinear model and the narrow operating range of a linear model, a reduced order nonlinear model of a reusable rocket engine is formulated to synthesize a damage mitigating control system. This model is computationally less complex than the high order nonlinear model of Rockwell (1981) and yet remains valid over the operating conditions of 1200 psi to 3000 psi of the main thrust chamber pressure. The model equations and the underlying assumptions for major components of the rocket engine are presented in Chapter 2.

1.1.2 Structural and Damage Modeling of Reusable Rocket Engines

The critical components, under consideration, of a rocket engine such as the SSME are the fuel and oxidizer turbine blades and the main thrust chamber coolant walls. A literature review on fatigue failure of turbine blades is presented in the earler NASA report (Ray and Wu, 1994a). In this section, only the literature pertinent to life prediction of the main thrust chamber is reviewed.

1.1.2.1 Life Prediction of the Main Thrust Chamber

Hannum et al. (1976) conducted a test program including 13 rocket combustion chambers with oxygen-free high-conductivity (OFHC) copper and a copper-zirconium alloy (~99.85% Cu and ~0.1% Zr) called Amzirc. Quentmeyer (1977) investigated low-cycle thermal fatigue for 22 cylindrical rocket thrust chambers with OFHC copper, Amzirc, and a copper-zirconium-silver alloy (~96.5% Cu, ~3.0% Ag, and ~0.15% Zr) called NARloy-Z. It was revealed that the progressive deformation indicated by incremental bulging-out and thinning of the ligaments occurs before the development of a fatigue failure. This is especially true for OFHC copper during the heating and cooling processes associated with each cycle of engine operation. As thermo-mechanical loading cycles continue, the inelastic ratcheting strains induce incremental bulging-out and progressive thinning of the ligament down to the critical value, and eventually lead to failure by tensile rupture. Both Hannum et al. (1976) and Quentmeyer (1977) identified the prime cause of coolant wall failures to be the creep rupture enhanced by ratcheting. In their opinion, fatigue is not the dominant mechanism for ligament failure.

1.1.2.2 Structural Modeling of the Main Thrust Chamber

For the purpose of damage mitigating control, the basic requirements of the structural and damage model of the main thrust chamber ligament are:

- Numerical efficiency of the model;
- Continuity of the time derivative of the damage with respect to time.

Nonlinear finite element approaches have been reported in literature for analyzing inelastic structures of complex geometry such as the coolant channel ligament under cyclic loading. Armstrong (1979, 1981) reported inelastic structural analysis of three cylindrical thrust chambers, constructed from different copper alloys using a nonlinear finite element analysis method. Kasper (1984) presented structural analysis and life prediction of the coolant channel ligament, made of NARloy-Z, for a typical mission of the SSME. In these studies, a structural model based on inelastic nonlinear finite element analysis was used to determine the cumulative plastic deformation leading to thin-out and tensile rupture. The results indicated that the cyclic creep phenomenon is significantly accelerated at elevated temperatures. However, for the purpose of damage mitigating control and on-line life prediction of reusable rocket engines, the finite element approach is not practicable because of the exceptionally large requirements of computational resources.

An attempt was made by Porowski et al. (1985) to formulate a structural model of the coolant channel ligament as a rectangular beam for life prediction of the main thrust chamber. In this model, the incremental bulging-out and progressive thinning at the center of the coolant channel ligament were approximately calculated based on the elasto-plasticity theory which does not account for the interactions between creep and plasticity. Although this approach permits approximate life prediction of the thrust chamber coolant channel ligament at the end of each complete firing cycle, it can not provide the incremental bulging-out and thinning of the ligament at each instant of time within a firing cycle, which is necessary for damage mitigating control [Ray et al., 1994c].

Since the above approaches do not satisfy the requirements for damage mitigating control of reusable rocket engines, it is necessary to develop a new structural and damage model for the main thrust chamber ligament such that this model is suitable for control and on-line life prediction. The proposed analytical model is built upon the concepts of sandwich beam approximation (Robinson and Arnold, 1990) and viscoplasticity (Freed, 1988), and is capable of representing the phenomenological effects of inelastic strain ratcheting, progressive bulging-out and incremental thinning in the coolant channel ligament. The proposed model also considered progressive changes in the ligament geometry and the nonlinear effects of creep and plasticity interactions which are important for calculation of inelastic stress-strain relations and also for life prediction. A major feature of this structural and life prediction model of the coolant channel ligament is its numerical efficiency, which allows real-time damage monitoring and control.

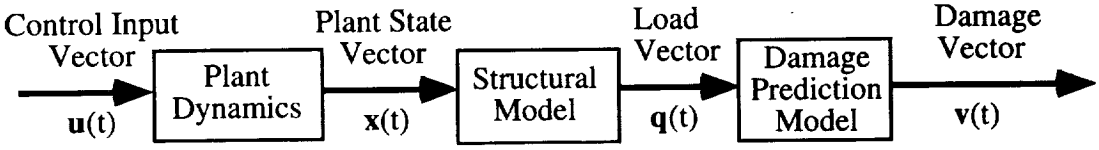

Figure 1.1 The damage prediction system

1.1.3 The Damage Mitigating Control System

The motivation and concept of damage mitigating control have been introduced by Ray et al. (1994c, 1994d). Fig. 1.1 shows a conceptual view of the damage prediction system, which is an essential ingredient of the damage mitigating control system. The plant states are inputs to the structural model which, in turn, generates the necessary information for the damage model. The

damage model is constructed in continuous-time such that the process and damage dynamics can be simultaneously incorporated within the framework of the control system in the state-variable setting. A major objective is to quantitatively evaluate the effects of damage rate and damage accumulation on structural durability under time-dependent thermo-mechanical loading. The damage state vector $\mathbf{v}(t)$ indicates, for example, the level of creep and fatigue damage accumulation at one or more critical points, and its time derivative $\dot{\mathbf{v}}(t)$ indicates how the instantaneous load is affecting the structural components (Ray and Wu, 1994b).

1.2 Objectives and Synopsis of the Report

The discussions above evince the need for interdisciplinary research in the fields of thermo-fluid dynamics, structural dynamics, thermo-mechanical fatigue and creep, and robust control and decision for enhancement of structural durability and performance of rocket propulsion systems (Ray et al., 1994d). Fig. 1.2 shows a schematic representation of a damage mitigating control system which is constructed by integrating the above four interacting disciplines to achieve optimized trade-off between the system performance and structural durability of a reusable rocket engine . The procedure for synthesizing a damage mitigating control system for rocket engines is partitioned into the following four tasks:

Task 1: Modeling of the process dynamics of the rocket engine for control system synthesis and damage evaluation;

Task 2: Modeling of the structural dynamics and damage dynamics of the critical components such as blades of the fuel and oxidizer turbines and the coolant channel ligament in the main thrust chamber;

Task 3: Analysis and synthesis of a feedforward control policy for open loop control of up-thrust transients of the rocket engine;

Task 4: Analysis and synthesis of a feedback control to track the desired open loop trajectory.

The model formulation in Task 1 and Task 2 involves thermal-fluid-structure-materials systems interactions and must satisfy the following two criteria:

- The model must be sufficiently accurate for damage prediction, plant performance analysis, and control systems synthesis;
- The governing equations must be mathematically and computationally tractable to generate feasible solutions for integrated systems optimization.

In essence, the model must be accurate and numerically efficient for systems analysis and control synthesis and, at the same time, provide the necessary information for life prediction and plant performance evaluation. Task 3 optimizes the plant dynamic performance while maintaining the damage of critical components of the rocket engine within the prescribed limits. Task 4 compensates for external disturbances and uncertainties in modeling of plant dynamics and damage dynamics.

The research work in this report focuses on the first three tasks in which a damage mitigating control methodology has been formulated for structural durability and performance enhancement of reusable rocket engines such as the SSME. A unique feature of the proposed damage mitigating control is that a substantial gain in service life and maintenance cost can be achieved with no significant reduction in engine performance. The trade-off between service life and performance is obtained by integrating the plant model with the damage model which provides the fatigue/creep damage information for control analysis and synthesis.

A finite-dimensional state-space model of the thermo-fluid propulsion dynamics has been formulated based on the fundamental principles of fluid flow and thermodynamics. The critical plant components that are prone to failure include the fuel and oxidizer turbine blades, and the main thrust chamber coolant wall. Inputs to the structural models are time-dependent plant

variables such as turbopump rotational speed and torque, main thrust chamber pressure and coolant wall temperature. The output of the structural model is the load vector which may consist of time-dependent variables such as stress and strain at the critical components, namely, blades of the fuel and oxidizer turbines and the coolant channel ligament in the main thrust chamber. The structural model of the coolant channel ligament captures the thermo-elastic-viscoplastic material behavior under both temperature and pressure variations in the main thrust chamber. The creep damage in the coolant wall is predicted based on the bulging-out and progressive thinning phenomena due to creep ratcheting and plastic strain. Based on the integrated model of plant, structural and damage dynamics, an optimal open loop control policy is synthesized in the feedforward control module via nonlinear programming for given user specified damage constraints on the critical components. Synthesis of a robust feedback control law is being pursued as an ongoing effort and is not addressed in this report. However, all four aspects of the damage mitigating control shown in Fig. 1.2 have been simulated on a multi-computer testbed to demonstrate feasibility of the proposed damage mitigating control concept for reusable rocket engines.

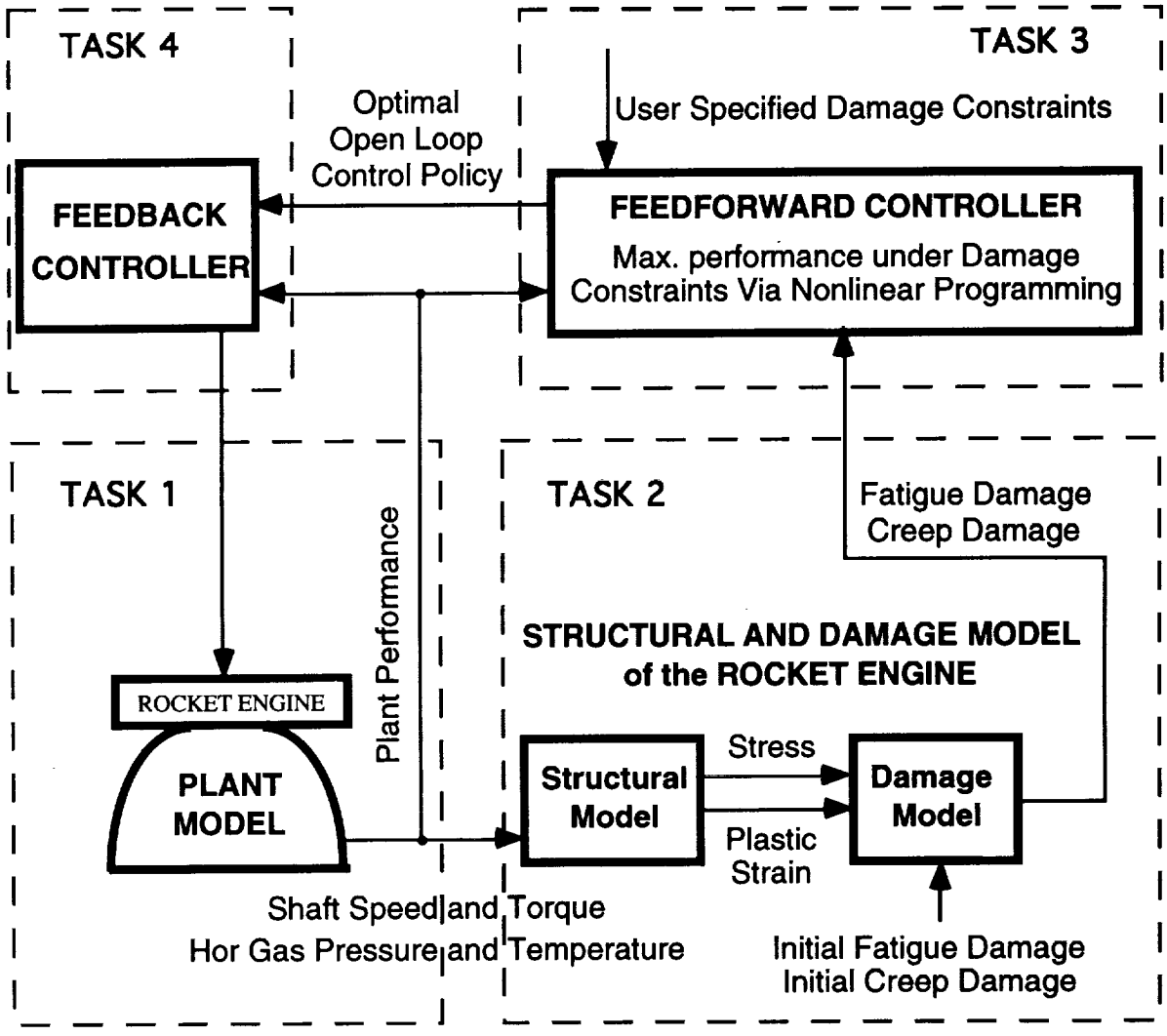

Figure 1.2 Schematic diagram of the damage mitigating control system

1.3 Contributions of the Reported Research Work

This report presents a unified methodology for damage mitigating control systems analysis and synthesis where the objective is to achieve optimized trade-off between the system performance and structural durability of reusable rocket engines such as the SSME. The proposed methodology integrates the disciplines of thermo-fluid dynamics, mechanical structures, and mechanics of materials along with control and optimization of dynamic systems.

The major contribution of this report is the formulation of a new structural and damage model of coolant channel ligaments of the main thrust chamber for both on-line life prediction and damage mitigating control of reusable rocket engines. The structural and damage model is developed based on the theories of sandwich beam and viscoplasticity. This structural model has proven to be numerically much more efficient than other finite element analysis models, and is of comparable accuracy. To the best of the authors' knowledge, no other structural and damage model of the main thrust chamber wall is suitable for both control systems synthesis and on-line life prediction of rocket engines.

Besides rocket engines, the proposed methodology of damage mitigation and life prediction is directly applicable to any thermo-mechanical process such as stream-electric power plants, land-based gas turbines, and aircraft engines where structural durability is a critical issue.

1.4 Organization of the Report

This report is organized into six main chapters including the introduction. Chapter 2 presents a simplified nonlinear model of the thermal-fluid dynamics of a rocket engine, similar to the SSME, which is the plant under control. The results of steady state solutions and transient responses are discussed. The first part of Chapter 3 presents a brief review of the structural model and the continuous-time fatigue damage model of the turbine blades, which are based on linear finite element analysis and nonlinear strain-life approach. In the second part of Chapter 3, a new structural and damage model of the coolant channel ligament is developed based on the theories of sandwich beam and viscoplasticity. By comparison with the nonlinear finite element analysis reported by other investigators, Chapter 4 validates the proposed structural and damage model of the coolant channel ligament for two different materials, namely, oxygen-free high-conductivity (OFHC) copper and a copper-zirconium-silver alloy called NARloy-Z. A series of parametric studies have been conducted corresponding to different design factors of the main thrust chamber coolant wall, such as ligament materials and configurations, thermo and mechanical loading, and loading cycle duration of the rocket engine. Chapter 5 discusses the procedure of the damage mitigating control synthesis, and formulates an optimal policy for feedforward control of up-thrust transients of rocket engines. Results of simulation experiments and parametric studies are presented for different damage constraints and different initial damage of the critical components. Chapter 6 summarizes and concludes the report along with the direction for future research and potential technology transfer.

CHAPTER 2

THERMO-FLUID DYNAMIC MODELING OF THE REUSABLE ROCKET ENGINE

This chapter presents a nonlinear dynamic model of the thermal-fluid dynamics in a reusable rocket engine. The purpose of this model is to represent the overall dynamic performance and component interactions with sufficient accuracy for control synthesis and damage prediction. The governing equations used in the model are based on the fundamental principles of physics as well as on the experimental data under a variety of plant operating conditions. The model is formulated in the state-variable setting via nonlinear differential equations with time-invariant coefficients.

The operating principles of the rocket engine under consideration are briefly described in Section 2.1. Section 2.2 presents the development of the nonlinear dynamic model equations using lumped parameter approximation. Section 2.3 discusses the results of simulation experiments for model evaluation where the transient responses of the plant state variables due to independent step disturbances in the control inputs are presented.

2.1 Description of the Reusable Rocket Engine

The reusable bipropellant rocket engine, under consideration in this report, is similar to the Space Shuttle Main Engine (SSME). Fig. 2.1 shows a functional diagram for operations and control of the rocket engine. The propellants, namely, liquid hydrogen and liquid oxygen, are individually pressurized by separate turbopumps. Pressurized liquid hydrogen and oxygen are pumped into individual high-pressure preburners which feed the respective turbines with fuel-rich hot gas. The exhaust gas from each turbine is mixed in the common manifold and then injected into the main combustion chamber where it burns with the oxidizer to make most efficient use of the energy liberated by combustion. The oxygen flow into each of the two preburners is independently controlled by the respective servo-valve while the valve position for oxygen flow into the main thrust chamber is held in a fixed position to derive maximum possible power from the engine. The plant outputs of interest are O_2 / H_2 mixture ratio and combustor pressure which are closely related to the rocket engine performance in terms of thrust-to-weight ratio and engine efficiency. The liquid hydrogen is used as a regenerative coolant for the walls of the combustion chamber and thrust nozzle where structural integrity is endangered by the high temperature environment. The pressurized liquid fuel is circulated through the coolant jackets to absorb the heat transferred from the hot reaction gases to the thrust chamber and nozzle walls.

2.2 Development of Plant Model Equations

Standard lumped parameter approaches have been used to model the thermo-fluid dynamics of the engine in order to approximate the partial differential equations describing mass, momentum, and energy conservation by a set of first-order differential equations with time as the independent variable. The plant model is constructed via causal interconnection of the primary subsystem models such as the main thrust chamber, preburners, turbopumps, valves, fuel and oxidizer supply headers, and regenerative cooling systems. Fig. 2.2 shows a model solution diagram (Ray, 1976 and Ray and Bowman, 1978) of the engine corresponding to the functional diagram in Fig. 2.1. Each block in Fig. 2.2 represents a physical plant component or subsystem. The governing equations for the lumped parameter model of the plant dynamics are described in the following sections. In addition to the basic assumption of the lumped parameter approach, other pertinent assumptions are stated while describing the models of the individual subsystems.

2.2.1 Fuel and Oxidizer Turbopump Subsystems

The rocket engine has two sets of turbopumps, namely, low pressure and high pressure, for each of the two propellants. A simplified representation of the dynamic characteristics of the

rocket engine is developed by lumping the low pressure and high pressure turbopumps into a single subsystem for each of the fuel and oxidizer propellants as shown in Fig. 2.1. On the oxidizer side, however, two pumps are modeled to obtain two sources of oxygen at different pressures. Model equations for the fuel and oxidizer turbopumps are given in Table 2.1 and Table 2.2, respectively.

Models of the hydraulic pump subsystems are derived based on the following assumptions:

(a) The pump head which is proportional to the difference between static pressures at the suction and discharge is derived based on the assumptions of: (i) one-dimensional steady incompressible flow with negligible heat transfer; (ii) identical fluid velocities at the suction and discharge section of the pump; and (iii) no change in potential energy

(b) The static performance of the pump is based on empirical characteristics (Rockwell, 1989) where the pump head ΔP_{PMP}, power V_{PMP}, and efficiency η_{PMP} are modeled as functions of the ratio of mass flow rate, W_{PMP}, to pump speed S:

$$\Delta P_{PMP} \propto S^2 \Phi_1(\Theta);\ V_{PMP} \propto S^2 \Phi_2(\Theta); \text{ and } \eta_{PMP} \propto S\Phi_3(\Theta) \tag{2.1}$$

where $\Theta = W_{PMP} / S$, and the functions Φ_1, Φ_2, and Φ_3 are obtained from Rockwell (1989). Therefore, the outputs of the pump model, namely, pump discharge pressure, temperature, enthalpy, and torque, can be obtained from the pump characteristics and thermodynamic state relations.

The governing equations for the turbine model are formulated under the following assumptions:

(c) The working fluid in the turbine is a perfect gas and the expansion process in the turbine is adiabatic. For the ideal frictionless process, the following relationship holds:

$$T_{in} / T_{out,ideal} = (P_{in} / P_{out})^{(k-1)/k} \tag{2.2}$$

where T is the absolute temperature, P is the pressure, the subscripts "in" and "out" respectively indicate the inlet and the outlet of the turbine, the subscript "ideal" stands for the idealized isentropic condition, and k is the ratio of the specific heats at constant pressure and temperature, which is assumed to be a constant within the operating range of turbine.

(d) No loss of pressure and enthalpy occurs between the preburner outlet and turbine inlet. That is,

$$P_{PBR} = P_{TRB,in}; \text{ and } H_{PBR} = H_{TRB,in} \tag{2.3}$$

(e) Flow through the turbine is assumed to be choked, and the kinetic energy of the fluid in the preburner chamber is negligible such that the stagnation pressure and temperature, P^* and T^*, are respectively identical to the static preburner pressure and temperature, P and T. Therefore, the mass flow rate W_{TRB} through the turbine can be expressed as:

$$W_{TRB} = C\frac{P^*_{TRB,in}}{\sqrt{T^*_{TRB,in}}} = C\frac{P^*_{PBR}}{\sqrt{T^*_{PBR}}} = C\frac{P_{PBR}}{\sqrt{T_{PBR}}} \tag{2.4}$$

where the coefficient C is calculated from the steady-state data.

(f) The turbine efficiency and the output torque are obtained from the empirical characteristics of the turbine (Rockwell, 1989) as:

$$\eta_{TRB} = \eta^{*}_{TRB}\,\Phi\left(\frac{S}{\sqrt{\Delta H_{ideal}}}\right) \tag{2.5a}$$

$$X_{TRB} = W_{TRB}\sqrt{\Delta H_{ideal}}\,\Phi\left(\frac{S}{\sqrt{\Delta H_{ideal}}}\right) \tag{2.5b}$$

where ideal (i.e., isentropic) enthalpy drop ΔH_{ideal} is given as:

$$\Delta H_{ideal} = C_p T_{in}\left(1 - \frac{T_{out,ideal}}{T_{in}}\right) = C_p T_{in}\left[1 - \left(\frac{P_{out,ideal}}{P_{in}}\right)^{\frac{k-1}{k}}\right] \tag{2.6}$$

The outputs of the fuel and oxidizer turbine models, namely, turbine pressure, temperature, enthalpy, flow rate, and output torque are obtained from thermodynamic relations as delineated in Tables 2.1 and 2.2, respectively.

The state variables in the fuel and oxidizer turbopump subsystems are respectively the shaft speeds S_{PMP} and S_{OPMP}. The power delivered by each turbine is equal to the sum of the power required by the propellant pump, and power losses in the bearings, gears, seals, and wear rings. Therefore, the dynamics of shaft speed in each turbopump are given in terms of the difference in torque as:

$$I\frac{dS}{dt} = (X_{TRB} - X_{PMP}) \tag{2.7}$$

where I is the moment of inertia and X indicates the torque.

2.2.2 Preburner Fuel and Oxidizer Supply Header Subsystems

The model equations of the preburner fuel and oxidizer supply header subsystems are listed in Table 2.3. The equations of fuel flow to each preburner are approximated to simplify the complexity of flow boundaries. The fuel flow to the two preburners accounts for the mixture of the coolant flow from the primary nozzle cooling region and the primary nozzle bypass. The governing equations of the fuel flow through the preburner header are derived under the following assumptions:

(a) The preburner fuel supply pressure P_{FPS} is proportional to the fuel flow pressure at the main fuel valve.

(b) Two coolant flows, namely, main chamber coolant flow (W_{CMBF}) and primary nozzle coolant flow (W_{NOZF}), varies in proportion to the total fuel flow (W_{PMP}). Since the coolant control valve position is held fixed, it is treated as fully open. Accordingly, the fixed nozzle bypass flow W_{FNBP} is obtained by subtracting the main chamber coolant flow and the nozzle coolant flow as:

$$W_{CMBF} = C_{CMBF} W_{PMP} \tag{2.8a}$$

$$W_{NOZF} = C_{NOZF} W_{PMP} \tag{2.8b}$$

$$W_{FNBP} = W_{PMP} - W_{CMBF} - W_{NOZF} \tag{2.8c}$$

By neglecting the dynamics due to fluid inertance in the flow passages, the above simplifications (a) and (b) reduce four differential equations of momentum conservation into four algebraic

equations. This approximation only affects the model accuracy at high frequencies because of relatively small fluid inertance.

(c) For one dimensional, incompressible uniform flow through a pipeline or valve and neglecting the body force, the friction pressure drop through a pipeline or valve is expressed as:

$$\Delta P = f\frac{L}{D}\frac{\rho}{2}\frac{Q^2}{A^2} = C\frac{|W|W}{\rho}, \qquad C = f\frac{L}{D}\frac{1}{2A^2}, \qquad \text{for pipeline} \tag{2.9a}$$

$$\Delta P = f\frac{L}{D}\frac{\rho}{2}\frac{Q^2}{A^2} = C'\frac{|W|W}{R_A{}^2}, \quad C' = f\frac{L}{D}\frac{1}{2\rho\bar{A}^2}, \quad R_A = \frac{A}{\bar{A}} \quad \text{for valve} \tag{2.9b}$$

The state variables of the preburner fuel and oxidizer supply headers are:

- W_{HPBH} and W_{HPBO} (fuel mass flow rates into the fuel and oxidizer preburners);
- W_{OPBH} and W_{OPBO} (oxidizer mass flow rates into the fuel and oxidizer preburners).

The derivatives of the above four state variables are obtained from conservation of linear momentum over a control volume of a pipeline,

$$\frac{d}{dt}(W) = C_f(P_{in} - P_{out} - C\frac{|W|W}{\rho}), \tag{2.10}$$

where ρ is the average fluid density and C_f is the inverse of equivalent fluid inertance.

2.2.3 Main Chamber Fuel Injector Subsystem

The fuel injector mixes the two branches of fuel-rich exhaust hot-gas from the two turbines and a small amount of fuel from the combustion chamber coolant path. Model equations for the preburners, main thrust chamber, and fuel injector are listed in Table 2.4. The governing equations of the fuel injector subsystem are derived under the following assumptions:

(a) The flow of an incompressible working fluid at a low Mach number (e.g., M< 0.3) is governed by the following relation (Blackburn et al., 1960) by assuming that the subsonic velocities exist throughout the orifices:

$$Q = \upsilon A = C_d' A\sqrt{2(P_{in} - P_{out})/\bar{\rho}} \qquad \text{(volumetric flow rate)} \tag{2.12a}$$

$$W = Q\rho = C_d\sqrt{2(P_{in} - P_{out})\bar{\rho}} \qquad \text{(mass flow rate)} \tag{2.12b}$$

where $\bar{\rho}$ is the average density which is approximated as the gas density ρ_{CMB} at the combustor.

(b) The flow into the fuel injector manifold is the sum of two turbine exhaust flows, W_{TRB} and W_{OTR}, and main combustion chamber coolant flow W_{CMBF}. The manifold pressure P_{FINJ} is derived form Eq. (2.12b) as:

$$P_{FINJ} = \frac{(W_{TRB} + W_{OTR} + W_{CMBF})^2}{C_d^2 \rho_{CMB}} + P_{CMB} \tag{2.13}$$

(c) The mixed gas temperature at the fuel injector manifold is obtained as a weighted average of the two turbine inlet temperatures, T_{PBR} and T_{OPB}, and the main chamber coolant flow temperature, T_{CMBF}. That is, $T_{FINJ} = C_0 T_{PBR} + C_1 T_{OPB} + C_2 T_{CMBF}$ where the coefficients, C_d, C_0, C_1, and C_2 are obtained from the steady-state data under normal operating conditions.

2.2.4 Oxygen Control Valve Subsystem

The nonlinearities of control valves are compensated by inducing the inverse characteristics of valves (Rockwell, 1989) in the control signal such the valve command becomes proportional to the valve area under steady-state operations. The oxygen control valve subsystem model has two state variables, namely, fuel and oxidizer preburner valve rotary positions. The dynamics of each valve are represented by a first order lag as:

$$\frac{d}{dt}(A_{RFPV}) = \frac{A_{RFPV} - U_{FPV}}{\tau_{FPV}} \tag{2.15a}$$

$$\frac{d}{dt}(A_{ROPV}) = \frac{A_{ROPV} - U_{OPV}}{\tau_{OPV}} \tag{2.15b}$$

where U_{FPV} and U_{OPV} are the commands to the oxygen control valves, and A_{RFPV} and A_{ROPV} are the effective areas of the oxidizer control valves, and τ is the time constant of the respective valve.

In solving the nonlinear optimal open loop control problem, the two commands U_{FPV} and U_{OPV} correspond to the decision variables in the nonlinear programming which are bounded above and below via specified constraints.

2.2.5 Preburner and Combustion Subsystems

The dynamic equations for the combustion process are developed by employing the principles of conservation of mass and energy with following assumptions.

(a) Conservation of momentum is satisfied by assuming that gas pressure and temperature in the combustion chamber are spatially uniform although they are time-dependent, and the kinetic energy due to gas velocity in the chamber is negligible. This assumption is valid for a low-frequency dynamic representation, and precludes the process of high-frequency acoustic propagation.

(b) One-dimensional unsteady flow in the combustion chamber is represented by a first order differential equation of the rate change of mixture gas density which is related to the mass flow into and out of the chamber via conservation of mass.

$$\frac{d}{dt}(\rho) = \frac{W_{in} - W_{out}}{V_{CMB}} \tag{2.16}$$

where V_{CMB} is the volume of the combustion chamber.

(c) The conservation of energy equation yields:

$$\frac{d}{dt}(C_V V \rho T) = \sum W_{in} H_{in} - \sum W_{out} H_{out} + F W_{O_2} - Q_{heat} \tag{2.17}$$

where F is the energy liberated by per unit mass of oxygen from a macroscopic point of view of the chemical process where the reaction dynamics is assumed to be instantaneous. Q_{heat} is the heat transfer rate from the control volume to the coolant channel wall.

(d) Based on the thermodynamic relationship of the perfect gas law, the average gas temperature in the combustion chamber is given as: $T_{CMB} = P_{CMB} / (\rho_{CMB} R)$ where R is the characteristic gas constant. Therefore, the derivative of the main chamber pressure is obtained by rewriting the energy Eq. (2.17) as:

$$\frac{d}{dt}(P_{CMB}) = (W_{FINJ}H_{FINJ} + W_{CMBO}H_{OP2E} - W_{NOZ}H_{CMB} + W_{CMBO}F - Q_{CMBW}) / (C_V V_{CMB} / R) \quad (2.18)$$

(e) The flow through the nozzle throat is choked.

The model equations of the preburner and combustor are given in Table 2.4. The six state variables in two preburners and main combustion chamber are:

- P_{PBR} and R_{PBR}: (Fuel preburner chamber gas pressure and density);
- P_{OPB} and R_{OPB}: (Oxidizer preburner chamber gas pressure and density);
- P_{CMB} and R_{CMB}: (Main thrust chamber hot gas pressure and density).

The governing equations in preburners are similar to those in the main chamber because of the similarity of the physical processes.

2.2.6 Main Thrust Chamber/Fixed Nozzle Cooling Subsystems

The basic relations governing the thrust chamber performance, such as specific impulse, combustion temperature and pressure, are calculated based on the thermodynamic principles of ideal rocket propulsion systems (Sutton, 1992). The following assumptions are used to derive the governing equations of heat transfer in the coolant channel wall.

(a) The hot-gas velocity, pressure, temperature, and density are uniform across any cross-section normal to the nozzle axis.

(b) No shock waves or discontinuities exist in the flow through the convergent-divergent nozzle, and the boundary layer effects are neglected. The energy equation applied across the nozzle throat and nozzle exit yields the exit temperature T_e as a function of the throat temperature, T_t, and exit Mach number M.

$$T_e = \left(\frac{1}{1 + \frac{k-1}{2} M^2} \right) T_t \quad (2.19)$$

where the exit Mach number M can be obtained as a function of the throat/exit pressure ratio, P_t / P_e, and throat/exit area ratio, A_t / A_e, by combining the energy and continuity equations:

$$M = \frac{1}{k-1} \left(-1 + \sqrt{(k-1)(k+1)\left(\frac{A_t}{A_e} \frac{P_t}{P_e} \right)^2 + 1} \right) \quad (2.20)$$

In the simplified model of the main thrust chamber coolant channel subsystem in Fig. 2.3, heat transfer rates and wall temperatures are derived using a lumped parameter model with two nodes. The model equations of the main chamber and nozzle regeneration cooling heat transfer subsystems are listed in Table 2.5. The heat transfer process is characterized by three different mechanisms, namely, convective heat flux from the hot gas to hot-side of the coolant wall, the conductive heat flux through the wall from the hot-side to the cold-side, and the convective heat flux from the cold-side of the wall to the liquid coolant as shown in Fig. 2.3.

(c) The conduction heat transfer rate is expressed in terms of a constant thermal conductivity of the coolant wall material and the temperature difference between the hot and cold sides as:

$$Q_{hk} = \left(\frac{kA}{L}\right)(T_{w2} - T_{w1}) \tag{2.21}$$

where k is the coefficient of thermal conductivity, and A is the area of heat transfer.

(d) Convective heat transfer is associated with the mass transfer in a fluid boundary layer over a fixed wall. In Fig. 2.3, the rates of convective heat transfer Q_{gw} and Q_{wf} are given as:

$$Q_{gw} = h_c A(T_g - T_{w2}) \qquad \text{from the hot gas to hot-side wall} \tag{2.22a}$$

$$Q_{wf} = h_c' A(T_{w1} - T_f) \qquad \text{from the cold-side wall to coolant} \tag{2.22b}$$

where h_c is the convective heat transfer coefficient, T_{w2} and T_{w1} represent hot-side and cold-side wall temperatures, respectively, and T_f represents the bulk temperature of the liquid coolant. The convective heat transfer coefficient is described as a function of the fluid mass flow rate W and other system parameters at specified operating conditions using the following empirical correlation (Rockwell, 1989):

$$h_c \propto W^{0.8} \qquad \text{from the hot gas to hot-side wall} \tag{2.23a}$$

$$h_c \propto (1 + CT_f)W^{0.8} \qquad \text{from the cold-side wall to coolant} \tag{2.23b}$$

For a thermal system composed of a material of density ρ, specific heat c_p, and a constant volume V, the energy balance equation takes the following form:

$$\rho c_p V \frac{dT}{dt} = Q_{in}(t) - Q_{out}(t) + Q_{gen}(t) + \frac{\delta Work}{dt} \tag{2.25}$$

where Q_{in} or Q_{out} is the heat flux entering or exiting the control volume, Q_{gen} is the rate of heat generated within the control volume, and $\delta Work / dt$ is the time derivative of the work done upon the control volume.

Two wall temperatures at the two nodes on the hot and cold sides of the coolant channel wall, T_{CMBW} and T_{CMBWW}, and hydrogen coolant temperature, T_{CMBWF}, are the three state variables in the heat transfer model of the thrust chamber coolant channel. In reality, these state variables correspond to wall temperatures at the throat location where the heat flux is the highest and failure is most likely to occur. In contrast, the thrust chamber nozzle is relatively less prone to failure because of lower temperature. One lumped heat transfer node with two state variables is used to model the heat transfer through the nozzle coolant channel. The five state variables in the heat transfer model of the combustion and nozzle walls are:

- T_{CMW1} and T_{CMW2} are the cold-side and hot-side temperatures of the combustor wall.
- T_{CMBWF} and T_{NOZWF}: are coolant fluid temperatures in the combustor and nozzle.
- T_{NOZW} is the average wall temperature of the nozzle.

Derivatives of wall temperatures, T_{CMW1}, T_{CMW2}, and T_{NOZW}, are obtained via Eq. (2.25) as:

$$\frac{d}{dt}(T_{CMW1}) = (Q_{CMBWW} - Q_{CMBWF}) / C_{CMBWC} \tag{2.26a}$$

$$\frac{d}{dt}(T_{CMW2}) = (Q_{CMBW} - Q_{CMBWW}) / C_{CMBWC} \tag{2.26b}$$

$$\frac{d}{dt}(T_{CMWF}) = [Q_{CMBWF} + W_{CMBF} C_{P,H_2}(T_{PMPE} - T_{CMBF})] / C_{CMBFC} \tag{2.26c}$$

The cold-side and hot-side temperatures, T_{CMW1} and T_{CMW2}, of the combustor wall are denoted as T_1 and T_2 for brevity in the creep damage model in Chapter 3.

2.3 Simulation of Transient Responses of the Rocket Engine

In the thermo-fluid-dynamic model of the rocket engine derived above, the plant state vector consists of twenty state variables, two control inputs, and ten output variables as listed below:

State Variables:

Fuel Turbopump shaft speed	Oxidizer Turbopump shaft speed
Main thrust chamber hot-gas pressure	Main thrust chamber hot-gas density
Fuel preburner oxygen flow valve position	Oxidizer preburner oxygen flow valve position
Fuel preburner hot-gas pressure	Oxidizer preburner hot-gas pressure
Fuel preburner hot-gas density	Oxidizer preburner hot-gas density
Fuel flow rate into the fuel preburner	Fuel flow rate into the oxidizer preburner
Oxygen flow rate into the fuel preburner	Oxygen flow rate into the oxidizer preburner
Hot-side coolant wall temperature	Oxidizer flow rate into the main thrust chamber
Cold-side coolant wall temperature	Nozzle cooling tube wall temperature
Main thrust chamber coolant temperature	Nozzle coolant temperature

Control Inputs:

Fuel preburner oxidizer valve position	Oxidizer preburner oxidizer valve position

Output Variables for Life Prediction and Plant Control:

Main thrust chamber pressure	(O_2 / H_2) mixture ratio
Fuel turbopump shaft speed	Oxidizer turbopump shaft speed
Fuel turbopump torque	Oxidizer turbopump torque
Hot-side coolant wall temperature	Cold-side coolant wall temperature
Main thrust chamber coolant temperature	Main thrust chamber coolant pressure

2.3.1 Steady State Response Simulation

A comparison of the steady-state data between the present nonlinear model and a more detailed model (Rockwell, 1989) is given in Table 2.6 for the engine combustion pressure of 3000 psi at the rated power level (i.e., thrust = 470,000 ℓbf). The steady-state performance data are obtained in the range of 120% to 40% of the rated main thrust chamber pressure. The model performance was found to be gradually degraded below this range. This is mainly due to the fact that the characteristics of some of the components (e.g., pump and turbine) used in the model exceed the valid range in the curve fitting or table-lookup of the experimental data.

2.3.2 Transient Response Simulation

Simulation experiments were conducted to generate a series of transients from the nonlinear dynamic model of the rocket engine for independent step disturbances in the two control input variables at the rated pressure. Figs. 2.4 to 2.12 exhibit typical results of simulation experiments to represent the dynamic responses of 25 process variables for the following three cases:

- Case A: 5% step increase in the fuel preburner oxygen valve (FPOV) area;
- Case B: 5% step increase in oxidizer preburner oxygen valve (OPOV) area;
- Case C: 5% step increase in both FPOV and OPOV areas.

Items (a), (b), and (c) correspond to the cases A, B and C in each of Figs. 2.4 to 2.12 where all parameters are normalized and expressed as the fractional deviations from the nominal operating condition. The step disturbances were applied at time t=0.05 second to display the steady state before initiating the disturbances. Dynamic responses were observed for a period of 1.0 second.

Pressure transients at the discharge of the fuel pump and two oxidizer pumps are shown in Fig. 2.4 for the three cases, in which the discharge pressures increase to higher steady-state values. However, the percentage magnitudes are different for the three different cases. Fig. 2.5 shows the dynamics of turbine torque and pump torque for both the fuel and the oxidizer turbopump subsystems. An increase in the hot-gas flow through each turbine results in a higher turbine torque and increased power for all three cases. As long as the turbine torque exceeds the pump torque, each of the turbopumps accelerates as seen from the turbopump speed transients in Fig. 2.6 and then settles down to a higher steady state value. A small initial overshoot in the transients of the oxidizer turbine torque in Fig. 2.5b for Case B is directly related to the increase of energy generated by oxidizer preburner where the turbine torque varies with the hot-gas flow rate and the turbine inlet temperature.

The dynamics of oxygen flow rate into the fuel preburner, oxidizer preburner and main thrust chamber for all three different cases of input excitation are shown in Fig. 2.7. In Fig. 2.7a, an increase in the fuel preburner valve area promptly increases the oxygen flow into the fuel preburner, which causes an increase in the fuel turbine torque. Consequently, the fuel turbopump speed increases resulting in a larger fuel flow which eventually increases the oxidizer turbine torque. Hence, oxygen flow into the oxidizer preburner is also increased although its valve area is not changed. The initial dip in oxygen flow into the main thrust chamber in Fig. 2.7a is caused by a small pressure drop in the high pressure oxidizer pump discharge as seen in Fig. 2.4a.

Pressure and temperature transients in the preburners and main thrust chamber pressure are shown in Figs. 2.8 and 2.9, respectively. Higher steady state values of the chamber pressure are related to the increased energy liberated by combustion. The small initial dip in the main combustion pressure dynamics in Fig. 2.8a is caused by the dip in oxygen flow into the main thrust chamber as seen in Fig. 2.7a. The dynamics of O_2 / H_2 mixture ratio is shown in Fig. 2.10, in which opposite trends are observed for the Case A and B. The lower steady-state value of the mixture ratio in Fig. 2.10a is due to increased fuel flow resulting from higher fuel pump discharge as seen in Fig. 2.4a. In contrast, Fig. 2.10b shows s a higher steady-state value in mixture ratio due to increased oxygen flow. The oscillations in Fig. 2.10c are a consequence of the combined dynamic effects of Case A and Case B.

Transients of heat flux through the main thrust chamber regenerative cooling channel wall, consisting of convective heat flux from the hot gas to the wall, conductive heat flux within the wall, and convective heat flux from the coolant side wall to the coolant fluid, are shown in Fig. 2.11. In each case, the fuel-rich hot-gas flow through the main thrust chamber increases causing a boost up in the heat flux through the wall. In Case A, liquid hydrogen flow increases due to increase in the speed of the fuel turbopump and therefore more energy is absorbed from the chamber wall. The initial transients show an opposite trend in Case B because the fuel flow initially decreases as a result of an increase in the fuel preburner pressure. Three temperature transients, namely, hot-side wall temperature, cold-side wall temperature, and coolant fluid temperature are presented in Fig. 2.12. A reduction in the steady-state value of all three temperatures are observed in Fig. 2.12a because more energy is absorbed due to the increased fuel flow. In contrast, a higher steady-state temperature as seen in Fig. 2.12b is due to increased heat flux generated in the combustion chamber resulting from a higher mixture ratio in the fuel-rich environment. These two opposing effects are almost balanced as seen in Fig. 2.12c.

Table 2.1 The fuel turbopump model equations

Fuel Pump Model Equations	Fuel Turbine Model Equations
$S_{PMP} = \int_0^t \dot{S}_{PMP}(t)dt + S_{PMP}(0)$	$T_{PBR} = \frac{P_{PBR}}{R_{PBR} R C_{TBU}} = T_{TRBI}$
$\dot{S}_{PMP} = (X_{TRB} - X_{PMP}) / C_{PMPMI}$	$H_{TRBI} = C_{P,PBR} T_{TRBI}$
$W_{PMP} = (1 + C_{PMPW})(W_{HPBH} + W_{OPBH})$	$G_{TRBP} = \frac{P_{TRBE}}{P_{TRBI}} = \frac{P_{FINJ}}{P_{PBR}}$
$G_{PMP} = C_{PMPG} W_{PMP} / S_{PMP}$	$T_{TRBE,ideal} = C_{TRBTI} T_{TRBI} \times (G_{TRBP})^{k-1/k}$
$G_{PMPP} = \Phi_{PMPP}(G_{PMP})$	$W_{TRB} = C_{TRBW3} \frac{P_{TRBI}}{\sqrt{T_{TRBI}}}$
$G_{PMPD} = C_{PMPP} S_{PMP}^2 G_{PMPP}$	$G_{TRBH} = \sqrt{C_{P,TRB}(T_{TRBI} - T_{TRBE,ideal})}$
$P_{PMPE} = P_{PMPS} + G_{PMPD}$	$G_{TRBX} = C_{TRBX5} \frac{S_{PMP}}{G_{TRBH}}$
$V_{PMP} = W_{PMP} G_{PMPD} / R_{PMPI}$	$X_{TRB} = C_{TRBX5} W_{TRB} G_{TRBH} \times \Phi_{TRBX}(G_{TRBX})$
$X_{PMP} = V_{PMP} / S_{PMP}$	$V_{TRB} = X_{TRB} S_{PMP}$
$G_{PMPE} = (\frac{W_{PMP}}{S_{PMP}}) / (\frac{W_{PMPR}}{S_{PMPR}})$	$G_{TRBE} = (\frac{S_{PMP}}{G_{TRBH}}) / (\frac{S_{PMPR}}{G_{TRBHR}})$
$E_{PMP} = E_{PMPR} \Phi_{PMPE}(G_{PMPE})$	$E_{TRB} = E_{TRBR} \Phi_{TRBE}(G_{TRBE})$
$H_{PMPE} = C_{P,H_2} T_{PMPS} + \frac{V_{PMP}}{W_{PMP}} (\frac{1}{\eta_{PMP}} - 1)$	$H_{TRBE} = H_{TRBI} - G_{TRBH}^2 E_{TRB}$
$T_{PMPE} = H_{PMPE} / C_{P,H_2}$	$T_{TRBE} = H_{TRBE} / C_{P,TRB}$

Table 2.2 The oxidizer turbopump model equations

Oxidizer Pump2 Model Equations	Oxidizer Pump3 Model Equations
$W_{WO} = (1 + C_{OTRIW}) \times (W_{CMBO} + W_{HPBO} + W_{OPBO})$ $G_{OP2} = C_{OP2G} W_{WO} / S_{OPMP}$ $G_{OP2P} = \Phi_{OPMPP}(G_{OP2})$ $G_{OP2D} = C_{OP2P} S_{OPMP}^2 G_{OP2P}$ $P_{OP2PE} = P_{OPMPS} + G_{OP2D}$ $G_{OP2X} = \Phi_{OP2X}(G_{OP2})$ $X_{OP2} = C_{OP2X} S_{OPMP}^2 G_{OP2X}$ $V_{OP2} = X_{OP2} S_{OPMP}$ $G_{OP2E} = (\frac{W_{WO}}{S_{OPMP}}) / (\frac{W_{WOR}}{S_{OPMPR}})$ $E_{OP2} = E_{OP2R} \Phi_{OP2E}(G_{OP2E})$ $H_{OP2E} = C_{P,O_2} T_{OPMPS} + \frac{V_{OP2}}{W_{WO}} (\frac{1}{\eta_{OP2}} - 1)$ $T_{OP2E} = H_{OP2E} / C_{P,O_2}$	$W_{OP3} = (W_{HPBO} + W_{OPBO})$ $G_{OP3} = C_{OP3G} W_{OP3} / S_{OPMP}$ $G_{OP3P} = \Phi_{OPMPP}(G_{OP3})$ $G_{OP3D} = C_{OP3P} S_{OPMP}^2 G_{OP3P}$ $P_{OP3PE} = P_{OPMPS} + G_{OP3D}$ $G_{OP3X} = \Phi_{OP3X}(G_{OP3})$ $X_{OP3} = C_{OP3X} S_{OPMP}^2 G_{OP3X}$ $V_{OP3} = X_{OP3} S_{OPMP}$ $G_{OP3E} = (\frac{W_{OPP3}}{S_{OPMP}}) / (\frac{W_{OP3R}}{S_{OPMPR}})$ $E_{OP3} = E_{OP3R} \Phi_{OP3E}(G_{OP3E})$ $H_{OP3E} = C_{P,O_2} T_{OP2E} + \frac{V_{OP3}}{W_{OP3}} (\frac{1}{\eta_{OP3}} - 1)$ $T_{OP3E} = H_{OP3E} / C_{P,O_2}$

Oxygen Turbine Model Equation	
$S_{OPMP} = \int_0^t \dot{S}_{OPMP}(t)dt + S_{OPMP}(0)$ $\dot{S}_{OPMP} = (X_{OTR} - X_{OP2} - X_{OP3}) / C_{OPMPI}$ $T_{OPB} = \frac{P_{OPB}}{R_{OPB} R C_{TBU}} = T_{OTRI}$ $H_{OTRI} = C_{P,OPB} T_{OTRI}$ $G_{OTRP} = \frac{P_{OTRE}}{P_{OTRI}} = \frac{P_{FINJ}}{P_{OPB}}$ $T_{OTRE,ideal} = C_{OTRTI} T_{OTRI} G_{OTRP}^{k-1/k}$ $W_{OTR} = C_{OTRW3} \frac{P_{OTRI}}{\sqrt{T_{OTRI}}}$	$G_{OTRH} = \sqrt{C_{P,OTR}(T_{OTRI} - T_{OTRE,ideal})}$ $G_{TRBX} = C_{TRBX4} \frac{S_{OPMP}}{G_{OTRH}}$ $X_{TRB} = C_{TRBX3} W_{OTR} G_{OTRH} \times \Phi_{OTRX}(G_{OTRX})$ $V_{TRB} = X_{TRB} S_{PMP}$ $G_{OTRE} = (\frac{S_{OPMP}}{G_{OTRH}}) / (\frac{S_{OPMPR}}{G_{OTRHR}})$ $E_{OTR} = E_{OTRR} \Phi_{OTRE}(G_{OTRE})$ $H_{OTRE} = H_{OTRI} - G_{OTRH}^2 E_{OTR}$ $T_{OTRE} = H_{OTRE} / C_{P,OTR}$

Table 2.3 Preburner fuel supply header model equations

Preburner Fuel Supply Header Model Equations	**Preburner Oxidizer Supply Header Model Equations**
$W_{HPBH} = \int_0^t \dot{W}_{HPBH}(t)dt + W_{HPBH}(0)$	$W_{HPBO} = \int_0^t \dot{W}_{HPBO}(t)dt + W_{HPBO}(0)$
$W_{OPBH} = \int_0^t \dot{W}_{OPBH}(t)dt + W_{OPBH}(0)$	$W_{OPBO} = \int_0^t \dot{W}_{OPBO}(t)dt + W_{OPBO}(0)$
	$W_{CMBO} = \int_0^t \dot{W}_{CMBO}(t)dt + W_{CMBO}(0)$
$P_{MFVD} = P_{PMPE} - C_{PMPFV}\lvert W_{PMP}\rvert W_{PMP}$	$A_{RFPV} = C_{FPVAR}A_{FPV}$
$P_{FPS} = C_{PFPS}P_{MFVD}$	$A_{ROPV} = C_{OPVAR}A_{OPV}$
$W_{CMBF} = C_{CMBF}W_{PMP}$	$A_{RMOV} = 1.0$
$W_{NOFF} = C_{NOFF}W_{PMP}$	$\dot{W}_{HPBO} = C_{HOW0}(P_{OP3PE} - P_{PBR} - C_{HOW1}\lvert W_{HPBO}\rvert W_{HPBO} - C_{HOW2}\frac{\lvert W_{HPBO}\rvert W_{HPBO}}{A_{RFPV}^2})$
$W_{FNBP} = W_{PMP} - W_{CMBF} - W_{NOZF}$	
$H_{NOZFE} = C_{P,H_2}T_{NOZF}$	
$H_{FPS} = (W_{NOZF}H_{NOZFE} + W_{FNBP}H_{PMPE}) / (W_{HPBH} + W_{OPBH})$	$\dot{W}_{OPBO} = C_{OOW0}(P_{OP3PE} - P_{OPB} - C_{OOW1}\lvert W_{OPBO}\rvert W_{OPBO} - C_{OOW2}\frac{\lvert W_{OPBO}\rvert W_{OPBO}}{A_{ROPV}^2})$
$\dot{W}_{HPBH} = C_{HHW0}(P_{PFS} - P_{PBR} - C_{HHW1}\frac{\lvert W_{HPBH}\rvert W_{HPBH}}{R_{PFS}})$	$\dot{W}_{CMBO} = C_{CMBW0}(P_{OP2PE} - P_{CMB} - C_{CMBW1}\lvert W_{HPBO}\rvert W_{HPBO} - C_{CMBW2}\frac{\lvert W_{HPBO}\rvert W_{HPBO}}{A_{RMOV}^2})$
$\dot{W}_{OPBH} = C_{OHW0}(P_{PFS} - P_{OPB} - C_{OHW1}\frac{\lvert W_{OPBH}\rvert W_{OPBH}}{R_{PFS}})$	

Table 2.4 Valve, preburner, combustion, and fixed nozzle model equations

Oxygen Control Valve Model Equations

$$A_{FPV} = \int_0^t \dot{A}_{FPV}(t)dt + A_{FPV}(0)$$
$$A_{OPV} = \int_0^t \dot{A}_{OPV}(t)dt + A_{OPV}(0)$$

$$\dot{A}_{FPV} = (U_{AFPV} - A_{FPV}) / C_{FPVA}$$
$$\dot{A}_{OPV} = (U_{AOPV} - A_{OPV}) / C_{OPVA}$$

Fuel Preburner Model Equations

$$R_{PBR} = \int_0^t \dot{R}_{PBR}(t)dt + R_{PBR}(0)$$
$$P_{PBR} = \int_0^t \dot{P}_{PBR}(t)dt + P_{PBR}(0)$$

$$\dot{R}_{PBR} = (W_{HPBH} + W_{HPBO} - W_{TRB}) / C_{PBRV}$$
$$\dot{P}_{PBR} = (W_{HPBH}H_{MIX} + W_{HPBO}H_{OP3E} - W_{TRB}H_{TRBI} + W_{HPBO}C_{PBRF}) / C_{PBRL}$$

Oxidizer Preburner Model Equations

$$R_{OPB} = \int_0^t \dot{R}_{OPB}(t)dt + R_{OPB}(0)$$
$$P_{OPB} = \int_0^t \dot{P}_{OPB}(t)dt + P_{OPB}(0)$$

$$\dot{R}_{OPB} = (W_{OPBH} + W_{OPBO} - W_{TRB}) / C_{OPBV}$$
$$\dot{P}_{OPB} = (W_{OPBH}H_{MIX} + W_{OPBO}H_{OP3E} - W_{OTR}H_{OTRI} + W_{OPBO}C_{OPBF}) / C_{OPBL}$$

Main Combustion Model Equations

$$R_{CMB} = \int_0^t \dot{R}_{CMB}(t)dt + R_{CMB}(0)$$
$$P_{CMB} = \int_0^t \dot{P}_{CMB}(t)dt + P_{CMB}(0)$$
$$T_{CMB} = \frac{P_{CMB}}{R_{CMB}CR_{CMB}C_{TBU}}$$
$$H_{CMB} = C_{P,CMB}T_{CMB}$$
$$MR = \frac{W_{CMBO} + W_{OP3}}{W_{PMP}}$$
$$\dot{R}_{CMB} = (W_{FINJ} + W_{CMBO} - W_{NOZ}) / C_{CMBV}$$
$$\dot{P}_{CMB} = (W_{FINJ}H_{FINJ} + W_{CMBO}H_{OP2E} - W_{NOZ}H_{CMB} - Q_{CMBW} + W_{CMBO}C_{CMBF}) / C_{CMBL}$$

Fuel Injector Model Equations

$$P_{FINJ} = (W_{TRB} + W_{OTR} + W_{CMBF})^2 / \left(C_d^2 \rho_{CMB}\right) + P_{CMB}$$

$$T_{FINJ} = C_0T_{PBR} + C_1T_{OPB} + C_2T_{CMBF}$$
$$H_{FINJ} = C_{P,TRB}T_{FINJ}$$
$$W_{FINJ} = C_{FINJW}\frac{P_{FINJ}}{\sqrt{T_{FINJ}}}$$

Fixed Nozzle Model Equations

$$W_{NOZ} = C_{NOZW}\frac{P_{CMB}}{\sqrt{T_{CMB}}}$$
$$C_{MACH} = 1.1$$
$$T_{NOZ} = \frac{T_{CMB}}{[1 + \left(\frac{K-1}{2}\right)C_{MACH}^2]}$$

Table 2.5 Main chamber and fixed nozzle regenerative cooling model equations

Main Chamber Regenerative Cooling Model Equations	Fixed Nozzle Regenerative Cooling Model Equations
$T_{CMW1} = \int_0^t \dot{T}_{CMW1}(t)dt + T_{CMW1}(0)$ $T_{CMW2} = \int_0^t \dot{T}_{CMW2}(t)dt + T_{CMW2}(0)$ $T_{CMBF} = \int_0^t \dot{T}_{CMBF}(t)dt + T_{CMBF}(0)$ $Q_{CMBW} = C_{CMBWH}(T_{CMB} - T_{CMW2}) \times \lvert W_{CMB} \rvert^{0.8}$ $Q_{CMBWW} = C_{CMBK}(T_{CMW2} - T_{CMW1})$ $Q_{CMBWF} = C_{CMBFH}(1 + C_{CMBQ1}T_{CMBF}) \times (T_{CMW1} - T_{CMBF}) \lvert W_{CMBF} \rvert^{0.8}$ $\dot{T}_{CMW2} = (Q_{CMBW} - Q_{CMBWW}) / C_{CMBWC}$ $\dot{T}_{CMW1} = (Q_{CMBWW} - Q_{CMBWF}) / C_{CMBWC}$ $\dot{T}_{CMBF} = (Q_{CMBWF} + W_{CMBF}C_{P,H_2} \times (T_{PMPE} - T_{CMBF})) / C_{CMBFC}$	$T_{NOZW} = \int_0^t \dot{T}_{NOZW}(t)dt + T_{NOZW}(0)$ $T_{NOZF} = \int_0^t \dot{T}_{NOZF}(t)dt + T_{NOZF}(0)$ $Q_{NOZW} = C_{NOZWH}(T_{NOZ} - T_{NOZW}) \times \lvert W_{NOZ} \rvert^{0.8}$ $C_{NOZFH} = C_{NOZFH}(1 + C_{NOZQ1}T_{NOZF})$ $Q_{NOZWF} = C_{NOZFH}(T_{NOZW} - T_{NOZF}) \times \lvert W_{NOZF} \rvert^{0.8}$ $\dot{T}_{NOZW} = (Q_{NOZW} - Q_{NOZWF}) / C_{NOZWC}$ $\dot{T}_{NOZWF} = (Q_{NOZWF} + W_{NOZF}C_{P,H_2} \times (T_{PMPE} - T_{NOZF})) / C_{NOZFC}$

Table 2.6 Steady state model results

Process Variables (State Variables)	Symbol	Unit	100% Load	
			Model Results	Heat Balance
Fuel turbopump shaft speed	SPMP	rad/sec	3570.74	3577.6
Oxidizer turbopump shaft speed	SOPMP	rad/sec	2917.49	2849.4
Main thrust chamber hot-gas pressure	PCMB	psi	3000.0	3006.0
Main thrust chamber hot-gas density	RCMB	$lb/in.^3$	1.3358d-04	1.2673d-04
Fuel preburner hot-gas pressure	PPBR	psi	4831.0	4938.7
Oxidizer preburner hot-gas pressure	POPB	psi	4854.09	5003.5
Fuel preburner hot-gas density	RPBR	$lb/in.^3$	4.7846d-04	5.4478d-04
Oxidizer preburner hot-gas density	ROPB	$lb/in.^3$	6.4924d-04	6.7526d-04
Fuel flow rate into the fuel preburner	WHPBH	lb/sec	82.1055	78.18
Fuel flow rate into the oxidizer preburner	WOPBH	lb/sec	76.1259	67.78
Oxidizer flow rate into the fuel preburner	WHPBO	lb/sec	38.5659	35.1
Oxidizer flow rate into the oxidizer preburner	WOPBO	lb/sec	20.665	23.67
Oxidizer flow rate into the thrust chamber	WCMBO	lb/sec	809.656	801.77
Coolant side chamber wall temperature	TCMW1	^oR	1240.43	/
Hot-gas side chamber wall temperature	TCMW2	^oR	1457.45	/
Main thrust chamber coolant temperature	TCMBF	^oR	483.341	469.1
Coolant side nozzle wall temperature	TNOZW	^oR	1078.21	1260.0
Nozzle coolant temperature	TNOZF	^oR	433.145	466.1
Fuel preburner oxygen flow valve position	AFPV	/	0.7813	0.7812
Oxidizer preburner oxygen flow valve position	AOPV	/	0.6387	0.6388

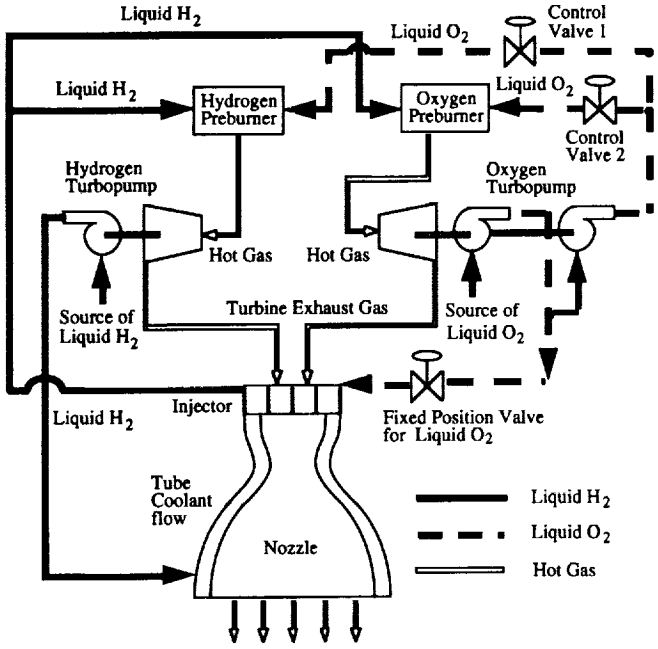

Fig. 2.1 Schematic diagram of the rocket engine

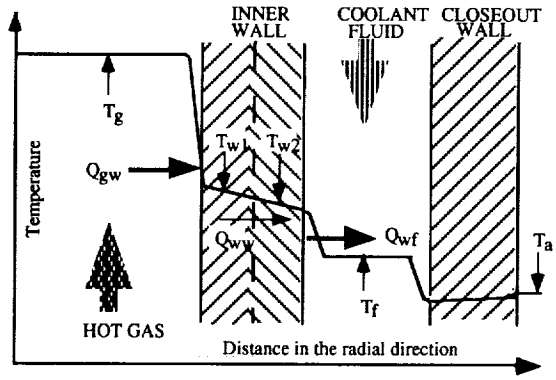

Fig 2.3 Heat transfer model of the combustor wall

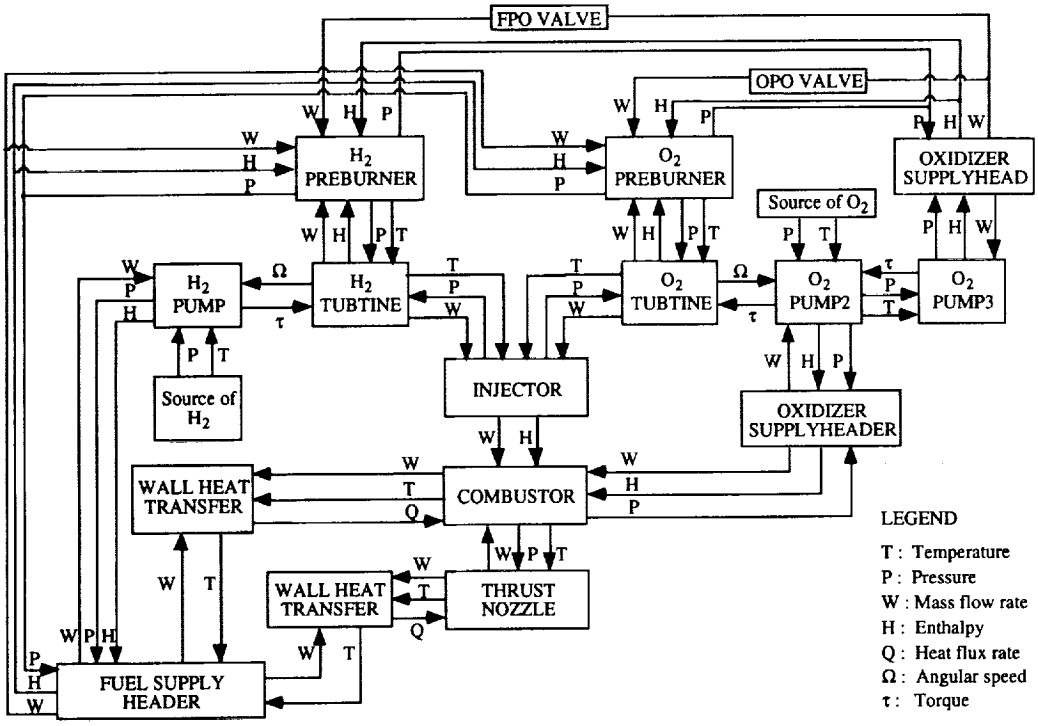

Fig. 2.2 Model solution diagram of the rocket engine

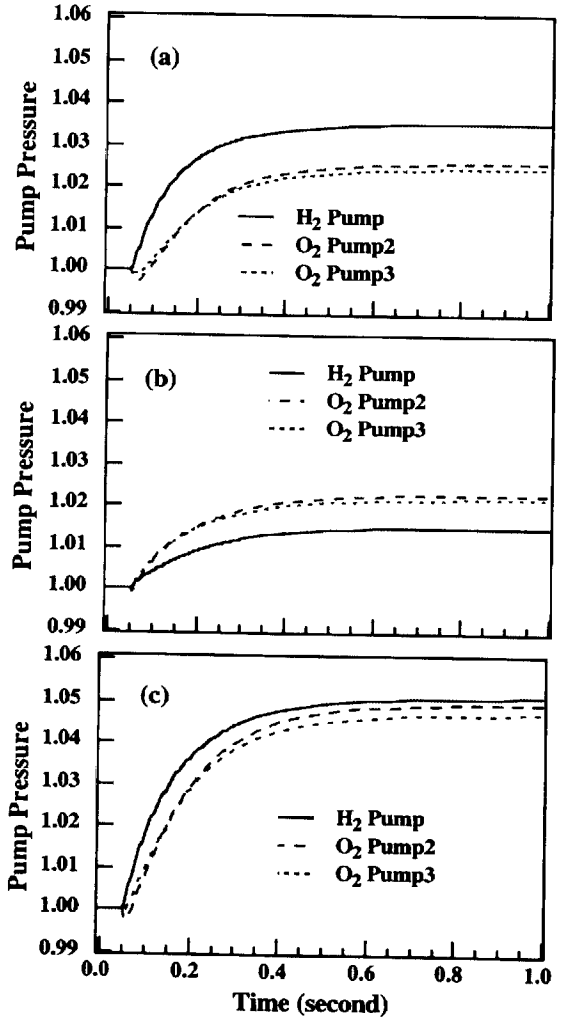

Fig. 2.4 Transients of pump discharge pressure

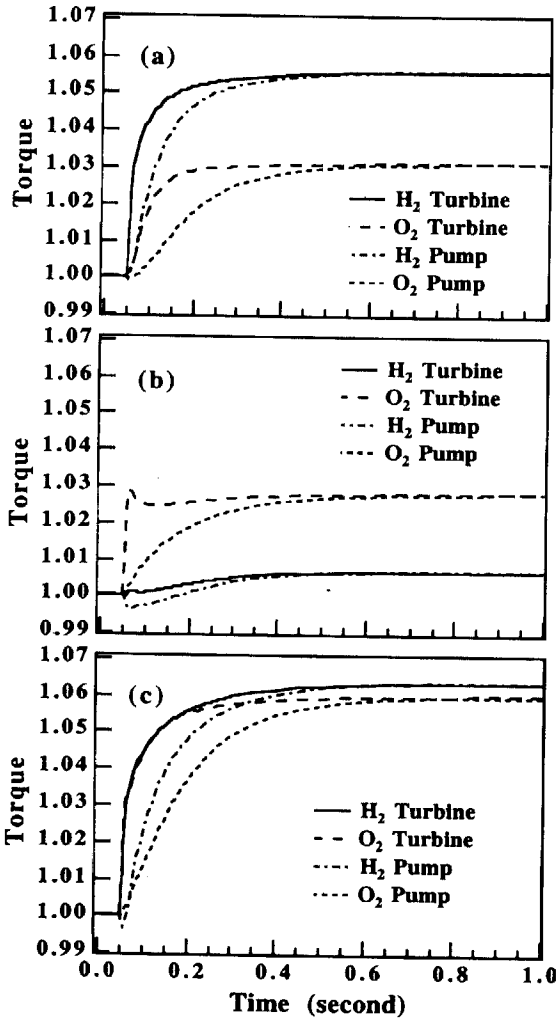

Fig. 2.5 Transients of pump/turbine torque
(a) 5% step increase in FPOV area
(b) 5% step increase in OPOV area
(c) 5% step increase in FPOV and OPOV areas

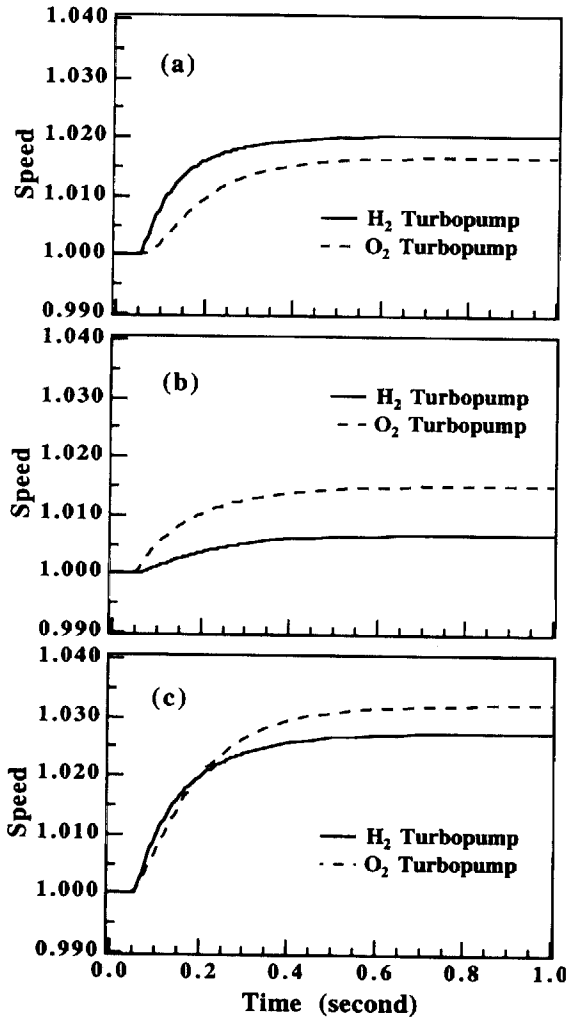

Fig. 2.6 Transients of turbopump speed

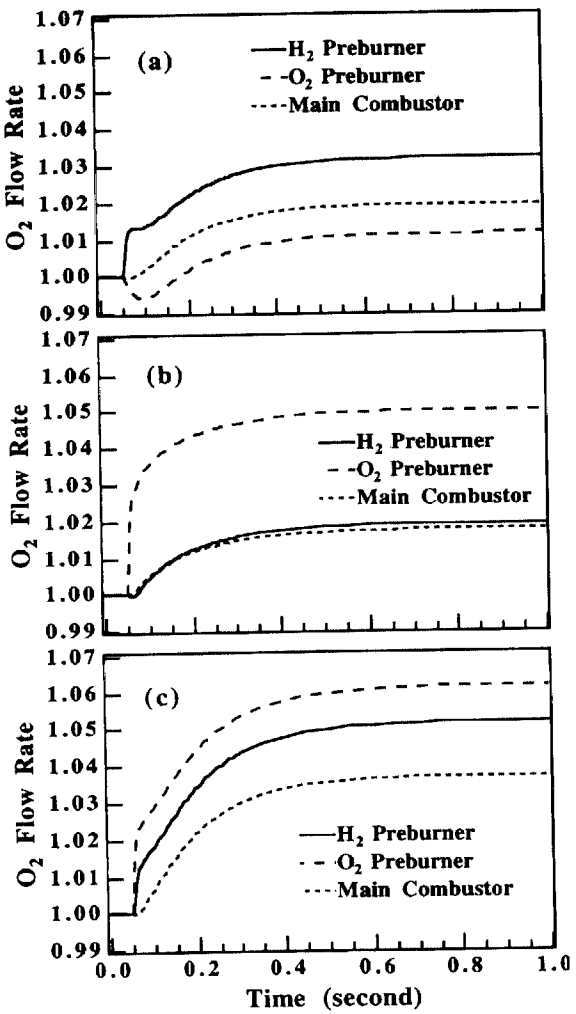

Fig. 2.7 Transient response of oxygen flow rate

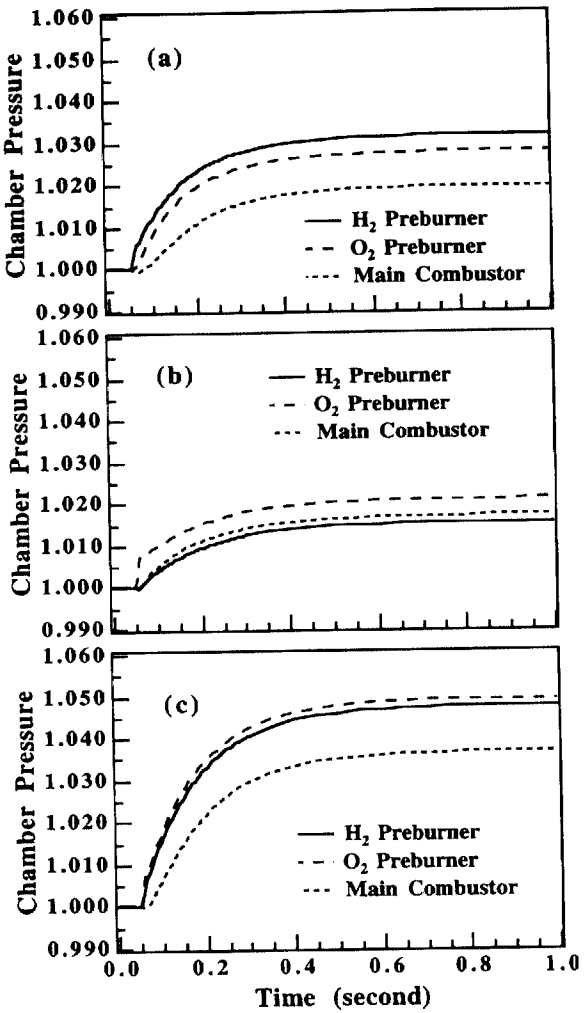

Fig. 2.8 Transient response of chamber pressure

(a) 5% step increase in FPOV area
(b) 5% step increase in OPOV area
(c) 5% step increase in FPOV and OPOV areas

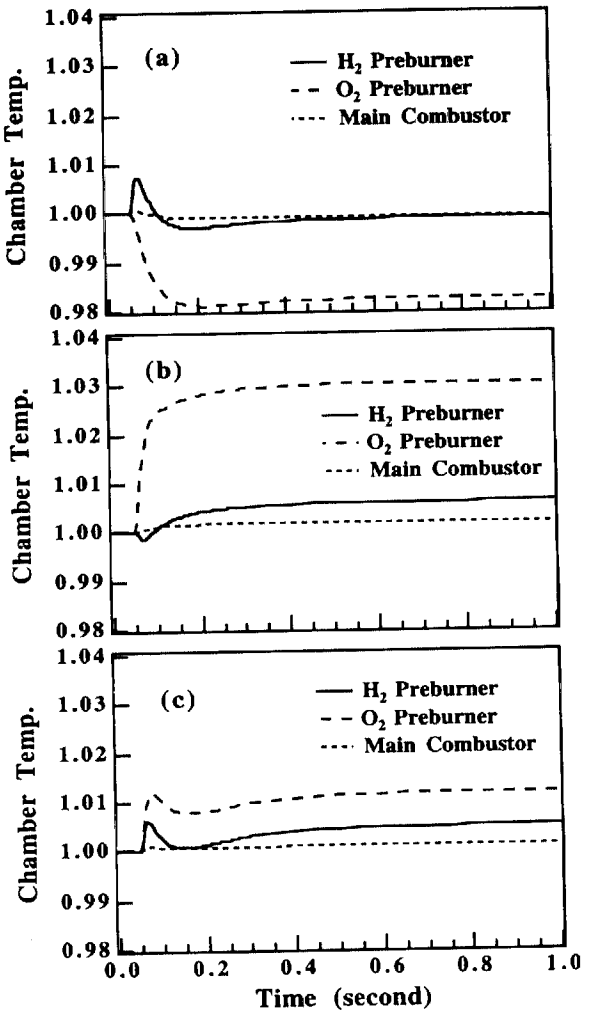

Fig. 2.9 Transient response of chamber temperature

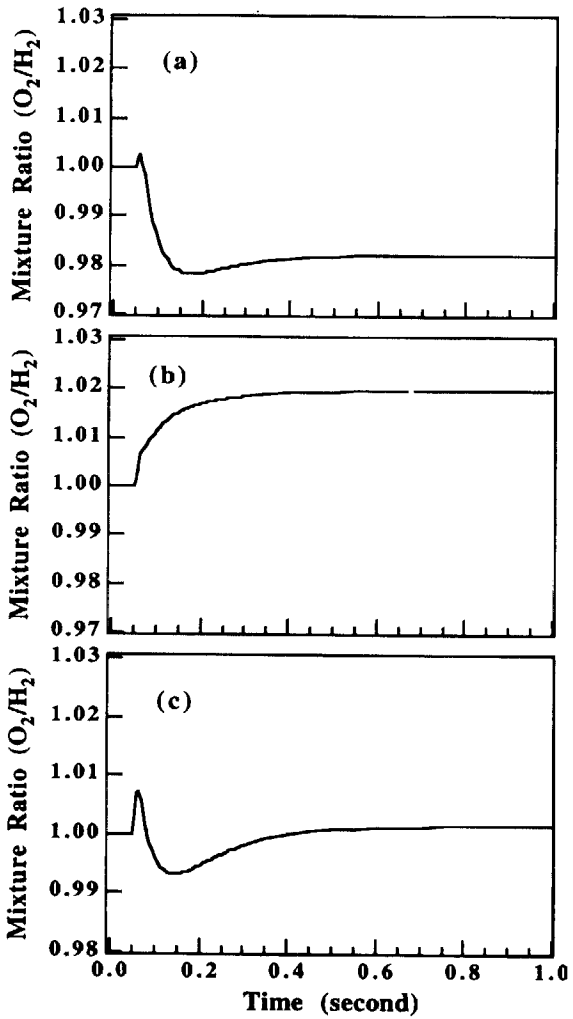

Fig. 2.10 Transientsof O_2/H2 mixture ratio

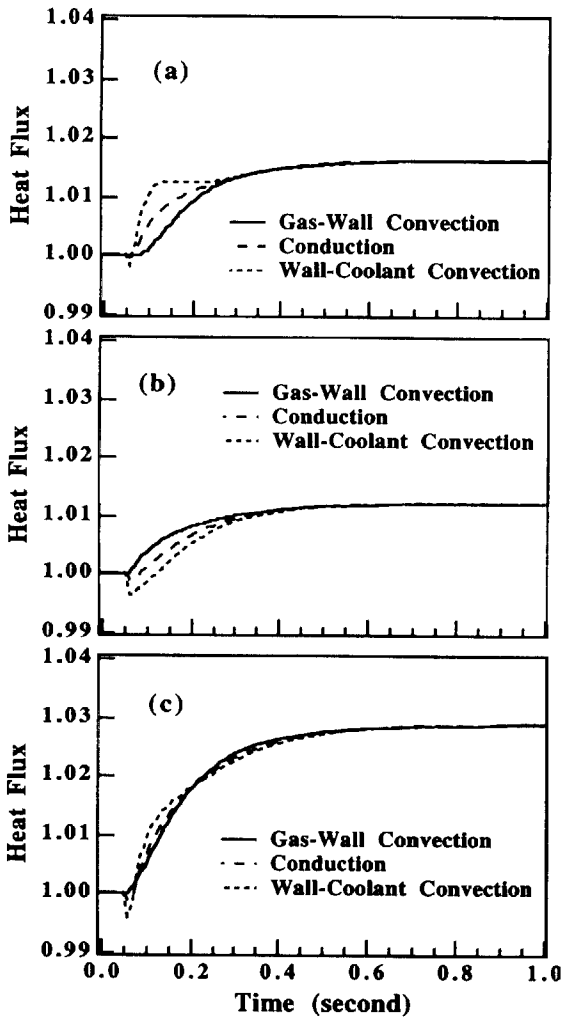

Fig. 2.11 Transient response of heat flux rate

(a) 5% step increase in FPOV area
(b) 5% step increase in OPOV area
(c) 5% step increase in FPOV and OPOV areas

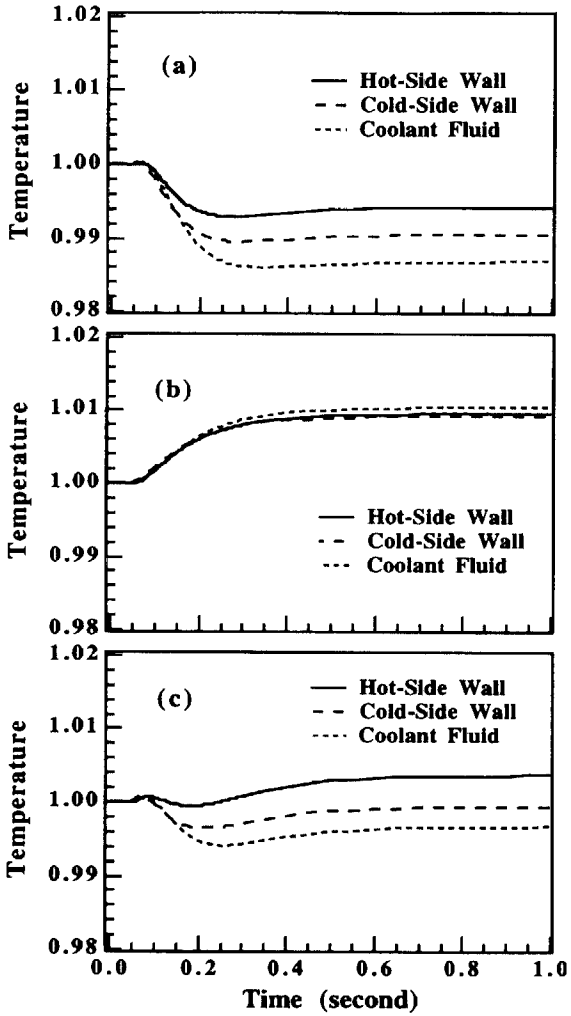

Fig. 2.12 Transients of wall/coolant temperature

CHAPTER 3

STRUCTURAL AND DAMAGE MODELS OF THE REUSABLE ROCKET ENGINE

The critical components of the reusable rocket engine under consideration, which could significantly reduce its service life, include (see Fig. 2.1):

- Blades of the fuel turbine;
- Blades of the oxidizer turbine;
- Main thrust chamber coolant channel ligaments cooled by liquid hydrogen;
- Rocket nozzle coolant channel ligaments cooled by liquid hydrogen;
- Injector tubes carrying the turbine exhaust gas into the combustion chamber.

The fatigue failure in the injector tubes, originally caused by thermal stresses, has been solved by appropriate selection of materials in the later versions of the Space Shuttle Main Engine (SSME). Therefore, the injector tube is not included as a critical point in the present study. The failure of coolant channel ligaments (i.e., walls of the coolant channel) in the main thrust chamber and rocket nozzle is caused by creep and creep ratcheting due to plasticity at high temperatures (for example, in the vicinity of 1200°R). Since the heat flux through the coolant channel ligament at the throat section of the main thrust chamber is higher than that at other sections of the nozzle, the damage control of the coolant channel ligament in the main thrust chamber is expected to protect the nozzle coolant wall. Therefore, the first three components, namely, blades of the fuel turbine, blades of the oxidizer turbine, and coolant channel ligaments at the main thrust chamber are selected as the critical points for damage mitigating control. The damage model is a representation of:

- Fatigue at the roots of the fuel and oxidizer turbine blades, and
- Creep and creep ratcheting of the coolant channel ligaments at the throat plane of the main thrust chamber.

3.1 Structural and Damage Model of the Turbine Blades

The structural model in each of the fuel and oxidizer turbines calculates the cyclic mechanical stresses at the root of a typical blade which is presumed to be a critical point in this dissertation. The blade model for each of the two turbines is represented by a three-node beam model with six degrees of freedom at each node while the first node at the root is fixed. The load on each blade model is assumed to consist of two components, namely, the (time-dependent) drive torque, and the oscillatory load on the blade as it passes each stator. It is the second component that causes high cycle fatigue at the root of the blade while the first component is largely responsible for the mean stress. The resulting stiffness matrix, mass matrix, and force vector are used to obtain a model solution for the displacements. In the last step, the stress-displacement relations from the linear elastic finite element analysis are used to predict the stresses at the critical point(s) of the blade structure.

The development of this fatigue damage model is reported in detail by Ray et al. (1994a) and Ray and Wu (1994a, 1994b) by assuming the damage rate $d\delta/dt$ is obtained as the weighted average of the elastic and plastic damage rates such that

$$\frac{d\delta}{dt} = w\frac{d\delta_e}{dt} + (1-w)\frac{d\delta_p}{dt} \tag{3.1}$$

where the weighting function, w, is selected as the ratio of the elastic strain amplitude and total strain amplitude. Since the turbine blades are subjected to loads of varying amplitude, the linear damage is modified via a nonlinear damage rule as follows:

$$D = (\delta)^{\gamma(\sigma_a, D)} \tag{3.2}$$

where D and δ are the current states of nonlinear and linear damage accumulation, respectively, and σ_a is the stress amplitude. It follows from a crack propagation model such as the Paris model (Paris and Erdogan, 1963) that the crack growth rate is dependent not only on the stress amplitude but also on the current crack length (Ray and Wu, 1994b). An approach to evaluate γ at selected discrete levels of stress amplitude by interpolation based on the experimental data of Swain et al. (1990) for the material AISI 4340 steel are reported by Ray and Wu (1994a, 1994b).

3.2 Structural Model of the Coolant Channel Ligament

The structural model of the coolant channel ligament is based on the experimental prototype of the cylindrical thrust chamber by Quentmeyer (1977), which was designed to emulate the operating conditions of the SSME. The cross-sectional dimensions of the thrust chamber configuration are geometrically similar to those of a full scale thrust chamber of the SSME even though the diameter and length of the nozzle are reduced. An enlarged view of one of the 72 coolant channels described by Quentmeyer (1977) is represented in Fig. 3.1, where the ligament connects two consecutive ribs forming the inner wall of the thrust chamber. The ligament is constructed from oxygen-free high-conductivity (OFHC) copper or a copper-zirconium-silver alloy called NARloy-Z, and the closeout wall is made of electroformed copper.

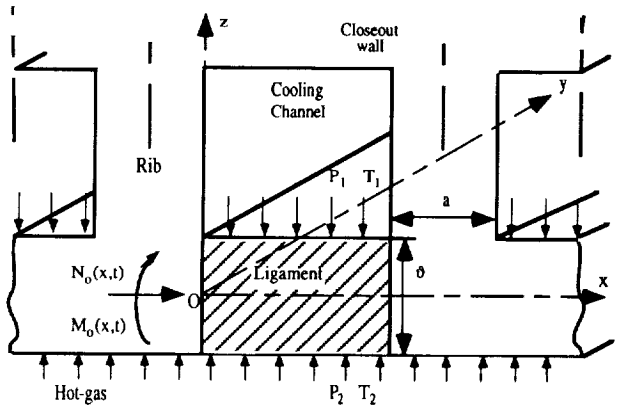

Fig. 3.1 Schematic view of a coolant channel ligament

3.2.1 Formulation of an Equivalent Sandwich Beam Model

To focus on the interactions between the structural response and temperature dependence of the coolant channel ligament, the governing equations for the structural model of the ligament are derived using Bernoulli's assumption based on the small deflection theory and by neglecting deformations due to shear. The coolant channel ligament of rectangular cross-section in Fig. 3.1 is represented by an idealized sandwich beam model (Robinson and Arnold, 1990) as seen in Fig. 3.2. The coordinates of the sandwich beam model and its loading conditions are shown in Fig. 3.2 where x, y and z coordinates correspond to the circumferential (hoop), axial, and radial directions of the ligament, and the subscripts 1 and 2 denote the cold and hot side of the ligament, respectively. The sandwich beam model (Dai and Ray, 1994a) consists of two thin faces with identical thickness θ, which are separated by an incompressible core of thickness $d_1 + d_2 - 2\theta$. Consequently, the local bending stiffness of each thin face is neglected, the normal stresses σ_1 and σ_2 are assumed to be constant throughout the faces, and the core is assumed to be rigid in shear and bear no normal stresses. The ligament is exposed to the hot gases on one surface and the liquid hydrogen coolant on the other surface. The surfaces are also

subjected to hydrostatic pressure which exerts distributed force on the wall in the radial (z) direction. The time-dependent temperature and pressure are denoted as $T_1(t)$, $P_1(t)$ on the cold-side of the ligament, and as $T_2(t)$, $P_2(t)$ on the hot-side of the ligament. The uniformly distributed force per unit length of the beam is denoted as $p(t) = [P_1(t) - P_2(t)]/(2\ell)$ in the circumferential (x) direction, where 2ℓ is the actual length of the ligament in x direction. Although the ligament temperature does not vary along the x-direction because of geometrical symmetry, there exists a temperature difference across the wall thickness in the radial (z) direction. Due to the symmetric loading and geometric configuration, only a half-beam model is considered.

For the sandwich beam structure to be equivalent to the ligament structure with rectangular cross-section in terms of identical deformation in the hoop and radial directions at the mid-plane, the parameters d_1, d_2, A_1 and A_2 (shown in Fig. 3.2) of the sandwich beam are chosen such that the cross-sectional area and moment of inertia of the rectangular beam are preserved (Arnold and Robinson, 1989) as:

$$d_1 + d_2 = d = \frac{\vartheta}{\sqrt{3}} \text{ and } A_1 = A_2 = \frac{\vartheta}{2} \text{ for unit thickness in the y-direction} \qquad (3.3)$$

where ϑ is the true thickness of the rectangular beam (i.e., the actual coolant channel ligament thickness), d_1 and d_2 are the distances from the outer fibers of the two faces to the mid-plane, A_1 and A_2 represent the cross-section areas of cold-side and hot-side of the ligament for unit length in the y-direction, respectively.

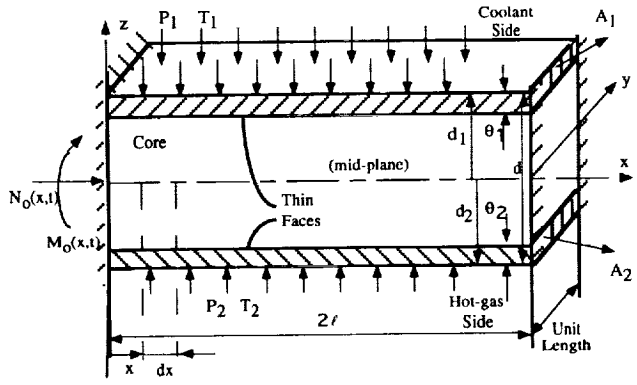

Fig. 3.2 Sandwich beam model of the coolant channel ligament

3.2.2 Kinematic Assumptions

Based on the symmetric geometry of the sandwich beam model in Fig. 3.3a, the expressions for the strain-displacement relation are as follows:

$$\varepsilon_1(x,t) = \varepsilon^o(x,t) - d_1\kappa(x,t); \quad \varepsilon_2(x,t) = \varepsilon^o(x,t) + d_2\kappa(x,t); \text{ and } w(x,t) = w^o(x,t) \qquad (3.4)$$

where $u^o(x,t)$ and $w^o(x,t)$ denote the displacement and deflection at the mid-plane z=0, respectively. The mid-plane strain ε^o and mid-plane curvature κ are defined as:

$$\varepsilon^o(x,t) = \frac{\partial u^o(x,t)}{\partial x}; \text{ and } \kappa(x,t) = -\frac{\partial^2 w(x,t)}{\partial x^2} \qquad (3.5)$$

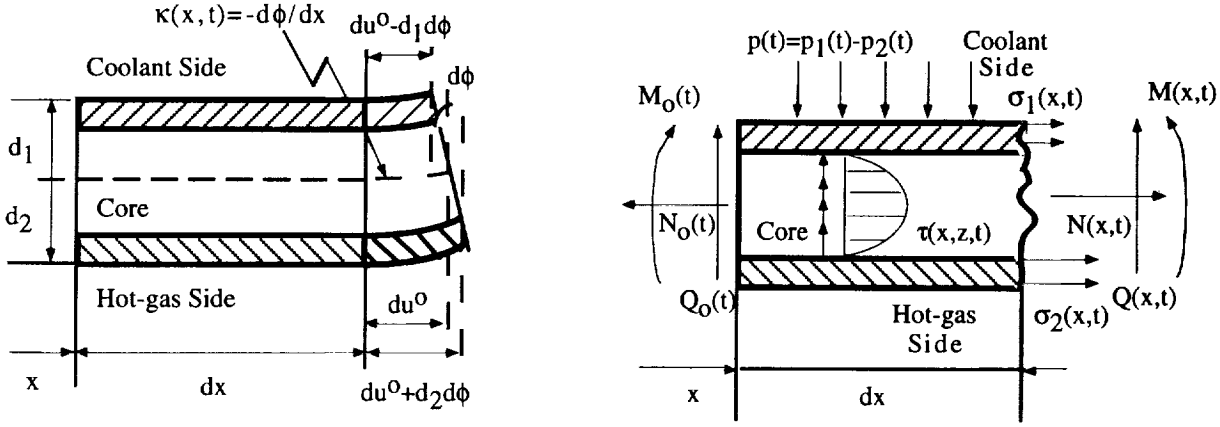

(a) displacement field (b) free body diagram

Fig. 3.3 Loading conditions on the sandwich beam model

3.2.3 Constitutive Equations

The viscoplastic theory has been adopted for modeling the nonlinear inelastic material properties at high temperatures because of its ability to represent both rate-dependent creep and rate-independent plastic behavior (Freed, 1988). The viscoplastic model serves as the constitutive law with a single kinetic equation and two types of internal state variables, namely, the tensorial anisotropic back stress and the scalar isotropic drag stress. In addition to the assumptions of small displacements and deformations, and the absence of coupling between the static and dynamic recovery terms in the viscoplastic model, the major assumptions on the two thin faces of the sandwich beam model in the present analysis are as follows:

(i) The modified version of the viscoplastic constitutive equations is presented only for the two thin faces of the sandwich beam structure where $\tau_{xz} = 0$ and $\sigma_z = 0$;

(ii) Stress components in the axial (y) direction are negligible (i.e. $\sigma_y, \tau_{xy}, \tau_{zy} = 0$);

(iii) The total strain ε_i is assumed to be the sum of elastic, inelastic, and thermal strains, ε^e, ε^p and ε^{th} on each of the cold and hot faces, i.e.,

$$\varepsilon_i(x,t) = \varepsilon_i^e(x,t) + \varepsilon_i^p(x,t) + \varepsilon_i^{th}(x,t) \qquad i = 1,2 \tag{3.6}$$

(iv) for the one-dimensional loading problem in the sandwich beam, the hoop stresses in the cold and hot faces are obtained by combining Eqs. (3.5) and (3.8) as:

$$\sigma_1 = E_1\left(\varepsilon^o - d_1\kappa\right) - E_1\varepsilon_1^p - E_1\varepsilon_1^{th} \text{ and } \sigma_2 = E_2\left(\varepsilon^o + d_2\kappa\right) - E_2\varepsilon_2^p - E_2\varepsilon_2^{th} \tag{3.7}$$

where plastic strain ε^p is obtained from the viscoplastic model as described in Section 4.4.

3.2.4 Equilibrium Equations

The stress resultants, N and M, shown in the free body diagram in Fig. 3.3b, are obtained by integrating the stress over the sandwich beam cross section as:

$$N(x,t) = \int_{-d_2}^{d_1} \sigma_z(x,z,t)dz = \sigma_1(x,t)A_1 + \sigma_2(x,t)A_2 \tag{3.8}$$

$$M(x,t) = \int_{-d_2}^{d_1} \sigma_z(x,z,t)zdz = \sigma_2(x,t)A_2d_2 - \sigma_1(x,t)A_1d_1 \tag{3.9}$$

where the hoop force N(x, t) and bending moment M(x, t) of the ligament as shown in Fig. 3.3b are obtained from the equilibrium conditions as follows:

$$N(x,t) = -N_o(t); \text{ and } M(x,t) = M_o(t) + p(t)\ell x - \frac{p(t)x^2}{2} \tag{3.10}$$

$$M(x,t) = M_o(t) + p(t)\ell x - \frac{p(t)x^2}{2} \tag{3.11}$$

The unknown reaction bending moment, M_o, and hoop force, N_o, at the junction of the ligament with the rib (i.e., at x=0) are to be determined from the boundary conditions in this statically indeterminate structure.

3.2.5 Governing Equations

Combining Eqs. (3.8), (3.9), (3.10) and (3.11), the stress and moment resultants yield the following constitutive relations for the sandwich beam in the matrix form:

$$\begin{pmatrix} N \\ M \end{pmatrix} = \begin{bmatrix} a_{11} & b_{11} \\ b_{11} & d_{11} \end{bmatrix} \begin{pmatrix} \varepsilon^o \\ \kappa \end{pmatrix} - \begin{pmatrix} N^{th} \\ M^{th} \end{pmatrix} - \begin{pmatrix} N^p \\ M^p \end{pmatrix} \tag{3.12}$$

where the extensional, flexural-extensional coupling, and bending stiffness coefficients, a_{11}, b_{11}, and d_{11} are defined as:

$$\begin{bmatrix} a_{11} \\ b_{11} \\ d_{11} \end{bmatrix} = \int_{-d_2}^{d_1} E(z) \begin{bmatrix} 1 \\ z \\ z^2 \end{bmatrix} dz = \begin{bmatrix} A_1E_1 + A_2E_2 \\ A_2d_2E_2 - A_1d_1E_1 \\ A_1d_1^2E_1 + A_2d_2^2E_2 \end{bmatrix} \tag{3.13a}$$

and the thermal and plastic "pseudo-force" and "pseudo-moment" quantities are defined as:

$$\begin{bmatrix} N^{th} \\ M^{th} \end{bmatrix} = \begin{bmatrix} A_1E_1\varepsilon_1^{th} + A_2E_2\varepsilon_2^{th} \\ A_2d_2E_2\varepsilon_2^{th} - A_1d_1E_1\varepsilon_1^{th} \end{bmatrix} \tag{3.13b}$$

$$\begin{bmatrix} N^p \\ M^p \end{bmatrix} = \begin{bmatrix} A_1E_1\varepsilon_1^p + A_2E_2\varepsilon_2^p \\ A_2d_2E_2\varepsilon_2^p - A_1d_1E_1\varepsilon_1^p \end{bmatrix} \tag{3.13c}$$

Since the temperatures at the faces 1 and 2 are significantly different (e.g., about 200°F), the elastic modules which is a function of the temperature varies in the z-direction in the event of thermo-viscoplasticity. This causes b_{11} in Eq. (3.13a) to be nonzero implying the existence of a flexural-extensional coupling effect which is similar to that in a laminated composite material.

Substitution of ε^o and κ from Eq. (3.5) into Eqs. (3.12) and (3.13), and a rearrangement yield the following pair of coupled nonlinear partial differential equations with respect to x as the independent variable:

$$\frac{\partial u^o(x,t)}{\partial x} = \frac{1}{A_1A_2E_1E_2(d_1+d_2)^2}\left[\left(A_1d_1^2E_1 + A_2d_2^2E_2\right)N(x,t) + \left(A_1d_1E_1 - A_2d_2E_2\right)M(x,t)\right] \tag{3.14a}$$
$$+\frac{d_2}{(d_1+d_2)}[\varepsilon_1^{th}(x,t)+\varepsilon_1^p(x,t)]+\frac{d_1}{(d_1+d_2)}[\varepsilon_2^{th}(x,t)+\varepsilon_2^p(x,t)]$$

$$\frac{\partial^2 w(x,t)}{\partial x^2} = \frac{-1}{A_1A_2E_1E_2(d_1+d_2)^2}\left[\left(A_1d_1E_1 - A_2d_2E_2\right)N(x,t) + \left(A_1E_1 + A_2E_2\right)M(x,t)\right] \tag{3.14b}$$
$$+\frac{1}{(d_1+d_2)}\left[d_2[\varepsilon_1^{th}(x,t)+\varepsilon_1^p(x,t)]-d_1[\varepsilon_2^{th}(x,t)+\varepsilon_2^p(x,t)]\right]$$

At a fixed instant of time, t, the above partial differential equations can be solved for known plant variables, chamber pressure, coolant pressure, and wall temperatures on both hot and cold sides, and the inelastic strains ε_1^p and ε_2^p with x as the independent variable, along with the boundary conditions derived in the next section.

3.2.6 Boundary Conditions

Five boundary conditions are needed for solving the third order differential Eqs. (3.14a) and (3.14b) with respect to x, and two unknown variables, namely, reaction moment M_o and force N_o at each instant of time t.

$$\frac{dw(x,t)}{dx} = 0, \quad \text{at } x = 0 \tag{3.15a}$$

$$\frac{dw(x,t)}{dx} = 0, \quad \text{at } x = \ell \tag{3.15b}$$

$$w(x,t) = 0, \quad \text{at } x = 0 \tag{3.15c}$$

$$u^o(x,t) = -\ell\varepsilon_B \quad \text{at } x = 0 \tag{3.15d}$$

$$u^o(x,t) = 0, \quad \text{at } x = \ell \tag{3.15e}$$

where the closeout wall strain ε_B is given as:

$$\varepsilon_B = \alpha_B T_B - \alpha_o T_o \tag{3.15f}$$

where T_B and α_B are the closeout wall temperature and linear coefficient of thermal expansion, respectively; T_o is the known reference temperature of the closeout wall; and $x = \ell$ corresponds to the center section of the ligament. Eq. (3.15d) implies that the boundary constraint is affected by the displacement of the closeout wall.

3.2.7 Closed Form Solution of the Sandwich Beam Model Equations

Applying Eq. (3.11) and the boundary conditions in Eq. (3.15) into the governing equations (3.14), the time-dependent reaction force N_o and moment M_o are obtained as:

$$N_o(t) = \frac{1}{\tilde{B}^2 - \tilde{A}\tilde{C}}\{\frac{2\tilde{B}\tilde{C}}{3}p(t)\ell^2 + \tilde{C}\tilde{I}_1^{th}(t) + \frac{\tilde{B}}{(d_1+d_2)}\tilde{I}_2^{th}(t)$$
$$-\tilde{C}\varepsilon_B(t) + \frac{\tilde{C}}{\ell}\int_0^\ell \tilde{I}_1^p(x,t)dx - \frac{\tilde{B}}{\ell(d_1+d_2)}\int_0^\ell \tilde{I}_2^p(x,t)dx\} \quad (3.16a)$$

$$M_o(t) = \frac{1}{\tilde{B}^2 - \tilde{A}\tilde{C}}\{\tilde{B}[\frac{\tilde{B}p(t)\ell^2}{3} + \tilde{I}_1^{th}(t) - \varepsilon_B(t) + \frac{1}{\ell}\int_0^\ell \tilde{I}_1^p(x,t)dx]$$
$$+\frac{\tilde{A}\tilde{C}}{3}p(t)\ell^2 + \frac{\tilde{A}}{(d_1+d_2)}\tilde{I}_2^{th}(t) - \frac{\tilde{A}}{\ell(d_1+d_2)}\int_0^\ell \tilde{I}_2^p(x,t)dx\} \quad (3.16b)$$

where

$$\tilde{A} = \frac{A_1 d_1^2 E_1 + A_2 d_2^2 E_2}{A_1 A_2 E_1 E_2 (d_1+d_2)^2} \quad (3.17a)$$

$$\tilde{B} = \frac{A_1 d_1 E_1 - A_2 d_2 E_2}{A_1 A_2 E_1 E_2 (d_1+d_2)^2} \quad (3.17b)$$

$$\tilde{C} = \frac{A_1 E_1 + A_2 E_2}{A_1 A_2 E_1 E_2 (d_1+d_2)^2} \quad (3.17c)$$

$$\tilde{I}_1^{th} = \frac{\left(d_2 \varepsilon_1^{th} + d_1 \varepsilon_2^{th}\right)}{(d_1+d_2)} \quad (3.17d)$$

$$\tilde{I}_1^p = \frac{(d_2 \varepsilon_1^p + d_1 \varepsilon_2^p)}{(d_1+d_2)} \quad (3.17e)$$

$$\tilde{I}_2^{th} = (\varepsilon_2^{th} - \varepsilon_1^{th}) \quad (3.17f)$$

$$\tilde{I}_2^p = (\varepsilon_2^p - \varepsilon_1^p) \quad (3.17g)$$

Then the hoop stresses on the two thin faces of the sandwich beam, which are the inputs to the viscoplastic model for computation of the respective inelastic strains, can be obtained in terms of the force and moment from Eq. (3.10) as:

$$\sigma_1(x,t) = \frac{d_2 N(x,t) - M(x,t)}{A_1(d_1+d_2)} \quad (3.18a)$$

$$\sigma_2(x,t) = \frac{d_1 N(x,t) + M(x,t)}{A_2(d_1+d_2)} \quad (3.18b)$$

A closed form solution of the radial deflection w(x, t) at the mid-plane of the ligament can be obtained by substituting the boundary conditions, Eq. (3.15) and Eqs. (3.16) to (3.17) into the governing differential equations (3.14) as:

$$w(x,t)=\tilde{B}\left[\frac{x^2}{2}N_o-\frac{\tilde{C}x^2}{2(\tilde{B}^2-\tilde{A}\tilde{C})}\left(\frac{\tilde{B}p\ell^2}{3}+\tilde{I}_1^{th}-\varepsilon_B+\frac{1}{\ell}\int_0^{\ell}\tilde{I}_1^{p}d\xi\right)\right]$$
$$+\tilde{I}_2^{th}\left[\frac{x^2}{(d_1+d_2)}\times\frac{2\tilde{B}^2-\tilde{A}\tilde{C}}{2(\tilde{B}^2-\tilde{A}\tilde{C})}\right]-p\left[\frac{\tilde{A}\tilde{C}^2\ell^2}{6(\tilde{B}^2-\tilde{A}\tilde{C})}x^2+\frac{\tilde{C}\ell}{6}x^3-\frac{\tilde{C}}{24}x^4\right] \quad (3.19)$$
$$-\left[\frac{1}{(d_1+d_2)}\left(\int_0^x\int_0^x\tilde{I}_2^{p}d\xi\,d\eta-\frac{x^2}{2\ell}\int_0^{\ell}\tilde{I}_2^{p}d\xi\right)\right]$$

The first term on the right hand side of Eq. (3.19) represents the deflection components solely due to the coupling effects, $\tilde{B}$, of extension and bending. Stubstad and Simitses (1987) pointed out that this coupling effect is a result of temperature difference in the radial direction and temperature dependence of the elastic modules. The temperature transients also cause thermally induced bending of the beam element, which is represented by the second term of Eq. (3.19). The third term represents the deflection component solely due to the bending induced by the pressure difference acting on the ligament. The deflection calculated by the first three terms vanish in absence of any pressure and temperature difference across the ligament thickness when the cycle is completed. The fourth term represents the irreversible deflection resulting from the inelastic strain ratcheting induced by thermo-mechanical loading, which contributes to the irreversible bulging-out of the ligament. This inelastic strain ratcheting-induced bending is caused by the pressure difference across the ligament wall and the temperature difference between the hot ligament and the closeout wall. In essence, the irreversible phenomena of creep ratcheting and inelastic strains are responsible for permanent bulging-out and progressive thinning of the coolant channel ligament. The last term in Eq. (3.19) is defined as the irreversible or permanent deflection $w^I(x,t)$ at the mid-plane of the ligament,

$$w^I(x,t)=-\frac{1}{(d_1+d_2)}\left[\int_o^x\int_o^x(\varepsilon_2^p-\varepsilon_1^p)d\xi\,d\eta-\frac{x^2}{2\ell}\int_o^{\ell}(\varepsilon_2^p-\varepsilon_1^p)d\xi\right] \quad (3.20a)$$

This irreversible deflection $w^I(x,t)$ in the radial direction is more significant than the first three terms in Eq. (3.19). Differentiating the above equation twice with respective to x, the inelastic bending moment $M^I(x,t)$ which causes the permanent deflection due to creep ratcheting is obtained as:

$$M^I(x,t)=-\frac{\partial^2 w^I(x,t)}{\partial^2 x}=\frac{1}{(d_1+d_2)}\left[(\varepsilon_2^p-\varepsilon_1^p)-\frac{1}{\ell}\int_0^{\ell}(\varepsilon_2^p-\varepsilon_1^p)d\xi\right] \quad (3.20b)$$

3.3 Thinning Model of the Coolant Channel Ligament

Experimental studies by Hannum et al., (1976) show the evidence of incremental bulging-out and progressive thinning at the center of the ligament after each firing cycle for the oxygen-free high-conductivity (OFHC) copper material. Porowski et al., (1985) proposed a relationship for linear variations in the thickness of the coolant channel ligament, shown in Fig. 3.4, based on experimental observations of the deformed shapes, popularly known as the "doghouse" (Quentmeyer, 1977). The total area of cross-section of the ligament, shown in Fig. 3.5, is conserved under inelastic deformation because the ligament length does not change in the axial (y) direction and the principle of volume conservation holds under plastic deformation. Following the details reported by Porowski et al., (1985), a simple geometric relationship for the incremental permanent deflection is derived as:

$$\frac{1}{2}\ell\delta_1(t) = \frac{1}{2}(\ell + \frac{a}{4})w^I(t) = \frac{1}{2}(\ell + \frac{a}{2})\delta_2(t) \tag{3.21}$$

where δ_1 and δ_2 are denoted as the respective deflections of the cold-side face and hot-side face at the center of the ligament; and a is the rib width in the coolant channel. The time-dependent thinning, $\tau(t)$, of the ligament at its center is obtained as:

$$\tau(t) = \delta_1(t) - \delta_2(t) = \frac{w(t)(4\ell + a)a}{4\ell(2\ell + a)} \tag{3.22}$$

and the normalized thinning, $\bar{\tau}(t)$, relative to the initial ligament thickness, ϑ_o, is obtained as:

$$\bar{\tau}(t) = \tau(t) / \vartheta_o \tag{3.23}$$

and the creep damage of the coolant channel ligament is defined as:

$$D_{cr}(t) = \bar{\tau}(t) / \tau^* \tag{3.24}$$

where τ^* is the critical thinning at which the bulging process becomes unstable leading to tensile rupture. The critical thinning of the ligament, τ^*, is different for different material. For example, τ^* is about 0.37 for OFHC copper (Porowski et al., 1985) and is in the range of 0.05 to 0.08 for NARloy-Z (Kasper, 1984).

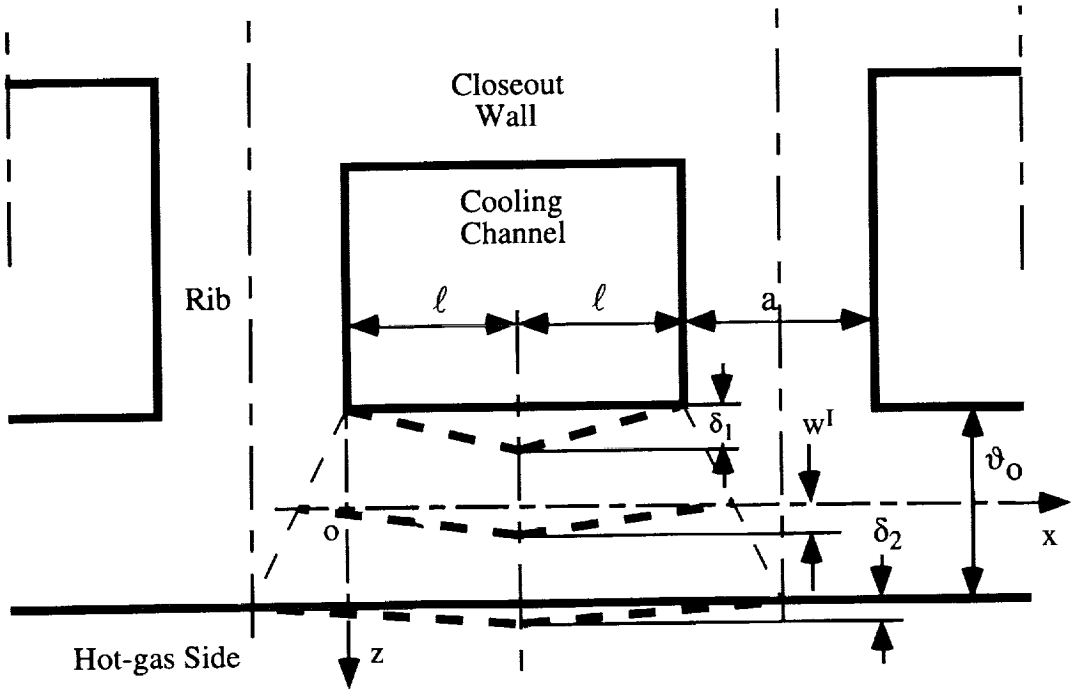

Figure 3.4 Linear thinning model of the coolant channel ligament

The instantaneous thickness of the deformed beam is updated by subtracting the time-dependent thinning from the original thickness:

$$\vartheta(t) = \vartheta_0 - \tau(t) \tag{3.25}$$

Following Fig. 3.5, this information is fed back to the sandwich model in Eq. (3.3).

3.4 Viscoplastic Model for the Coolant Channel Ligament

Most of the studies for structural analysis of the coolant channel ligament use the classical technique of inelastic strain analysis in which interactions between time-independent plasticity and time-dependent creep at elevated temperatures are neglected. However, the experimental results on hot section components have demonstrated that these interactions have significant effects and therefore cannot be ignored (Pugh and Robinson, 1978). Unified viscoplastic analysis is capable of predicting the inelastic behavior of materials at elevated temperatures (for example, thirty percent or higher of the melting point temperature), in which inelastic strains resulting from creep, plasticity, relaxation, and their interactions are accounted for as a single time-dependent quantity.

A sizable body of literature exists on phenomenological constitutive equations for the strain-rate and temperature dependent plastic deformation of metallic materials. Almost all of these unified theories are based on small strain assumptions. More than ten unified constitutive theories have been reviewed by Chen et al. (1984). Allen and Beek (1984) reviewed and clarified the general theory of internal state variables for application to inelastic metals in elevated temperature environments. McDowell (1992) extended the concept of nonlinear kinematics hardening model for multiple back stress under thermo-mechanical cyclic loading.

The viscoplastic theory has been adopted for modeling the nonlinear inelastic material properties at elevated temperatures because of its ability to represent both rate-dependent creep and rate-independent plastic behavior. The general theory of a multiaxial viscoplastic model is reported by Freed (1988), and the associated model parameters are given by Freed and Verrilli (1988) for the main thrust chamber coolant chamber wall with OFHC copper. Robinson and Swindeman (1982) have reported another viscoplastic model, and the material functions and parameters of a copper-zirconium-silver alloy NARloy-Z are specified by Arnold (1987) for the SSME main thrust chamber coolant chamber wall. For the sake of completeness, these two viscoplastic models are presented in the next sections.

3.4.1 Freed's Viscoplastic Model for OFHC Copper

Freed's viscoplastic model serves as the constitutive law with a single kinetic equation and two types of internal state variables, namely, the tensorial anisotropic back stress B_{ij} and the scalar isotropic drag stress D. The static and dynamic recovery terms in the model are assumed to be uncoupled.

The deviatoric stress S_{ij} and the effective stress Σ_{ij} at the two faces of the sandwich beam are defined as follows:

$$S_{ij} = \sigma_{ij} - 1/3\sigma_{kk}\delta_{ij}; \text{ and } \Sigma_{ij} = S_{ij} - B_{ij} \tag{3.26}$$

Flow law:

The inelastic hoop strain rate relations at the two faces of the sandwich beam are given by the flow law as:

$$\dot{\varepsilon}_{ij} = \Theta Z \frac{\Sigma_{ij}}{\|\Sigma\|_2} \tag{3.27}$$

where $\|\Sigma\|_2 = \sqrt{1/2\Sigma_{ij}\Sigma_{ji}}$ is the ℓ_2-norm of the effective stress tensor. The thermal-diffusivity function Θ and Zener-Hollomon parameter are defined as:

$$\Theta = \begin{cases} \exp(-Q/kT) & T \geq 0.5T_m \\ \exp\left\{\dfrac{-2Q}{kT_m}\left[\ln\left(\dfrac{T_m}{2T}\right)+1\right]\right\} & T \leq 0.5T_m \end{cases} \quad \text{and} \quad Z = \begin{cases} AF^n & F \leq 1 \\ A\exp[n(F-1)] & F \geq 1 \end{cases} \tag{3.28}$$

where Q is the activation energy, k is the Boltzmann constant; T is the absolute temperature; T_m is the melting point of the material; A and n are material constants; and $F = \|\Sigma\|_2 / D$.

Evolutionary laws:

The evolutionary laws provide equations for the internal state variables, namely, the back stress B_{ij} and the drag stress D as:

$$\dot{B}_{ij} = H\Theta Z\left(\frac{\Sigma_{ij}}{J_2} - \frac{B_{ij}}{L}\right); \text{ and } \dot{D} = h\Theta\left(\frac{Z}{G} - r(G)\right) \tag{3.29}$$

where H, L, and h are inelastic material constants, and the recovery function r is defined as:

$$r(G) = \begin{cases} 0 & D = D_0 \\ AG^{n-1} & D > D_0 \text{ and } G \leq 1 \\ A\exp[n(G-1)]/G & D > D_0 \text{ and } G \geq 1 \end{cases} \tag{3.30}$$

and $G = \dfrac{L}{S-D}$, where S and D_0 are material constants. The following inequality condition of dissipativity must be satisfied at all instants of time for the viscoplastic theory to be thermodynamically admissible (Freed, 1988):

$$r \geq Z\left[\frac{1}{G} - 2\left(F + \frac{\|B\|_2^2}{LD}\right)\right] \tag{3.31}$$

3.4.2 Robinson's Viscoplastic Model for NARloy-Z

Robinson's model incorporates internal state variables in terms of the components of the back stress tensor, α_{ij}, which accounts for kinematic hardening, and the constant drag stress, K, which represents isotropic hardening of the material. This model employs a dissipation potential to derive the flow and evolutionary laws for the inelastic strain and internal state variables. The nonisothermal multiaxial inelastic constitutive equations are given, in terms of the stress tensor components, σ_{ij}, and the material constants, A, n, m, β, H, R, G_o, K and K_o, as follows:

Flow law:

$$\dot{\varepsilon}_{ij}^p = \begin{cases} \dfrac{AF^n\Sigma_{ij}}{\sqrt{J_2}}; & F > 0 \text{ and } S_{ij}\Sigma_{ij} > 0 \\ 0 \quad ; & F \leq 0 \text{ or } F > 0 \text{ and } S_{ij}\Sigma_{ij} \leq 0 \end{cases} \tag{3.32}$$

where the components of the deviatoric and effective stress tensors are:

$$S_{ij} = \sigma_{ij} - 1/3\sigma_{kk}\delta_{ij}; \text{ and } \Sigma_{ij} = S_{ij} - a_{ij} \tag{3.33}$$

and $$J_2 = 1/2\Sigma_{ij}\Sigma_{ji}; \text{ and } F = J_2 / K^2 - 1 \tag{3.34}$$

Evolutionary laws:

$$\dot{a}_{ij} = \begin{cases} \dfrac{H}{G^{\beta}}\dot{\varepsilon}^{p}_{ij} - \dfrac{RG^{m-\beta}}{\sqrt{I_2}}a_{ij}\,; & G > G_o \quad \text{and} \quad S_{ij}a_{ij} > 0 \\ \dfrac{H}{G_o^{\beta}}\dot{\varepsilon}^{p}_{ij} - \dfrac{RG_o^{m-\beta}}{\sqrt{I_2}}a_{ij}\,; & G \le G_o \quad \text{or} \quad G > G_o \quad \text{and} \quad S_{ij}a_{ij} \le 0 \end{cases} \tag{3.35}$$

where

$$a_{ij} = \alpha_{ij} - 1/3\alpha_{kk}\delta_{ij};\ \ I_2 = 1/2a_{ij}a_{ji};\ \text{and}\ G = I_2 / K_o^2 \tag{3.36}$$

3.5 Model Solution Approach

The partial differential equations (3.14) are approximated via spatial discretization as a set of ordinary differential equations where the number of nodes is selected to be 11 for half of the ligament. Fig. 3.5 illustrates a concept for simultaneously solving the structural and creep damage model equations of the coolant channel ligament. A causal relationship exists between the partial differential equations with respect to the spatial variable x in the Sandwich Beam Model and those with respect to the temporal variable t in the Viscoplastic Model as seen in Fig. 3.5. As explained in Section 3.2.7, the tensile force, bending moment and stresses in the coolant channel ligament are generated from the Sandwich Beam Model for given boundary conditions, plant variables, and inelastic strain $\varepsilon_1^p(x,t)$ and $\varepsilon_2^p(x,t)$ at each instant of time. The plastic strains at each node are obtained from the Viscoplastic Model as shown in Fig. 3.5 at each instant of time in terms of the initial conditions of the plastic strains and internal state variables, and stresses at each node. These partial differential equations with respect to time are derived in Section 3.4 following the Freed's or Robinson's viscoplastic model.

A closed form solution of the mid-plane deflection of the coolant ligament is derived at each node in the spatial direction through the Sandwich Beam Model and fed into the Thinning Damage Model in Fig. 3.4. The damage measure, which is defined in Eq. (3.24) as the thickness reduction of the coolant channel ligament normalized with respect to the original thickness, is calculated and feed back to the Sandwich Beam Model to update the geometric deformation at each instant of the time during the operating cycles. These calculation can be easily performed for on-line life prediction and damage mitigating control process. The time-dependent coolant wall temperature and fluid pressure acting on the ligament, generated from the nonlinear Plant Dynamic Model, are the inputs to the Sandwich Beam Model and Viscoplastic Model. The sets of ordinary differential equations are solved by numerical integration in both the Sandwich Beam Model and Viscoplastic Model. In contrast to the common practice of finite element analysis, the proposed life prediction model for the coolant channel ligament has been proven to be computationally much more efficient than the finite element models with comparable accuracy on damage prediction. Details are given in Chapter 4.

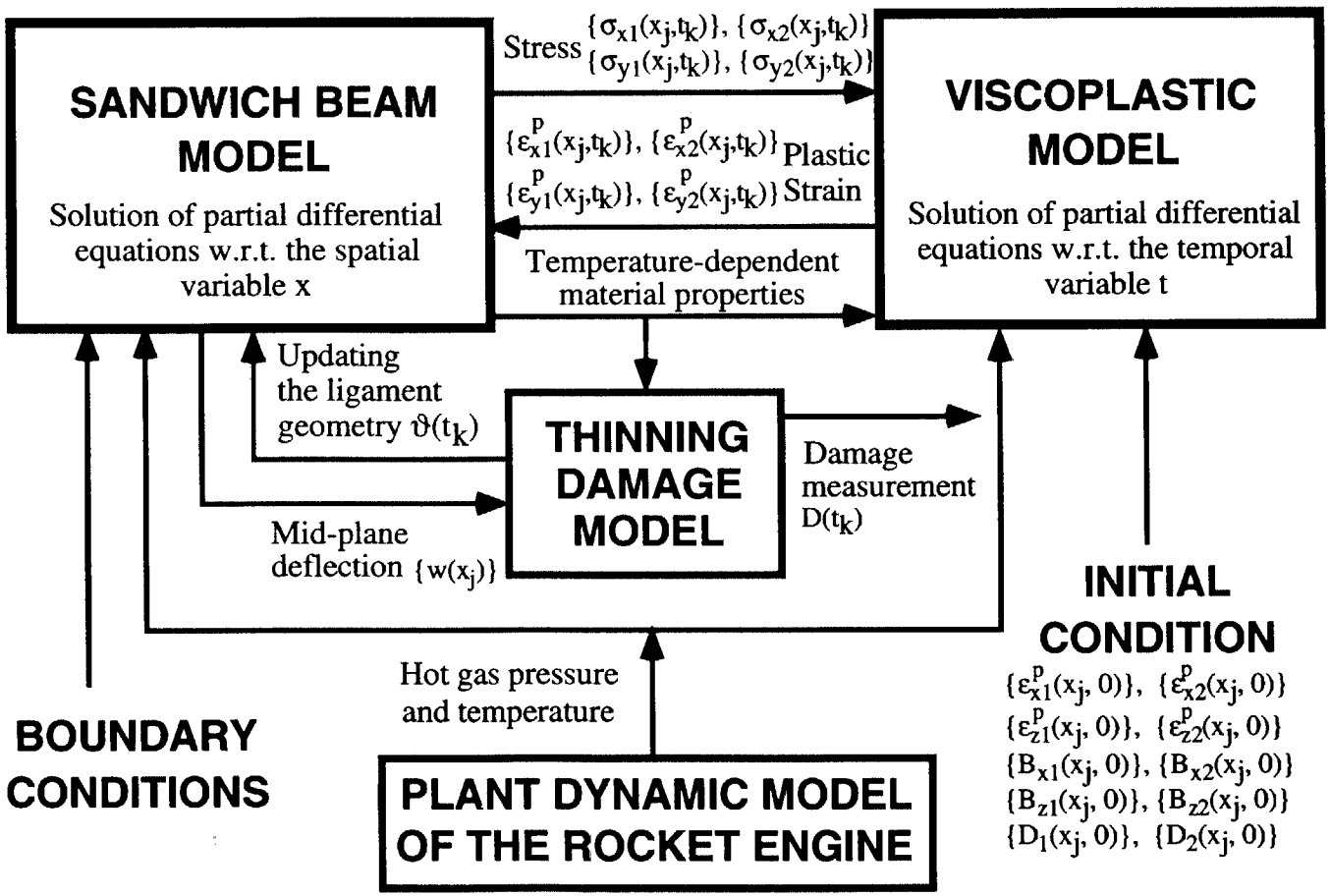

Fig. 3.5 Schematic diagram for solving the creep damage model of the cooling channel ligament

CHAPTER 4

VALIDATION OF STRUCTURAL AND DAMAGE MODELS OF THE REUSABLE ROCKET ENGINE

The structural model of the coolant channel ligament, developed in Chapter 3, is verified through comparison with a finite element model of the main thrust chamber coolant wall for two different materials, namely, oxygen-free high-conductivity (OFHC) copper and a copper-zirconium-silver alloy, known as NARloy-Z. In the proposed model, structural geometry of the ligament and displacement of the closeout wall are used to obtain the required boundary conditions. The data reported in open literature are available for OFHC copper using Freed's viscoplastic model (Freed and Verrilli, 1988) and for NARloy-Z using Robinson's viscoplastic model (Arnold and Robinson, 1989). These models are briefly described in Chapter 3. The model results are compared with the respective finite element analyses of the main thrust chamber coolant wall for both OFHC copper and NARloy-Z. Finally the results of parametric studies for the creep damage of the main thrust chamber coolant wall are presented.

4.1 Validation of the Thrust Chamber Life Prediction Model for OFHC Copper

The life prediction model of the main thrust chamber wall, derived in Chapter 3, in which structural geometry of the ligament and displacement of the closeout wall are used to obtain the required boundary conditions, is verified by comparison with a finite element model (Armstrong, 1981). The temperature-dependent material parameters (e.g., coefficient of thermal expansion and modulus of elasticity) for OFHC copper have been taken from Hannum et al. (1976), and the material constants of the viscoplastic model reported by Freed and Verrilli (1988) are listed in Table 4.1. The geometrical dimensions of the cylindrical thrust chamber coolant channel with 72 channels (Quentmeyer, 1977) are listed in Table 4.2. These data are used for comparing the proposed model with the finite-element model of Armstrong (1981) for OFHC copper.

Table 4.1. The OFHC copper material constants for Freed's viscoplastic model

PARAMETERS	UNIT	VALUE
Young's modulus E	MPa	165 000-125T
α	$^{o}C^{-1}$	$15\times10^{-10}+5\times10^{-9}T$
Poisson's ratio ν	/	0.34
A	s^{-1}	50,000,000
D_o	MPa	1.5
Inelastic material constant h	MPa	500
Inelastic material constant H	MPa	5,000
Limiting value of back stress at kinematic saturation L	MPa	25 exp(-T/300)
n	/	5
Activation energy Q	J/mole	200 000
S	MPa	14.3
Melting Point T_m	K	1356

Table 4.2 The geometrical dimensions of the OFHC copper cylindrical thrust chamber ligament

CHANNEL DIMENSION	UNIT	72 Channels
Ligament length 2ℓ	inch / mm	0.0664 / 1.686
Ligament height ϑ_o	inch / mm	0.035 / 0.889
Rib length a	inch / mm	0.05 / 1.27

Fig. 4.1 shows the time history of the process variables, namely, cold-side wall temperature (T_1), the hot-side wall temperature (T_2), closeout wall temperature (T_B), and the pressure load acting on the ligament for a typical firing cycle having a duration of 3.5 seconds. These process variables excite the structural and damage model as discussed in Chapter 3. The time period of 3.5 seconds includes start-up and heating, referred to as the hot phase of a cycle, and shut-down and cooling, referred to as the cold phase of a cycle.

4.1.1 Single Cycle Behavior

Both temporal and spatial responses of the ligament structure are investigated for a typical single cycle (i.e., the 3rd cycle in this simulation). Time histories of stress and strain of the sandwich beam model are presented in Fig. 4.2 for one firing cycle. As the temperature is rapidly increased corresponding to the transient heating part of the firing cycle, the hoop stress changes from tension to large compression due to the restricted expansion of the hot ligament imposed by the relatively cool closeout wall which exhibits elastic behavior. Thus, during the heating process, large plastic compressive strains are induced in the ligament. The stress overshoot occurs at the instants of t=0.27 sec and 2.07 sec corresponding to the maximum temperature difference between the ligament and closeout wall during the cycle. For the cooling process, a similar situation occurs except that the closeout wall is at a higher temperature than the coolant ligament which is subjected to the maximum tensile stress. As the temperature difference between the ligament and the closeout wall diminishes in the cold phase of the cycle, which follows the minimum temperature difference attained during the shut-down process, the tensile stress induced by the inelastic strain in the ligament reduces from its maximum level.

During the hot phase of the cycle, the compressive stress generally decreases or relaxes after the peak and then tends to keep constant. When the ligament is exposed to a higher temperature environment, the stress relaxation phenomenon becomes more significant. This behavior is characterized as the transition from "primary creep" to "secondary" or "steady" creep, and can be explained in terms of the constitutive equations of viscoplasticity as discussed by Stubstad and Simitses (1987). An examination of the flow model of viscoplasticity described in Chapter 3 reveals that the inelastic strain rate is determined by the effective stress, i.e., the difference between the actual stress and the back stress. The inelastic strain rate changes whenever the rate of the actual stress differs from that of the back stress. In some situations, however, the rates of actual stress and back stress tend to have a constant difference, and the rate of inelastic strain stabilizes to a constant value which is known as the secondary creep.

The shape of the predicted hoop stress and strain at the cold-side and hot-side ligament are shown in Figs. 4.3 and 4.4 at two specific instants of time, namely, t=1.7 and 3.4 sec corresponding to the end of the hot and cold phases of a typical cycle. The stress is tensile throughout the ligament during the chill-down part of the cycle and compressive during the heating-up part as mentioned earlier. The shape of the predicted hoop stress distribution on the hot-side ligament is different from that on the cold-side as seen in Fig. 4.3. This difference is more pronounced during the hot phase of a cycle (at t=1.7 sec) than that during the cold phase (at t=3.4 sec) because of a larger temperature difference between the ligament and the closeout wall. At the end of the cycle, the predicted tensile hoop stress difference in the radial direction is less than about 8 MPa throughout the ligament length. The maximum hoop stress occurs at the center of the hot-side ligament, which is in agreement with the results of finite element analysis reported by Arya (1992). The shape of the predicted inelastic strain distribution in the hoop direction on the hot-side is different from that on the cold-side in Fig. 4.4. The maximum effective strain range occurs on the hot-side at the center of the ligament. This is in agreement with the experimental results reported by Hannum et al. (1976). The effective strain range distribution in the hoop direction can be calculated by taking the difference of the maximum and minimum inelastic strain within one firing cycle.

In order to closely examine the failure mechanism of the coolant channel due to incremental bulging-out, Figs. 4.5 and 4.6 show the irreversible deflection $w^I(x,t)$ defined in Eq. (3.20a) which is normalized with respect to the initial thickness of the ligament, ϑ_o, and the inelastic bending moment $M^I(t,x)$, defined in Eq. (3.20b), at the two instants t=1.7 and 3.4 sec corresponding to the hot and cold phases of a cycle. Since the shape of the distribution of the inelastic strain difference between the hot and cold sides of the ligament is always convex as seen from Fig. 4.4, the shape of $M^I(t,x)$ profile in Fig. 4.6 is also convex by virtue of the relationship in Eq. (3.20b). This bending moment distribution implies progressive bulging-out of the coolant channel ligament in Fig. 4.5 during both hot and cold phases.

Time history of the associated normalized thinning $\bar{\tau}$ at the ligament center, defined in Eq. (3.23a), is shown in Fig. 4.7 for a typical cycle where progressive thinning is observed. The rapid increase in ligament thinning occurs during the heat-up and chill-down transients. During a thermo-mechanical loading transient, the back stress lags behind the actual stress. This results in large rate of change in the inelastic strains which eventually causes a rapid increment of the ligament bulging-out thinning as defined in Eq. (3.20a). The inelastic strains during the temperature and pressure transients change more rapidly than those in the steady state conditions when the thermo-mechanical loading is nearly constant.

4.1.2 Multi-Cycle Behavior

Fig. 4.8 shows profiles of the hoop stress and inelastic strain at the ligament center, averaged over the thickness, from the 2nd cycle to the 20th cycle. The stress profile remains practically unchanged after two or three transient cycles, and the inelastic strain increment per cycle becomes nearly constant. The first two or three cycles of the hoop stress exhibit work hardening because its magnitude increases at both hot and cold phases of the cycle as seen in Fig. 4.8a. Since the viscoplastic process is memory-dependent, the average hoop inelastic strain is initially compressive due to the initial chill-down. As the cycling continues, the inelastic strain becomes tensile even at the hot phase of the cycle due to strain ratcheting. Fig. 4.9 shows that, after the first two or three cycles, the stress-strain hysteresis loops are repetitive with a constant average ratcheting rate of about 0.06% per cycle. Both the effects of non-zero mean stress resulting from unequal tensile and compressive loading, and incomplete stress-strain loops due to temperature cycling are observed in Fig. 4.9. This thermo-mechanical creep ratcheting phenomenon, also discussed by Kasper (1984), is a consequence of cyclically varying mean stress and ligament temperature.

Figs. 4.10 and 4.11 depict the hoop stress and inelastic strain distributions versus cycle on both hot-side and cold-side of the ligament at the instants, t=1.7 and 3.4 sec in each cycle, respectively. The profiles of hoop stresses on the coolant side for both hot and cold phases of a cycle keep on changing during the first few loading cycles, and then tends to stabilize. In contrast, the hoop stress on the hot-side of the ligament remains practically unaltered. These characteristics of stress redistribution at the end of each cycle are in agreement with the results of finite-element analysis reported by Arya (1992). The distribution of the hoop inelastic strain at the end of each cycles is shown in Fig. 4.11 for both the hot-side and cold-side of the ligament. The shape of the inelastic strain distribution is convex on the hot-side of the ligament and concave on the cold-side for all cycles. The distribution of the inelastic strain range, averaged over the ligament thickness, is shown in Fig. 4.12 for several cycles where the maximum strain range occurs at the ligament center and the shape of the distribution remains unchanged after the first a few cycles.

The distributions of the inelastic deflection $w^I(x,t)$, normalized by the initial thickness of the ligament ϑ_o, and the inelastic bending moment $M^I(t,x)$ for different cycles are shown in

Figs. 4.13 and 4.14 at the end of each cycle. As the cycles continue, the difference between the maximum and minimum values of $M^I(t,x)$ distribution increases and the shape becomes more convex. This implies progressive bulging-out of the coolant channel ligament as seen in Fig. 4.13 as discussed earlier for the single-cycle case.

The available experimental results did not provide sufficient information for direct comparison of the ligament thinning at the end of each firing cycle. However, Armstrong (1981) reported the simulation results of ligament thinning at the end of each cycle for 200 cycles using a nonlinear finite element model. Fig. 4.15 compares the results of progressive thinning predicted by the sandwich beam model with those reported by Armstrong (1981) for OFHC copper. Considering the simplicity of the life prediction model presented in this report, the close agreement between this model and the finite element model is very encouraging. One of important features of the proposed life prediction model is its numerical efficiency. For example, one typical firing cycle takes about 0.35 hours on an IBM main frame computer for the finite element model given by Armstrong (1981), and about 0.5 second on a Silicon Graphics computer for the proposed model presented in this report. The thinning rate predicted by the proposed model increases gradually for the initial cycles (i.e., less than 250 cycles), and the grows rapidly after 250 cycles, indicting the approach of the ligament failure. This is qualitatively comparable with the experimental data of the life of the main thrust chamber coolant channel wall in the range of 55 to 220 cycles [Quentmeyer (1977)]. The analytically predicted life is somewhat longer than the experimentally observed life possibly due to the fact that the analytical model is based on uncertain parameters and several simplifying assumptions. These assumptions include absence of local stress concentrations, environmental corrosion effect, preexisting material defects, and fatigue effects.

4.2 Validation of the Thrust Chamber Life Prediction Model for NARloy-Z

The life prediction model of the main thrust chamber wall, derived in Chapter 3, is verified for a copper-zirconium-silver alloy, namely, NARloy-Z by comparison with a finite element model (Kasper, 1984). Table 4.3 lists the temperature-dependent material parameters (Hannum et al., 1976) and the material constants of the viscoplastic model (Robinson and Arnold, 1990) for NARloy-Z. The geometrical dimensions of the main thrust chamber of the SSME with 390 coolant channels are listed in the Table 4.4. These data are used for comparing the proposed model with the finite element model of Kasper (1984) for life prediction of the NARloy-Z ligament.

Fig. 4.16 shows the time history of the process variables, namely, the cold-side wall temperature (T_1), the hot-side wall temperature (T_2), the closeout wall temperature (T_B), and the pressure load acting on the ligament for a typical SSME operating cycle having a duration of 408 seconds. These process variables are inputs to the structural and damage model as discussed in Chapter 3. The time period of 408 seconds includes start-up and heating, referred to as the hot phase of a cycle, and shut-down and cooling, referred to as the cold phase of a cycle. The start-up and heating cycle represents the actual conditions under which the SSME is operated.

Table 4.3. The NARloy-Z material constants for Robinson's viscoplastic model

PARAMETERS	UNIT	VALUE
Young's modulus E	MPa	147 000-70.5T
α	$^{o}C^{-1}$	$15\times10^{-10}+5\times10^{-9}T$
Poisson's ratio ν	/	0.34
A	s^{-1}	1.60×10^{-8}
n	/	4
m	/	8.73
β	/	2.3
(Bingham-Prager) threshold stress K	MPa	6.89
Inelastic material constant H	MPa	1.46×10^{7}
Inelastic material constant R	MPa/s	1.06×10^{-7}
single inelastic state variable at threshold α_o	MPa	14.3

Table 4.4 The geometrical dimensions of the NARloy-Z cylindrical thrust chamber ligament

CHANNEL DIMENSION	UNIT	390 Channels
Ligament length 2ℓ	inch / mm	0.04 / 1.016
Ligament height ϑ_o	inch / mm	0.028 / 0.711
Rib length a	inch / mm	0.045 / 1.143

Time histories of average stress and inelastic strain in the structural model of the coolant channel ligament are presented in Fig. 4.17 for the first operating cycle. As the temperature is rapidly increased during the heating part of the operating cycle, the hoop stress changes from tension to large compression due to the restricted expansion of the hot ligament imposed by the relatively cool closeout wall. Thus, during the heating process, large plastic compressive strains are induced in the ligament. The stress overshoot occurs at the maximum temperature difference between the ligament and closeout wall during the cycle. In the hot phase of the cycle, the magnitude of the compressive stress relaxes to a lower steady state after reaching the peak. When the ligament is exposed to a higher temperature environment and longer time period, the stress relaxation phenomenon would become more prominent.

Fig. 4.18 shows the profile of progressive thinning $\bar{\tau}$ at the ligament center, defined in Eq. (3.23a), for a typical cycle. The rapid increase in ligament thinning occurs during the heat-up and chill-down transients can be explained following the rationale presented in Section 4.2 for the OFHC copper material.

Fig. 4.19 shows the stress-strain hysteresis loops from the 1st cycle to the 3rd cycle, and they are repetitive with a constant average ratcheting rate of about 0.055% per cycle. Since the viscoplastic process is memory-dependent, the average hoop inelastic strain is initially compressive due to the chill-down. As the cycling continues, the inelastic strain becomes tensile even at the hot phase of the cycle due to strain ratcheting. Fig. 4.19 exhibits incomplete stress-strain loops in the creep ratcheting phenomenon due to cyclically varying thermo-mechanical loading. This process occurs at almost zero mean stress for NARloy-Z in contrast to a similar process in Fig. 4.9 at non-zero mean stress for OFHC copper.

Kasper (1984) presented thinning of the NARloy-Z ligament for 150 cycles using a nonlinear finite element analysis. Fig. 4.20 compares the results of progressive thinning predicted by the present life prediction model with those reported by Kasper (1984). The close agreement with the finite element model indicates that the proposed model can capture the failure mechanics (i.e. creep rapture) of the main thrust chamber wall by calculating the mid-plane deflection of the ligament. This model is numerically much more efficient than the finite element model with comparable accuracy. Validation of this numerically efficient model for both NARloy-Z and OFHC copper materials establishes its credibility of proposed life prediction model of the main thrust chamber coolant channel ligament. To the best of the author's knowledge, this model is the only available one which is suitable for both on-line life prediction and damage mitigating control of reusable rocket engines such as the SSME.

4.3 Parametric Studies

This life prediction model is capable of providing general information for better understanding of the failure mechanism and nonlinear structural behavior of the main thrust chamber wall, and allows the design optimization with less computational cost. Specifically, this model can be used to investigate the impact of several factors of the main thrust chamber coolant wall, such as materials selection and mechanical design, thermo-mechanical loading conditions and their duration, on structural durability. This section briefly discusses the impact of the following factors on the life of the main thrust chamber wall.

- Different materials, namely, OFHC copper and NARloy-Z;
- Different ligament dimensions, namely, the number of coolant channels being 390 and 540;
- Different mechanical loading acting on the ligament;
- Different thermal loading acting on the ligament; and
- Different operational cycle duration, namely, a short cycle of 3.5 sec and an extended cycle of 485 sec.

Simulation experiments were conducted to investigate the above five cases one at a time.

4.3.1 Effects of Materials (OFHC Copper and NARloy-Z)

This section presents the results of analyses for two different ligament materials, namely, oxygen-free high-conductivity (OFHC) copper and a copper-zirconium-silver alloy called NARloy-Z, under identical channel dimension, thermo-mechanical loading, and operational cycle duration. The time history of the thermo-mechanical process variables including temperatures at the hot-side (T_2), cold-side and closeout wall (T_1), closeout wall temperature (T_B), and the pressure acting on the ligament are shown in Fig. 4.1 for a typical experimental test cycle having a cycle duration of 3.5 seconds (Armstrong, 1981). The geometric dimensions of the coolant channel ligament are listed in Table 4.2, which correspond to the experimental test specimen given by Quentmeyer (1977).

Profiles of the average cyclic stress/strain hysteresis loop at the ligament center are plotted in Fig. 4.21 for OFHC copper and NARloy-Z during the first three cycles. Even though both OFHC copper and NARloy-Z are subjected to thermal ratcheting caused by incomplete strain reversal, the stress/strain response for these two materials are quite different. The cyclic mean stress of the NARloy-Z is close to zero since the cyclic loading in tension and compression are almost symmetric. In contrast, the mean stress for the OFHC copper is tensile due to unequal loading in the tension and compression as seen in Fig. 4.21. Secondly, NARloy-Z seems to have higher stress relaxation rate than OFHC copper during both tensile and compressive holding periods. The stresses for the OFHC copper exhibit a few cycles of transitions due to the initial stress hardening whereas the stresses for NARloy-Z is almost perfectly periodic during the entire cyclic loading. Since OFHC copper is more ductile than NARloy-Z, the initial compressive

plastic strain of OFHC copper is more pronounced than that of NARloy-Z. The creep ratcheting is about 0.06% per cycle for OFHC copper and about 0.055% per cycle for NARloy-Z.

Once substantial bulging occurs, the thermal and structural characteristics in the vicinity of the bulging region changes because of the deformation in geometry. Since this deformation of the ligament is updated at each instant of time in the life prediction model, the resulting effects on creep ratcheting are more severe for the OFHC copper than those for NARloy-Z. Consequently, OFHC copper suffers from a larger bulging-out as shown in Fig. 4.22. The plastic flow and bulging-out of the inner wall for NARloy-Z are smaller than those for OFHC copper. This prediction is consistent with the damage observed in actual test chambers as reported by Hannum et al. (1976). The thinning of OFHC copper ligament is about ten times larger than that of the NARloy-Z chamber as seen in Fig. 4.22. Both simulation results and experimental observations demonstrate that NARloy-Z materials show an improvement in cyclic life over the OFHC copper under the identical thermo-mechanical loading.

4.3.2 Effects of Ligament Dimensions (Number of 390 and 540 Channels)

This section presents the results of analyses for different number of coolant channels under identical thermo-mechanical cyclic loading and duration for both OFHC copper and NARloy-Z. The time histories of the chamber wall temperatures and pressure are displayed in Fig. 4.1. Geometric dimensions for different configurations of the coolant channel are listed in Table 4.5.

Table 4.5 Different geometrical configurations for the main thrust chamber ligament

CHANNEL DIMENSION	Unit	390 Channels	540 Channels
Ligament length 2ℓ	inch / mm	0.04 / 1.016	0.029 / 0.7338
Ligament height ϑ_o	inch / mm	0.028 / 0.711	0.028 / 0.711
Rib length a	inch / mm	0.045 / 1.143	0.0325 / 0.8255

Profiles of the average cyclic stress/strain hysteresis loops at ligament center are plotted in Figs. 4.23 and 4.24 for OFHC copper and NARloy-Z, respectively, for the first three cycles. Fig. 4.23 shows almost identical stress and plastic strain for different ligament dimensions for NARloy-Z material under identical thermo-mechanical loading. In contrast, the average plastic strains of OFHC copper ligament, as seen in Fig. 4.23, are different for the two different ligament dimensions. The rationale is that OFHC copper is more ductile than NARloy-Z and thereby suffers from larger inelastic deformation which, in turn, influences the structural model by the geometric updating process.

Figs. 4.25 and 4.26 show the normalized thinning, $\bar{\tau}$, of the ligament for both OFHC copper and NARloy-Z materials, respectively, for the two different ligament configurations. For OFHC copper, $\bar{\tau}$ is about ten times larger than that of NARloy-Z due to the different material characteristics as discussed in Section 4.4.1. If the ratio of the length to height is made larger as seen in Table 4.5 for 390 channels, the ligament becomes more flexible resulting in increased bulging-out. Therefore, for both materials, thinning of the ligament with 390 channels is more pronounced than that with 540 channels as seen in Figs. 4.25 and 4.26. In other words, the mechanical design with 540 channels will yield a longer service life of the main thrust chamber than that for 390 channels under identical thermo-mechanical loading.

4.3.3 Effects of Mechanical Loading

Since the main thrust chamber coolant walls are subjected to severe cyclic loading of pressure and temperature, the resulting stresses and plastic strains cause incremental bulging out. To assess the role that pressure loading plays on the so-called doghouse effect (Hannum et al., 1976), the coolant ligament was analyzed for different pressure (mechanical) loading under

identical ligament configuration, temperature (thermal) loading, and operational cycle duration. The time history of the mechanical loading, namely, pressure difference acting on the ligament, $\Delta P(t) = [P_1(t) - P_2(t)]$, is shown in Fig. 4.27 where the magnitude of pressure difference acting on the ligament, ΔP, is increased twofold. The temperature loading history is shown in Fig. 4.1 for OFHC copper and the ligament dimensions are listed in Table 4.2.

Creep ratcheting which is largely induced by the pressure difference is discussed by Porowski et al., (1985). Bending stresses due to the cyclic pressure loading cause a plastic deformation and bulging-out of the ligament during each firing cycle. The time history of the average stress/strain hysteresis loop at the ligament center are plotted in Figs. 4.28 and Fig. 4.29 for OFHC copper and NARloy-Z ligaments during the first three cycles. As the pressure difference is increased twofold, plastic strain and creep ratcheting rate per cycle for OFHC copper change much more significantly than those for NARloy-Z which is less ductile material.

Normalized thinning of the ligament for twofold increase in pressure loading is shown in Figs. 4.30 and 4.31 for OFHC copper and NARloy-Z, respectively. The thinning rate is increased about two times for both OFHC copper and NARloy-Z. The resulting "doghouse" effect predicted here is a result of pressure difference across the coolant channel wall which is also observed in the experiments (Hannum et al., 1976)

4.3.4 Effects of Thermal Loading

Hannum et al (1976) and Quentmeyer (1977) reported that the cycles to failure could be correlated with either hot-side wall temperature, or the difference between hot-side wall and closeout wall temperatures. In order to determine the effects of different temperature (thermal) loading on the thrust chamber life, the following four sets of different temperature loading as depicted in Figs. 4.32 and 4.33 were investigated under identical pressure loading, ligament dimension, and operational cycle. The time history of the pressure (mechanical) loading is shown in Fig. 4.1b and the geometric dimension is listed in Table 4.2. For each of the following four cases, the closeout wall temperature, T_B, was kept unchanged.

- Case A in Fig. 4.32a serving as the baseline case in which the superscript * indicates the reference profile for the hot-side wall temperature, T_2, and the cold-side wall temperature, T_1.
- Case B in Fig. 4.32b representing a increased average wall temperature situation where T_2 is increased by about 150°K over T_2^* during the hot phase of the firing cycle, and T_1 is kept equal to T_1^*.
- Case C in Fig. 4.33a representing a increased average wall temperature situation with no temperature difference across the ligament where T_1 is increased to T_2^* during the hot phase of the firing cycle, and T_2 is kept equal to T_2^*
- Case D in Fig. 4.33b representing a decreased average wall temperature situation where T_1 decreased by about 150°K from T_1^* during the hot phase of the firing cycle, and T_2 is kept equal to T_2^*.

Figs 4.34 and 4.35 plot the stress/strain hysteresis loops for OFHC copper and NARloy-Z, respectively, under four different temperature loading. For Case D, which is the only case where the average ligament temperature is decreased during the hot phase of the firing cycle, the magnitude of both tensile and compressive stresses are reduced and the initial plastic strain is less compressive. This observation is more pronounced for OFHC copper as seen in Fig. 4.34 due to its ductility. The plastic strain range in the ligament is largely dependent on the thermal strain range which is a function of the transient difference between the average ligament

temperature and the closeout wall temperature. Therefore, each of Case B and Case C yields higher effective plastic strain range than Case A due to increased average temperature of the ligament. In contrast, Case D yields smaller effective plastic strain range and compressive mean plastic strain than Case A due to decreased average temperature of the ligament.

However, for both Case B and Case C, where average ligament temperature is increased, the magnitude of the compressive mean plastic strain in Case C is lager than that for Case B as seen in Figs 4.34 and 4.35. The difference between these two cases is that there is no temperature difference across the ligament in Case C whereas there is a temperature difference in Case B. The rationale is that the ligament is subjected to thermally induced bending for Case B due to the constraints at the two ends imposed by the relatively cool closeout wall. This thermally induced bending partially compensates the bulging-out effect resulting from the pressure loading (Arya and Arnold, 1992). However, there is no such effects for Case C since there is no temperature difference across the ligament.

Therefore, the resultant bulging-out due to both pressure and thermally induced bending for Case B are less pronounced than that for Case C as seen in Figs. 4.36 and 4.37 for both OFHC copper and NARloy-Z, respectively. Figs 4.36 and 4.37 also show that Case D has the longest service life for both materials since the average ligament temperature is the lowest among all four cases. This observation reveals that service life of the coolant wall can be improved not only by lowering the ligament temperature but also by increasing the temperature difference across the ligament. The latter phenomena is more significant for OFHC copper than for NARloy-Z because that the beneficial effects of thermally induced bending is more effective for the ductile OFHC copper than NARloy-Z.

4.3.5 Effects of Loading Cycle Duration

The effects of different loading cycle duration on the service life of the combustor wall of rocket engines have been investigated for two types of thermo-mechanical loading cycle duration. The short cycle of 3.5 sec duration, as reported by Arya and Arnold (1992), corresponds to the laboratory tests on the cylindrical thrust chambers whereas the extended cycle of 485 sec duration corresponds to the loading cycle experienced by the SSME. A comparison of the hoop stress distributions for the short and extended loading cycles shows that the stresses for the extended loading cycles are, in general, lower in magnitude than those for the short loading cycles. The rationale is that the extended loading cycle has a longer explosion time which enhances the stress relaxation. The plastic strain range for the extended cycle is also larger than that for the short cycle.

Fig. 4.38 depicts the normalized thinning, $\bar{\tau}$, of the OFHC copper ligament as a function of the number of cycles for both the short and extended loading cycles. A comparison of the $\bar{\tau}$ curves for these two loading cycles reveals that thinning is larger for the extended cycle. This happens because that the plastic strain obtained from the viscoplastic model increases as the hold time is increased for the extended cycle. Therefore, the irreversible or permanent deformation of the coolant channel ligament would increase more for the extended cycle than that for the short cycle. A similar behavior is observed for NARloy-Z in Fig. 4.39 as discussed by Arya and Arnold (1992). In summary, the bulging-out and thinning phenomena of the coolant channel ligament increase for both OFHC copper and NARloy-Z as the duration of the loading cycle is increased.

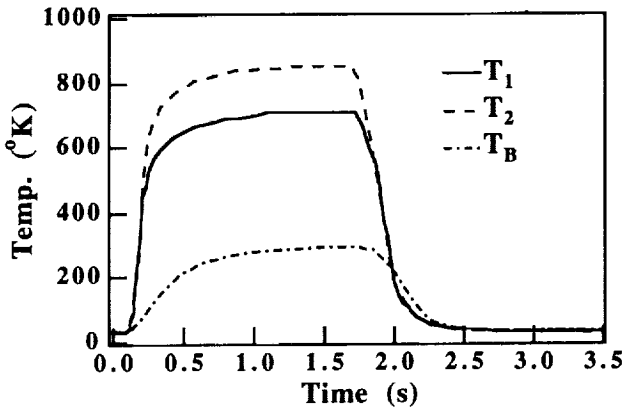

(a) Temperature (°K) History

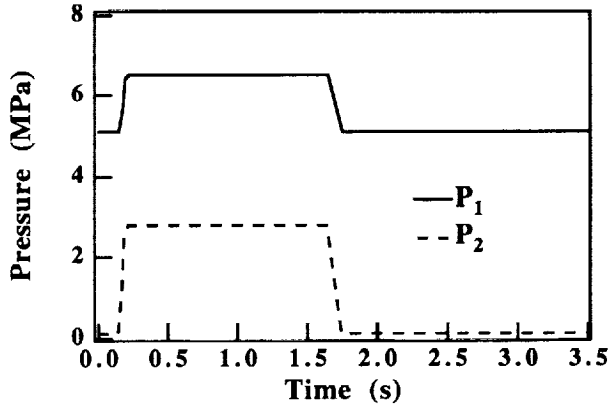

(b) Pressure (MPa) History

Fig. 4.1 Typical temperature/pressure profile for each cycle (Armstrong, 1979)

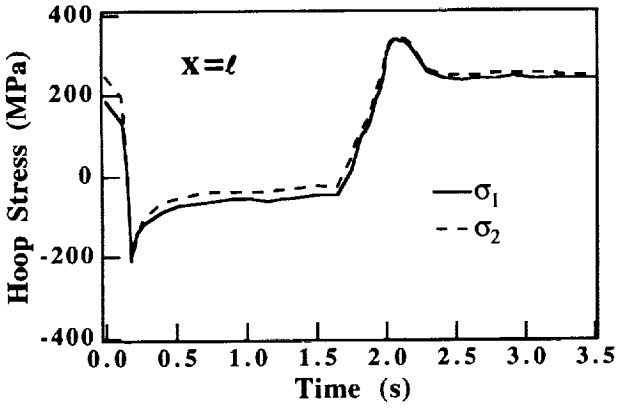

(a) Cyclic hoop stress (Mpa) vs. time

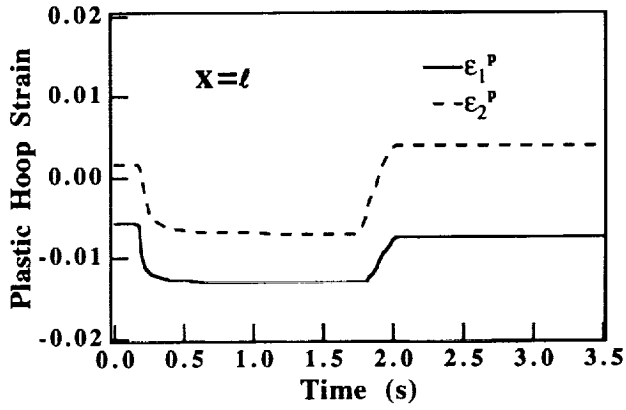

(b) Cyclic inelastic hoop strain vs. time

Fig. 4.2 Hoop stress/strain at x=ℓ for the 3rd cycle

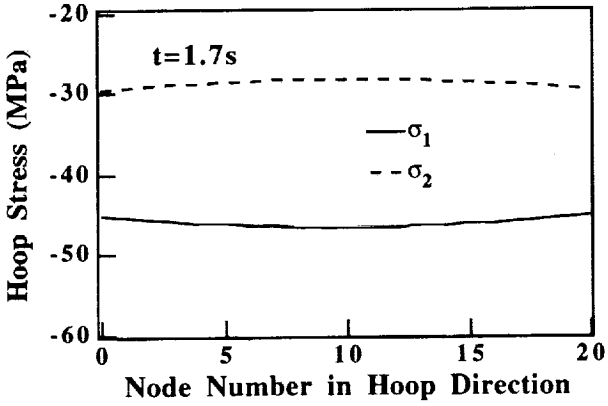

(a) at hot phase of cycle (t=1.7 sec)

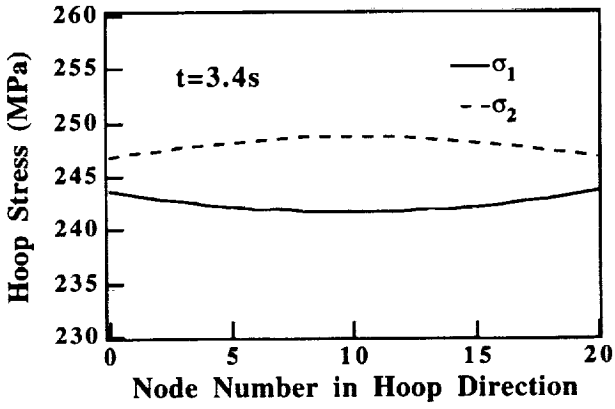

(b) at cold phase of cycle (t=3.4 sec)

Fig. 4.3 Hoop stress distribution at specified time for the 3rd cycle

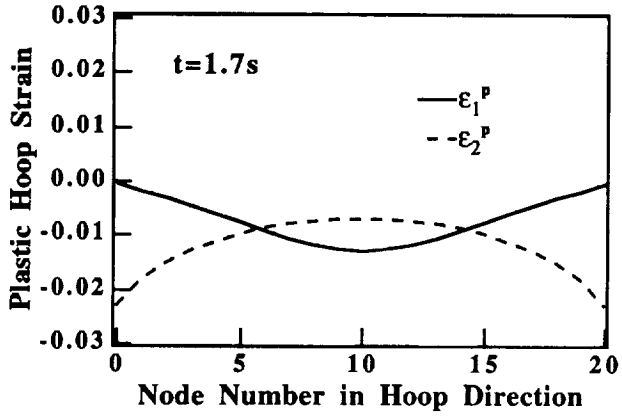

(a) at hot phase of cycle (t=1.7 sec)

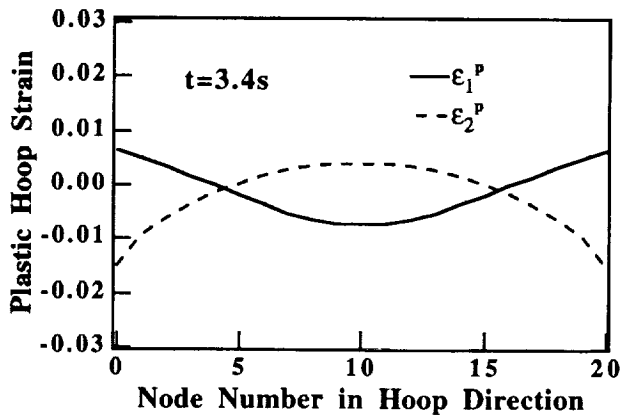

(b) at cold phase of cycle (t=3.4 sec)

Fig. 4.4 Plastic strain distribution at specified time for the 3rd cycle

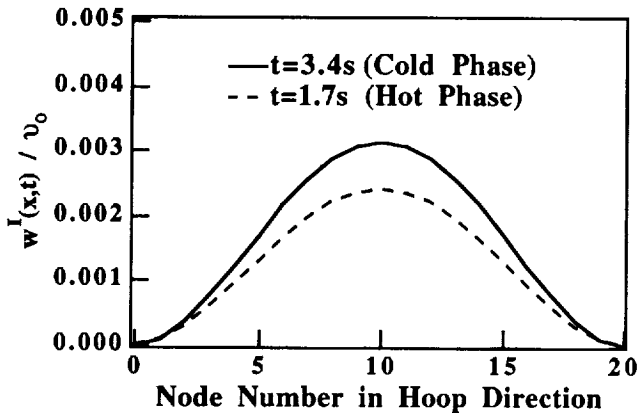

Fig. 4.5 Bulging-out $w^I(x,t)/\vartheta_o$ distribution for the 3rd cycle

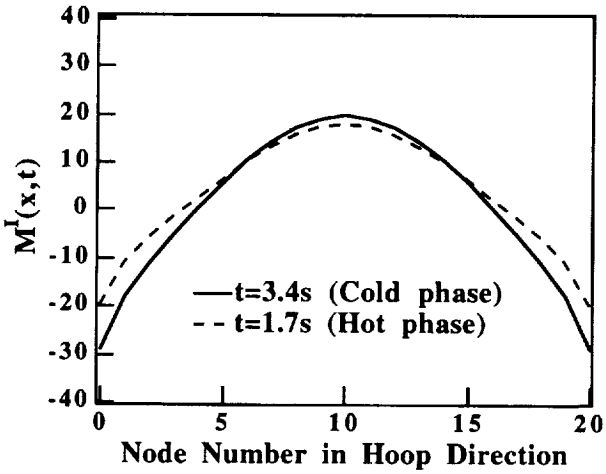

Fig. 4.6 Bending moment $M^I(x,t)$ distribution for the 3rd cycle

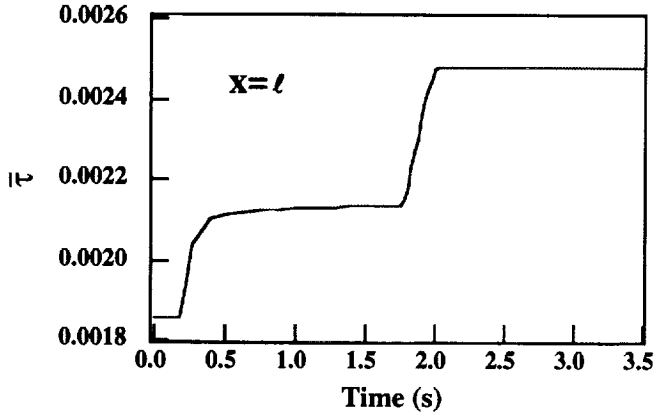

Fig. 4.7 Normalized thinning $\bar{\tau}$ profile for the 3rd cycle

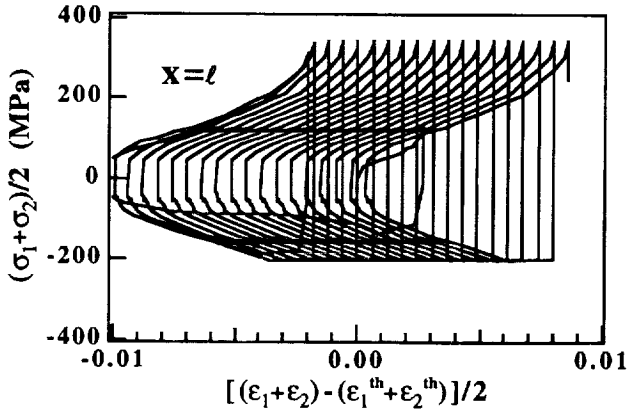

Fig. 4.8 Cyclic stress/strain hysteresis loop from 2nd to 20th cycle

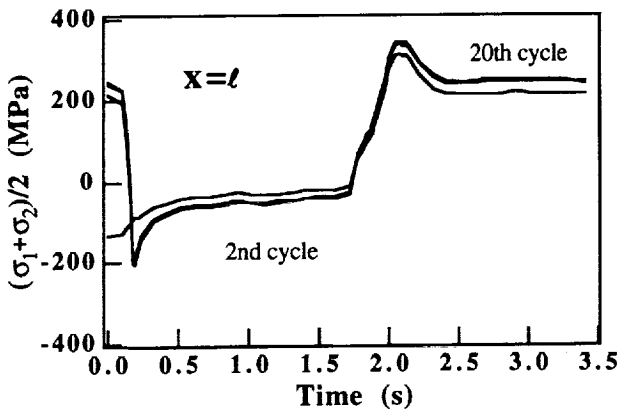

(a): Average cyclic hoop stress (Mpa)

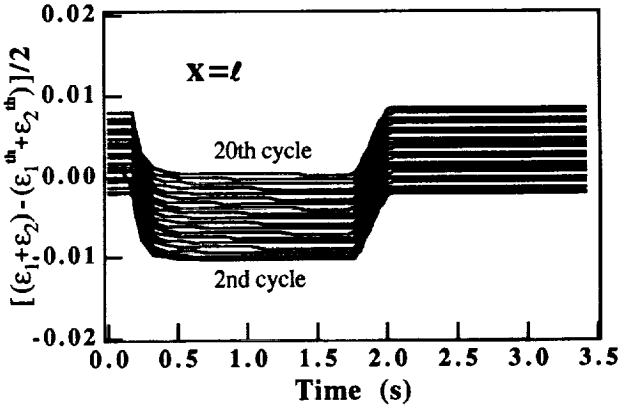

(b): Average cyclic plastic hoop strain

Fig. 4.9 Average cyclic hoop stress/strain profile at x=ℓ for multiple cycles

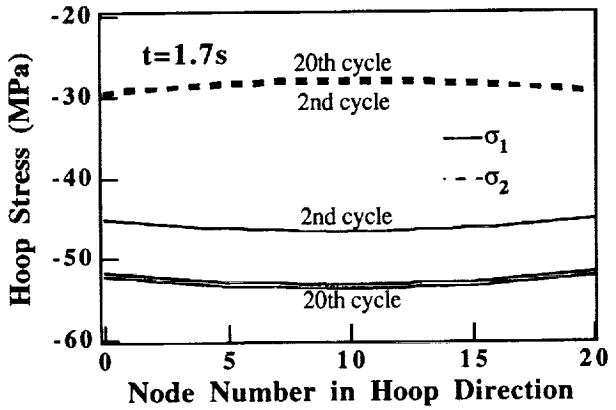

(a) at hot phase of cycle (t=1.7 sec)

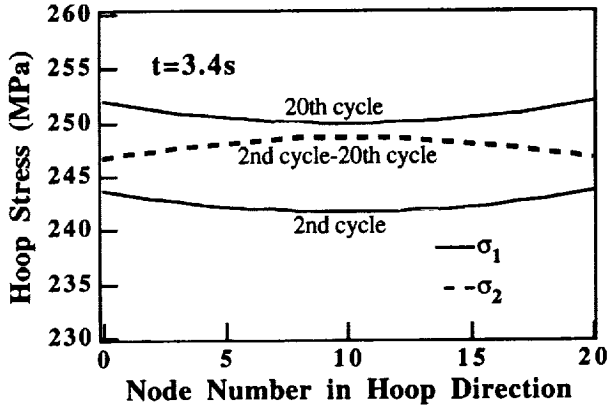

(b) at cold phase of cycle (t=3.4 sec)

Fig. 4.10 Hoop stress distribution at specified times for multiple cycles

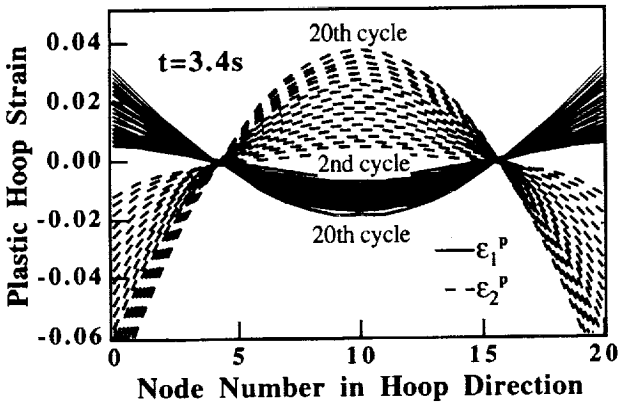

Fig. 4.11 Plastic hoop strain distribution at t=3.4 sec for multiple cycles

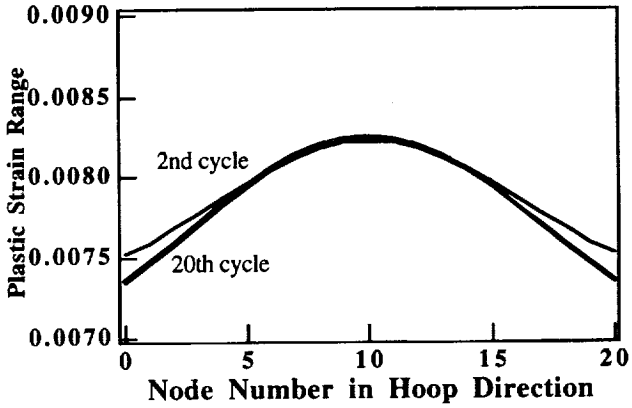

Fig. 4.12 Predicted plastic hoop strain range distribution for multiple cycles

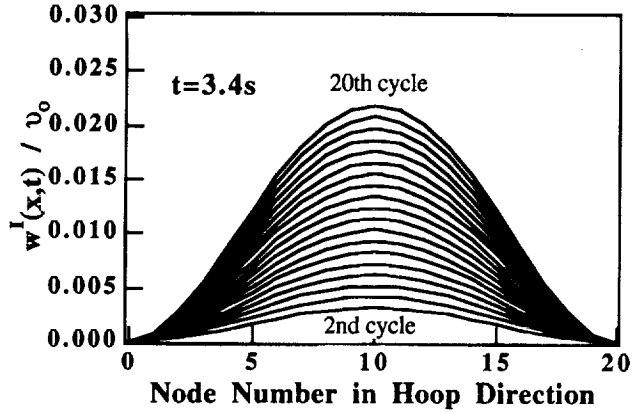

Fig. 4.13 $w^I(x,t)/\vartheta_o$ at cold phase of cycle for multiple cycles

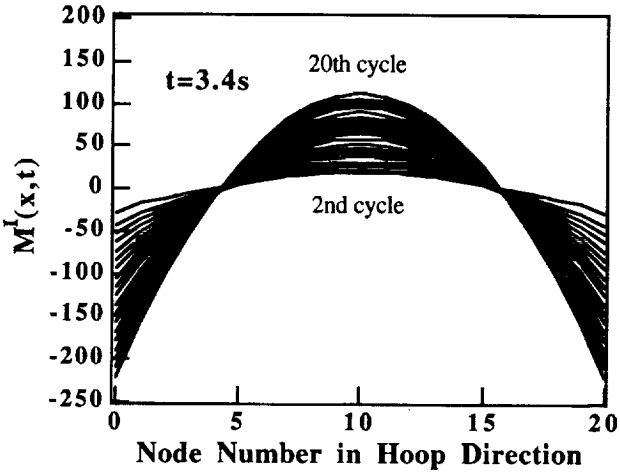

Fig. 4.14 $M^I(x,t)$ distribution at cold phase of cycle for multiple cycles

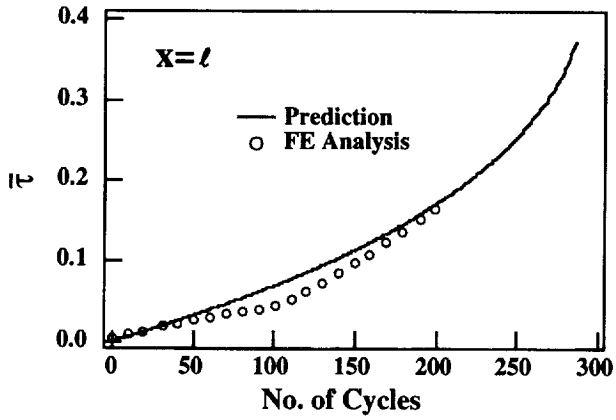

Fig. 4.15 Normalized thinning $\bar{\tau}$ profile at x=ℓ for OFHC copper

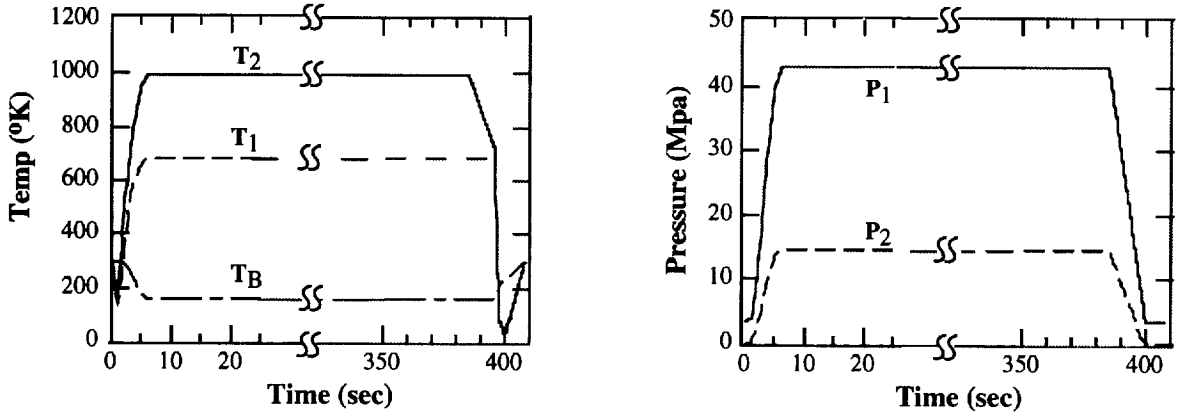

(a) Temperature (°K) history (b) Pressure (MPa) history

Fig. 4.16 Temperature /pressure profile for a typical cycle

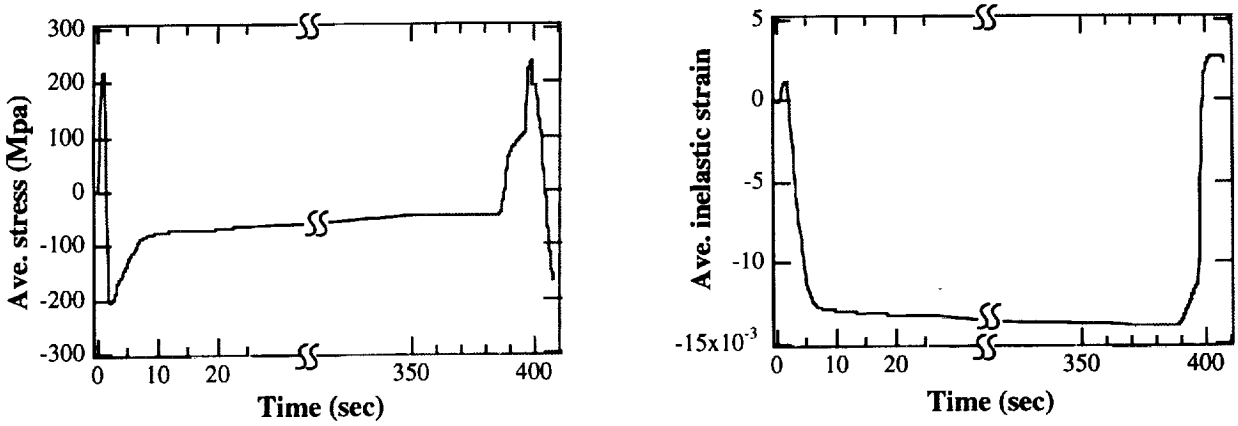

(a) Average cyclic hoop stress (Mpa) vs. time (b) Average cyclic inelastic hoop strain vs. time

Fig. 4.17 Average cyclic hoop stress/strain profile at x=ℓ

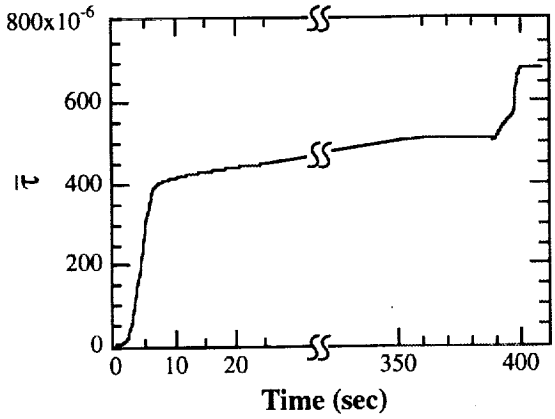

Fig. 4.18 Normalized thinning $\bar{\tau}$ Profile For a typical cycle

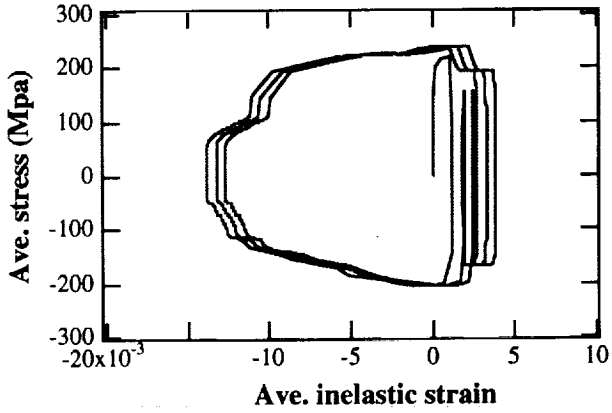

Fig. 4.19 Average cyclic stress/strain hysteresis loop

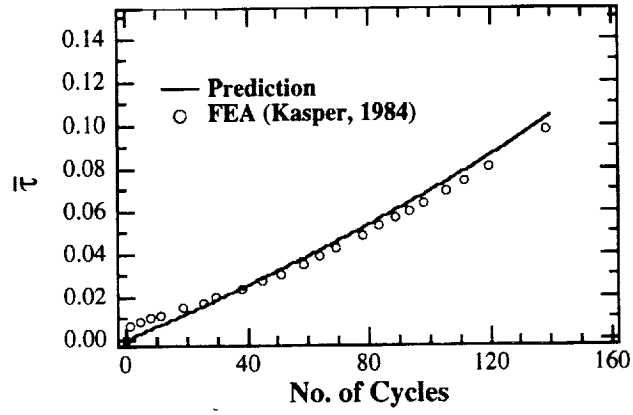

Fig. 4.20 Normalized thinning $\bar{\tau}(t)$ profile at x=ℓ for NARloy-Z

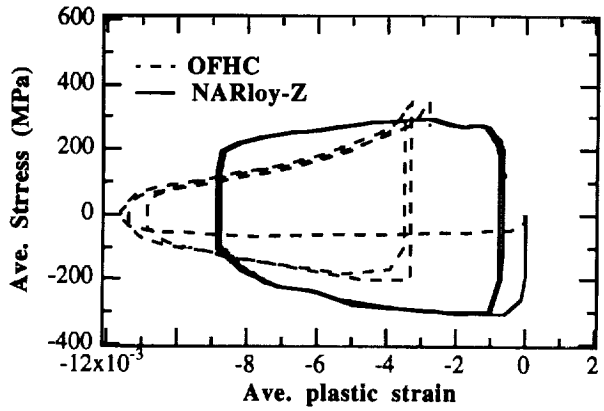

Fig. 4.21 Cyclic stress/strain hysteresis loop

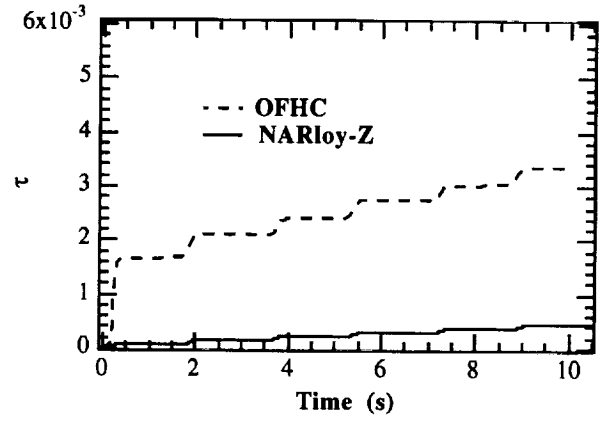

Fig. 4.22 Normalized thinning $\bar{\tau}(t)$ profile for different materials during the first three cycles

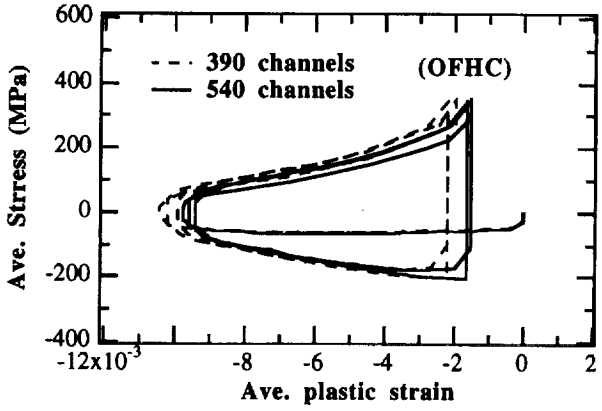

Fig. 4.23 Cyclic hysteresis loop (OFHC)

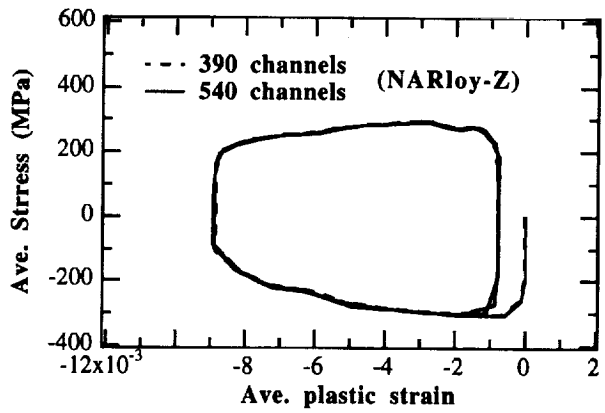

Fig. 4.24 Cyclic hysteresis loop (NARloy-Z) for different channel dimensions during the first three cycles

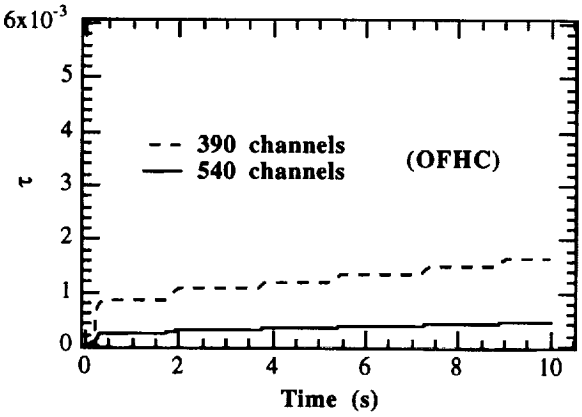

Fig. 4.25 $\bar{\tau}(t)$ profile (OFHC)

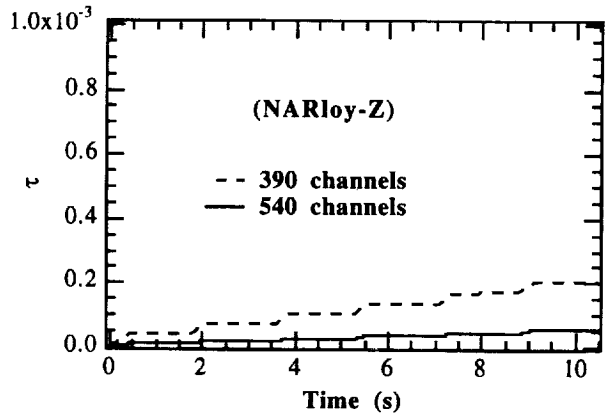

Fig. 4.26 $\bar{\tau}(t)$ profile (NARloy-Z for different channel dimensions during the first three cycles

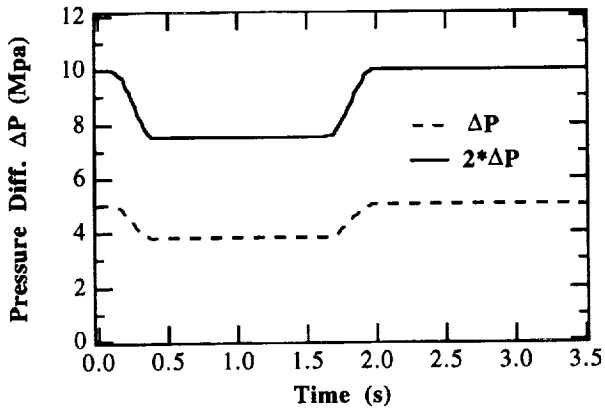

Fig. 4.27 Two pressure loading ($\Delta P=P_1-P_2$) histories for each operating cycle

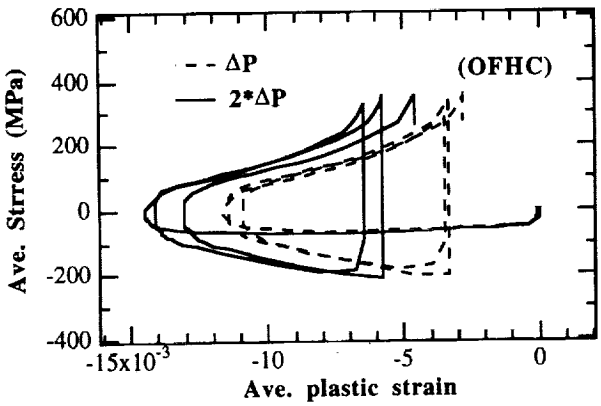

Fig. 4.28 Cyclic hysteresis loop (OFHC) for different pressure loading during the first three cycles

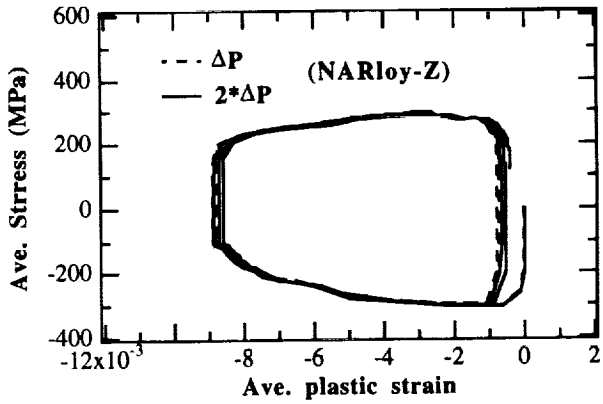

Fig. 4.29 Cyclic hysteresis loop (NARloy-Z) for different pressure loading during the first three cycles

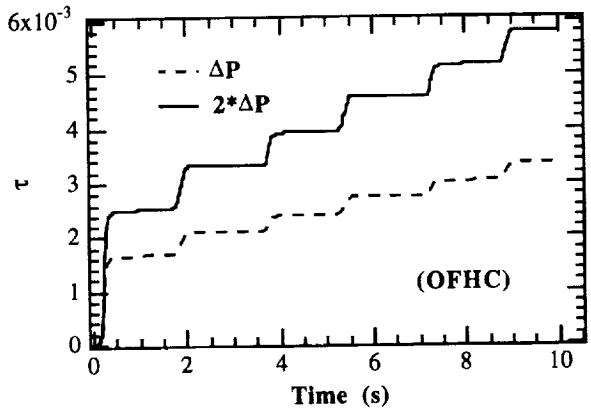

Fig. 4.30 $\bar{\tau}(t)$ profile (OFHC) for different pressure loading during the first three cycles

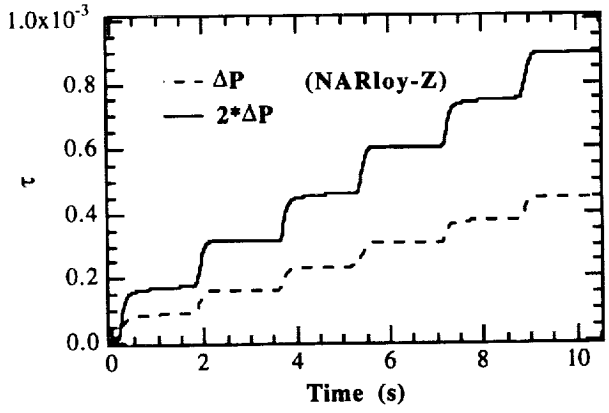

Fig. 4.31 $\bar{\tau}(t)$ profile (NARloy-Z) for different pressure loading during the first three cycles

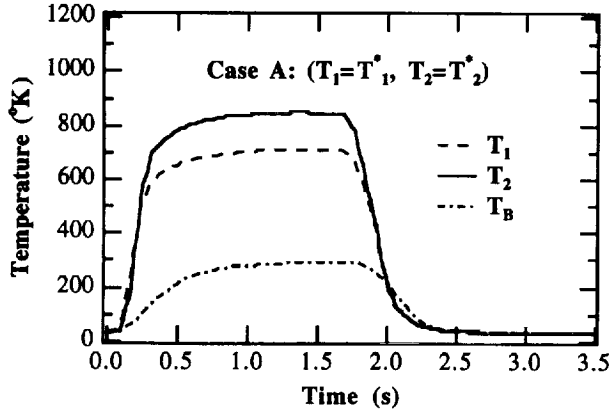

(a) : Case A: for $T_1 = T_1^*, T_2 = T_2^*$

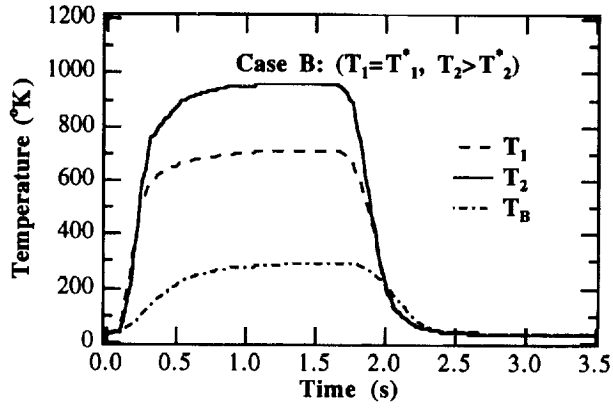

(b): Case B: for $T_1 = T_1^*, T_2 = T_3^* > T_2^*$

Fig. 4.32 Typical temperature profile for different temperature loading cycles

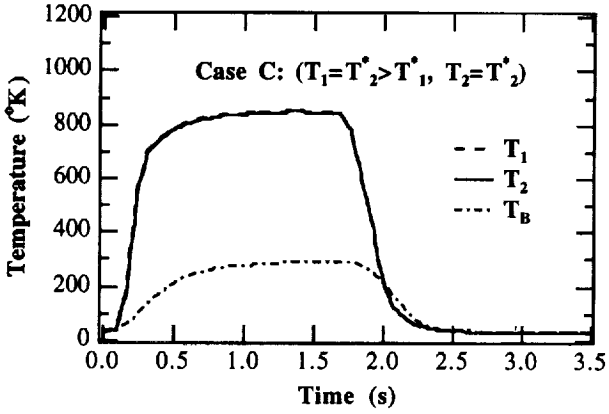

(a) Case C: for $T_1 = T_2^* > T_1^*, T_2 = T_2^*$

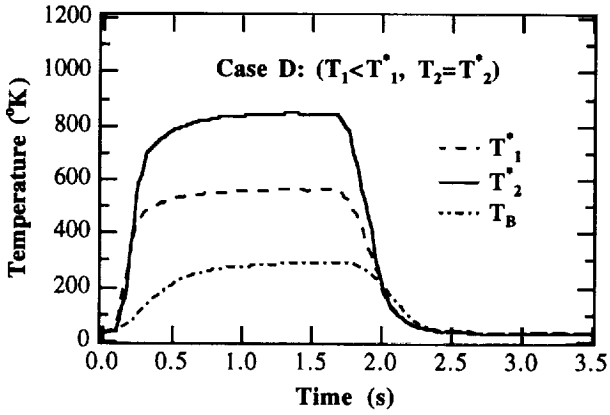

(b) Case D: for $T_1 = T_o < T_1^*, T_2 = T_2^*$

Fig. 4.33 Typical temperature profile for different temperature loading cycles

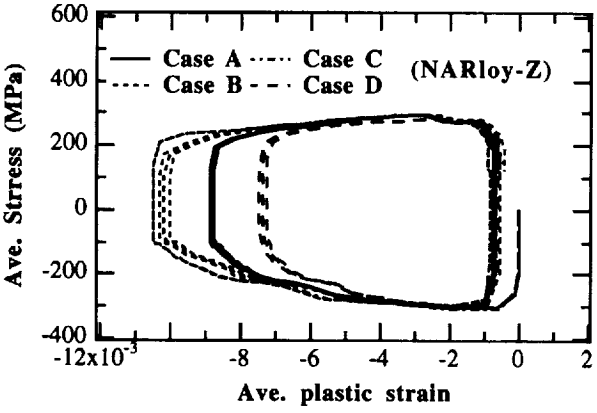

Fig. 4.34 Cyclic hysteresis loop (OFHC) for different temperature loading during the first three cycles

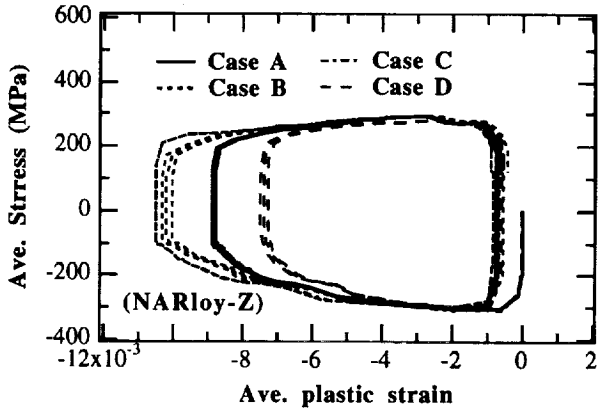

Fig. 4.35 Cyclic hysteresis loop (NARloy-Z)

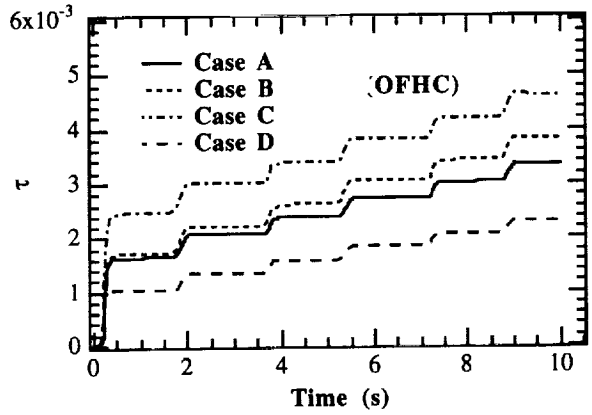

Fig. 4.36 $\bar{\tau}(t)$ profile (OFHC) for different temperature loading during the first three cycles

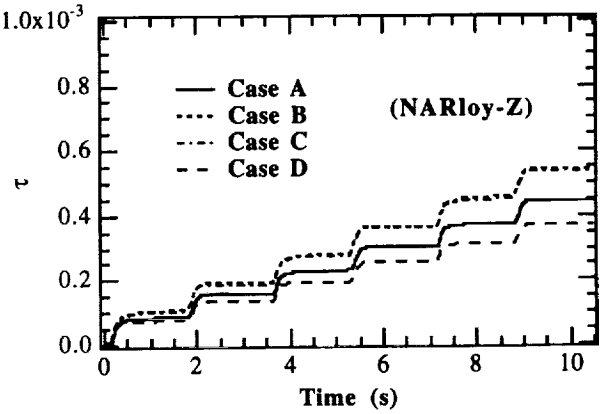

Fig. 4.37 $\bar{\tau}(t)$ profile (NARloy-Z)

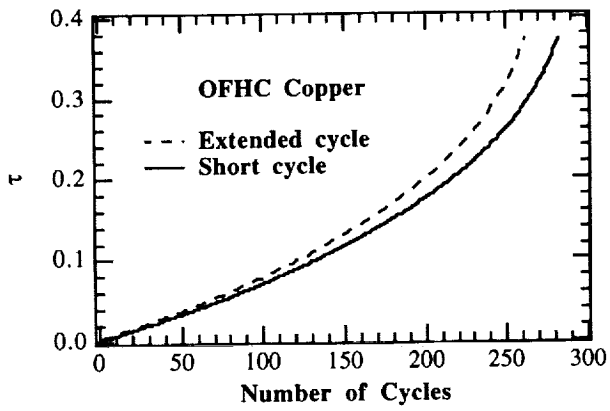

Fig. 4.38 $\bar{\tau}(t)$ profile (OFHC) for different operational cycle duration for multi-cycle

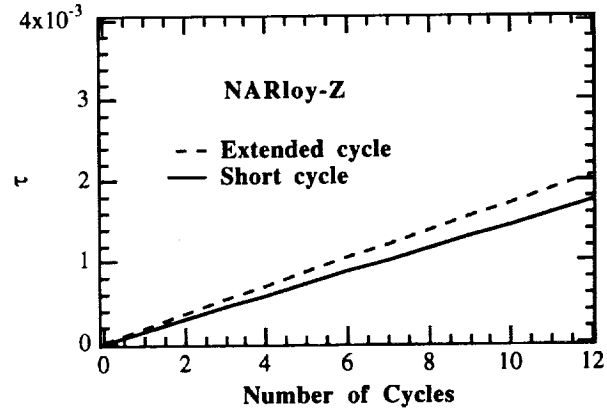

Fig. 4.39 $\bar{\tau}(t)$ profile (NARloy-Z)

CHAPTER 5

INTEGRATED LIFE EXTENSION AND CONTROL OF THE REUSABLE ROCKET ENGINE

The general structure of the damage mitigating control system is briefly described in Section 1.3.4 of Chapter 1. The major tasks in the synthesis of the damage mitigating control system in Fig. 5.1 are:

(i) Formulation of an appropriate dynamic model of the plant (e.g., the Space Shuttle Main Engine);
(ii) Formulation of the structural model and damage model of the critical plant components (e.g., turbine blades and main thrust chamber coolant channel ligament);
(iii) Synthesis of a feedforward control policy with the objective of achieving structural durability and high performance; and
(iv) Synthesis of a feedback control policy for intelligent decision-making such as damage prognosis and risk analysis via on-line feedback of the plant and damage monitoring information.

The first and the second tasks are addressed in Chapter 2 and Chapter 3, respectively. The third task is described in this chapter. The fourth task is not within the scope of this research report.

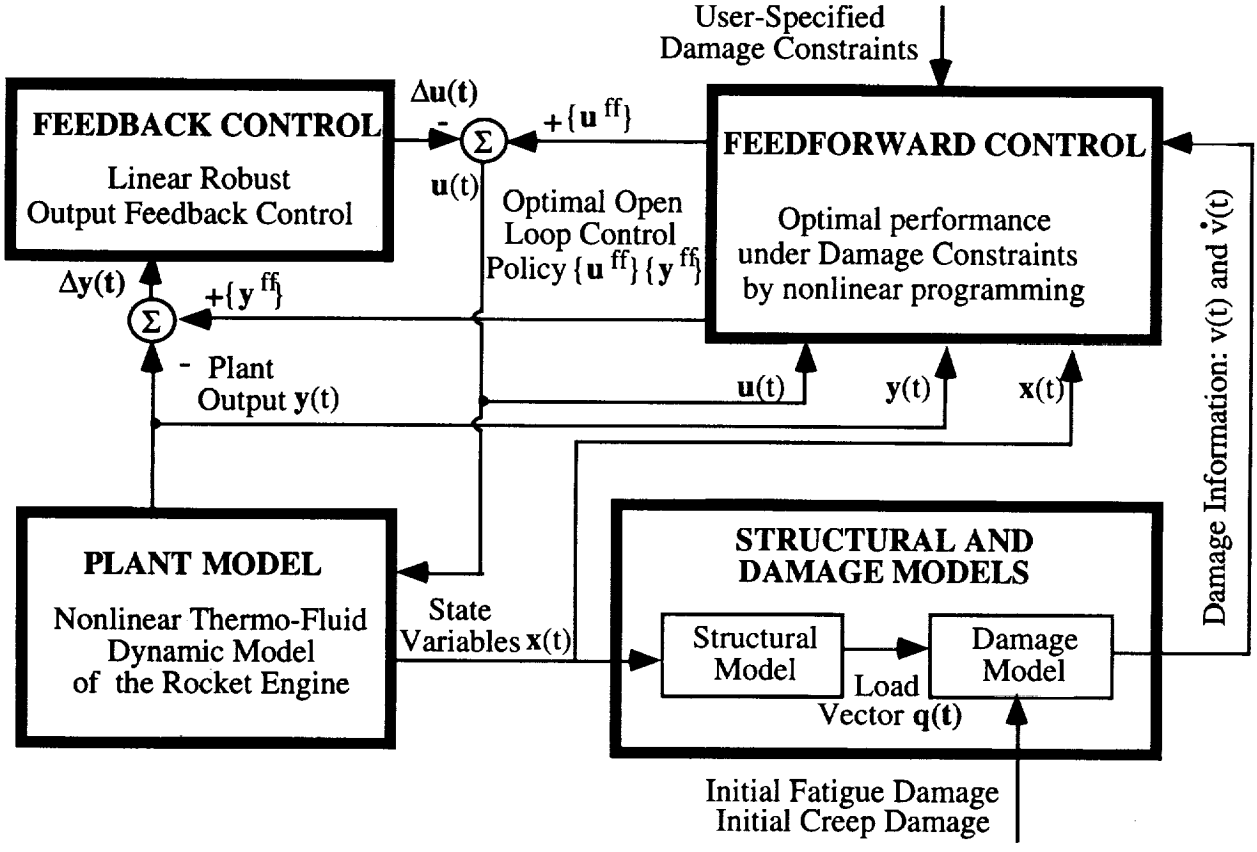

Fig. 5.1 Schematic diagram of the damage mitigating control system

5.1 Feedforward Optimal Control Policy

The feedforward control policy is obtained via nonlinear programming (Luenberger, 1984) by optimizing a specified cost functional of the plant dynamic performance without violating

preassigned constraints on the damage rate and accumulation. The optimal control problem is stated in the following three subsections.

5.1.1 Process to Be Controlled

The rocket engine under consideration is similar to the Space Shuttle Main Engine (SSME), and the critical components that are prone to damage are the fuel and oxidizer turbine blades and main thrust chamber coolant channel ligament. A general structure of the plant and its damage dynamics is represented in the deterministic continuous-time setting as:

Plant dynamics: $$\dot{\mathbf{x}} \equiv \frac{d\mathbf{x}}{dt} = \mathbf{f}(\mathbf{x}(t),\mathbf{u}(t)); \quad \mathbf{x}(t_o) = \mathbf{x}_o \tag{5.1}$$

Plant outputs: $$\mathbf{y}(t) = \mathbf{g}(\mathbf{x}(t),\mathbf{u}(t)) \tag{5.2}$$

Damage dynamics: $$\dot{\mathbf{v}} \equiv \frac{d\mathbf{v}}{dt} = \mathbf{h}(\mathbf{v}(t),\mathbf{q}(\mathbf{x},t)); \mathbf{v}(t_o) = \mathbf{v}_o; \mathbf{h} \geq 0 \ \forall t \in [t_o, t_f] \tag{5.3}$$

Structural outputs: $$\mathbf{q}(t) = \mathbf{h}(\mathbf{x}(t),\mathbf{u}(t)) \tag{5.4}$$

where t_o is the initial time and t_f is the final time; $\mathbf{x} \in \Re^n$ is the plant state vector; $\mathbf{y} \in \Re^\ell$ is the plant output vector, $\mathbf{u} \in \Re^m$ is the control input vector; $\mathbf{q} \in \Re^p$ is the structural output vector; $\mathbf{v} \in \Re^r$ is the damage state vector. The dimensions of these vectors in the damage mitigating control system are: n=20, l=10, m=2, p=7, and r=3 based on the plant dynamic model derived in Chapter 2 and the structural and damage models presented in Chapter 3. The nonlinear differential equations (5.1) and (5.3) are assumed to satisfy the local Lipschitz condition (Vidyasagar, 1992) within the domain of the plant operating range.

The state-variable representation of the damage model in Eq. (5.3) allows the instantaneous damage rate $\dot{\mathbf{v}}(t)$ to be dependent on the current level $\mathbf{v}(t)$ of accumulated damage. The physical interpretation of the above statement is that a given test specimen or a plant component, under identical stress-strain hysteresis, shall have different damage rates for different initial damage. For example, if the initial crack length is 100 mm, the crack propagation rate will be different from that for an initial crack length of 20 mm under identical stress excursions. Therefore, the initial damage $\mathbf{v}_o$ is important due to its effects on the dynamics of damage accumulation.

5.1.2 System Constraints

Constraints on allowable values of the control variables $\mathbf{u}(t)$ represent the actuator saturation, and preassigned limits of the damage rate and damage accumulation are imposed for assuring structural durability as follows:

Natural bounds: $$0 \leq \mathbf{u}(t) \leq \alpha \tag{5.5}$$

Nonlinear constraints: $$0 \leq \mathbf{h}(\mathbf{v}(t),\mathbf{q}(\mathbf{x}(t),t)) < \beta(t) \tag{5.6}$$

Nonlinear constraints: $$(\mathbf{v}(t_f) - \mathbf{v}_o) < \Gamma \tag{5.7}$$

where $\alpha \in \Re^m$ is the natural bound vector of the control valve positions; $\beta(t) \in \Re^r$ is specified tolerances for the damage rate vector; and $\Gamma \in \Re^r$ is specified tolerances for damage accumulation vector, which need to be appropriately chosen by considering the mission objectives, the time interval between maintenance actions, service life and allowable risk.

5.1.3 Cost Functional

The task to be accomplished is the up-thrust transient process which transfers the plant state from a known initial state $\mathbf{x}(t_0)$ to the specified final steady state $\mathbf{x}_{ss}$ and the corresponding control effort $\mathbf{u}_{ss}$ at the specified final time t_f. The quadratic cost functional is chosen to be the square of the weighted ℓ_2-norm of the plant states, a selected plant output, control efforts and final state errors. The task is to minimize this cost functional:

$$J = (\mathbf{x}(t_f) - \mathbf{x}_{ss})^T \mathbf{M}(\mathbf{x}(t_f) - \mathbf{x}_{ss}) + \int_{t_0}^{t_f} S(y(t) - y_{ss})^2 dt$$
$$+ \int_{t_0}^{t_f} [(\mathbf{x}(t) - \mathbf{x}_{ss})^T \mathbf{Q}(\mathbf{x}(t) - \mathbf{x}_{ss}) + (\mathbf{u}(t) - \mathbf{u}_{ss})^T \mathbf{R}(\mathbf{u}(t) - \mathbf{u}_{ss})] dt \quad (5.8)$$

where the penalty matrices **M**, **Q**, S, and **R** are symmetric positive semi-definite and have compatible dimensions. The purpose of including the plant output $y(t)$ in the cost functional is to inhibit any large deviation of this output variable from its desired value. In this specific case, the output variable of interest is the oxygen/fuel (O_2 / H_2) mixture ratio because the rocket engine performance and propellant utilization are very sensitive to the mixture ratio which should be maintained at the desired value of 6.02 during the transients. Note that S is a (1×1) matrix in this case because only one output vector has been selected.

The cost functional J is to be chosen in an appropriate form representing a weighted trade-off between the following three criteria of system performance. The matrix **M** is the cost or penalty associated with the terminal error. The matrices **Q** and S are the cost or loss function associated with the transient error of the plant state and the selected plant output of interest. The matrix **R** is the cost or loss function associated with the control sequence. Therefore, the weighting matrices **M**, **Q**, S, and **R** in the cost functional J must be selected by the system designer to put appropriate emphasis on the terminal accuracy, transient behavior of the plant, damage dynamics, and the expended control effort, respectively.

If the plant model is completely controllable, there is at least one control sequence which will transfer any initial state to the desired final state. However, controllability does not guarantee that a solution exists for every optimal control problem. Whenever the admissible controls are restricted to the feasible set, certain final states may not be attainable for some constraints. In this research, a general purpose nonlinear programming software, namely, NPSOL by Gill et al. (1991) has been adopted for solving the feedforward optimal control problem. Details are reported by Ray et al. (1994c) and Ray and Wu (1994a).

5.2 Problem Formulation

The problem is to generate an optimal control sequence for up-thrust transient operations of a reusable rocket engine such as the SSME such that the optimal control will not only make a trade-off between the performance and damage but also strike a balance between potentially conflicting requirements of damage mitigation at the individual critical points. This optimization problem is represented in the discrete-time setting to find an optimal control sequence $\{\mathbf{u}_k\}$ for given initial and terminal conditions, which minimizes the specified cost functional J of Eq. (5.8) subject to the following constraints:

- The discretized dynamic system constraints in Eqs. (5.1) to (5.4);
- The natural bounds of the control input sequence in Eq. (5.5);
- The constraints on the damage rate in Eq. (5.6); and
- The constraints on the accumulated damage of in Eq. (5.7).

The steps for generating the optimal control policy are as follows:

Minimize: $$J(\tilde{\mathbf{u}}_k) = \tilde{\mathbf{x}}_N{}^T \mathbf{M} \tilde{\mathbf{x}}_N + \sum_{k=o}^{N-1} [\tilde{\mathbf{x}}_k{}^T \mathbf{Q} \tilde{\mathbf{x}}_k + S\tilde{y}_k{}^2 + \tilde{\mathbf{u}}_k{}^T \mathbf{R} \tilde{\mathbf{u}}_k] \Delta t_k \quad (5.9)$$

Subject to: $$\mathbf{x}_{k+1} = \mathbf{x}_k + \int_{t_k}^{t_{k+1}} \mathbf{f}(\mathbf{x}(t), \mathbf{u}(t)) dt; \qquad \mathbf{x}_k = \mathbf{x}(t_k) \quad (5.10)$$

$$\mathbf{y}_k = \mathbf{g}(\mathbf{x}_k, \mathbf{u}_k); \qquad \mathbf{u}_k = \mathbf{u}(t_k) \quad (5.11)$$

$$\mathbf{v}_{k+1} = \mathbf{v}_k + \int_{t_k}^{t_{k+1}} \mathbf{h}(\mathbf{v}(t), \mathbf{q}(t)) dt; \qquad \mathbf{v}_k = \mathbf{v}(t_k) \quad (5.12)$$

$$\mathbf{q}_k = \xi(\mathbf{x}_k, \mathbf{u}_k); \quad (5.13)$$

and the constraints are:

$$0 \le \tilde{\mathbf{u}}_k < \tilde{\alpha}_k \quad (5.14)$$

$$0 \le \mathbf{h}(\mathbf{v}_k, \mathbf{q}(\mathbf{x}_k, t_k)) < \beta_k \qquad k=1, 2, \cdots, N \quad (5.15)$$

$$(\mathbf{v}_N - \mathbf{v}_o) < \Gamma \quad (5.16)$$

where N is the total number of discretized steps which represent the period from the initial time t_o to the final time t_f; Δt_k is the (possibly) non-uniform time interval, $\Delta t_k = t_{k+1} - t_k$, for k=1, 2, to N; $\mathbf{x}_k \in \Re^{n \times N}$ is the plant state vector; $\mathbf{y}_k \in \Re^{\ell \times N}$ is the plant output vector; $\mathbf{u}_k \in \Re^{m \times N}$ is the control input vector; $\mathbf{v}_k \in \Re^{r \times N}$ is the damage state vector; $\mathbf{q}_k \in \Re^{p \times N}$ is the structural output vector; $\tilde{\alpha}_k \in \Re^{m \times N}$ is the normalized natural bound vector of the valve positions; $\beta_k \in \Re^{r \times N}$ is specified tolerances for the damage rate vector; $\Gamma \in \Re^r$ is specified tolerances for accumulated damage vector; $\tilde{x}_k \in \Re^{n \times N}$ is the normalized deviations of plant state vector; $\tilde{y}_k \in \Re^{1 \times N}$ is the normalized deviations of selected plant output scalar which is oxygen/fuel (O_2 / H_2) mixture ratio, the second component of the plant output vector y_k as seen below in Eq. (5.17c); $\tilde{u}_k \in \Re^{m \times N}$ is the normalized deviations of control input vector. The definition of the above normalized vectors for k=1, 2, to N are given as:

$$\tilde{x}_k^i = (x_k^i - x_{ss}^i) / x_{ss}^i \qquad \mathbf{x}_k = [X_k^1, X_k^2, \cdots, X_k^n] \qquad i=1, 2, \cdots, n \quad (5.17a)$$

$$\tilde{y}_k = y_k^2 - y_{ss}^2 \qquad \mathbf{y}_k = [y_k^1, y_k^2, y_k^3, \cdots, y_k^\ell] \quad (5.17b)$$

$$\tilde{u}_k^i = (u_k^i - u_{ss}^i) / u_{ss}^i \qquad \mathbf{u}_k = [u_k^1, u_k^2, \cdots, u_k^m] \qquad i=1, 2, \cdots, m \quad (5.17c)$$

For simplicity, the matrices **M**, **Q**, S and **R** are chosen to be diagonal and constant. Furthermore, the matrices **M**, **Q** and **R** are normalized according to the non-dimensional vectors $\tilde{\mathbf{x}}_k$, and $\tilde{\mathbf{u}}_k$ in the cost functional J as described in Eq. (5.9).

$$\mathbf{Q}_{n \times n} = \left(\frac{1}{n + C_{33} - 1}\right) \mathrm{Diag}([1, 1, C_{33}, 1, \cdots, 1]) \quad \text{such that} \quad \mathrm{trace}(\mathbf{Q}) = 1 \quad (5.18a)$$

$$S = C_{SQ} \quad (5.18b)$$

$$\mathbf{R}_{m \times m} = \left(\frac{C_{RQ}}{m}\right) I_m \quad \text{such that} \quad \mathrm{trace}(\mathbf{R}) = C_{RQ} \quad (5.18c)$$

$$\mathbf{M}_{n \times n} = C_{MQ} \times Q_{n \times n} \quad \text{such that} \quad \mathrm{trace}(\mathbf{M}) = C_{MQ} \quad (5.18d)$$

where the scalar constants, C_{MQ}, C_{SQ} and C_{RQ} in the weighting matrices **M**, S and **R** represent their respective importance relative to the weighting matrix **Q**. This approach reduces the variety of choices for weighting matrices. The diagonal elements of the weighting matrix **Q** should be different because they correspond to the respective plant state variables which are not equally important for performance. In the present model, the main combustor pressure which is the third plant state variable is strongly related to the rocket engine performance. Therefore, the third diagonal element of **Q** is chosen to be larger than others, i.e., $C_{33} \geq 1$ in Eq. (5.18a).

For solving the nonlinear optimization problem, the scalar weighting parameters in matrices **M**, **Q**, S and **R** are chosen as $C_{33} = 30$; $C_{SQ} = 0.06$; $C_{RQ} = 0.002$ and $C_{MQ} = 0$. The optimal decision variables to be identified are the control inputs sequence $\{\mathbf{u}_k\}$ having the dimension of $m \times N$ for k=1, 2, ..., N. To accurately capture the fast dynamic response at an early stage of the transients, time steps Δt_k are chosen to be non-uniform as follows:

$$\Delta t_k = c\,\Delta t_{k-1} \tag{5.19}$$

where constant c>1 is the incremental ratio of two consecutive time steps. This setting of non-uniform time steps enhances the computational efficiency of numerical optimization process by reducing the total number steps of N (i.e., the dimension of the decision vector in optimization) for the same period $(t_f - t_o)$ without any significant loss of solution accuracy.

5.3 Optimization Results And Discussion

The purpose of these optimization studies is to examine the dynamic performance of reusable rocket engines and the fatigue and creep damage in the critical components. Based on the optimal control policy, the transients of the process variables and the resulting damage in the critical components were obtained by manipulating the two oxidizer valves in Fig. 2.1. The rocket engine is maneuvered from the initial equilibrium state of chamber pressure at 2700 psi and mixture ratio of 6.02 to the new equilibrium state of chamber pressure at 3000 psi and the same mixture ratio of 6.02 in 300 ms. The control commands to the two preburner oxidizer valves are updated at 37 discrete time instants (i.e., N=37) in which the parameters in Eq. (5.19) were selected as: c=1.035 and Δt_1=0.3 ms. The cost functional to be minimized is based on the deviations from the final equilibrium state at 3000 psi.

Optimization was carried out under different damage rate constraints and different initial damage in the critical plant components, namely, fuel turbine blades, oxidizer turbine blades, and the coolant channel ligament in the main thrust chamber. Pertinent results are presented in this section for four scenarios:

(i) Different creep damage constraints and a fixed initial creep damage in the ligament;

(ii) Different initial creep damage and a fixed creep damage constraint on the ligament;

(iii) Different fatigue damage constraints and a fixed initial fatigue damage on the fuel and oxidizer turbine blades; and

(iv) Different initial fatigue damage and a fixed fatigue damage constraint on the fuel and oxidizer turbine blades.

In the first two scenarios, no fatigue damage constraints were imposed on the fuel and oxidizer turbine blades, and the initial fatigue damage therein was held fixed. Optimization studies were also conducted under different fatigue damage constraints and initial fatigue damage in the fuel and oxidizer turbine blades. These results, corresponding to the last two scenarios, are extension of those reported in a previous publication (Dai and Ray, 1994b) where no creep damage constraints were imposed on the coolant channel, and the initial creep damage was held fixed.

Visco-elasto-plastic parameters of oxygen-free high-conductivity copper (Freed and Verrilli, 1988), which is a material for the coolant channel ligament, have been used in these optimization studies. However, the fatigue damage parameters of the turbine blades are based on the properties of AISI 4340 steel due to unavailability of the parameters of an appropriate turbine blade material such as Inconel 718 or MAR-M-246. Therefore, precise conclusions regarding the blade fatigue damage cannot be made based on these optimization results unless the actual damage parameters are used.

5.3.1 Different Creep Damage Constraints on the Coolant Channel Ligament

For a given initial creep damage, three cases with different creep damage rate constraints in the coolant channel ligament are presented in this section. The initial fatigue damage in the fuel and oxidizer turbine blades are set to $D_{o,H_2} = D_{o,O_2} = 0.1$ in each of these three cases, and no fatigue damage constraints are imposed. The initial damage and constrained damage rates for both coolant channel ligament and turbines blades are listed in Table 5.1.

Table 5.1 Damage rate constraints $\beta(t)$ and initial damage $\mathbf{D_o}$ under Simulation Condition 1

Simulation Condition 1	H_2 Turbine $\beta_{H_2}(t)$ / D_{o,H_2}	O_2 Turbine $\beta_{O_2}(t)$ / D_{o,O_2}	Coolant Channel Ligament $\beta_{Cr}(t)$ / $D_{o,Cr}$
Case 1A	Unconstrained / 0.1	Unconstrained / 0.1	**Unconstrained** / 0.008759
Case 1B	Unconstrained / 0.1	Unconstrained / 0.1	**1.3**×10-**3 sec-1** / 0.008759
Case 1C	Unconstrained / 0.1	Unconstrained / 0.1	**0.6**×10-**3 sec-1** / 0.008759

The transients in Figs. 5.2 to 5.7 exhibit the dynamics of various engine variables and the damage resulting from optimization over the time period of 0 to 300 ms where the control action is updated at the thirty seven non-uniformly spaced discrete instants of time. Fig. 5.2 shows the transients of the creep damage rate and accumulation in the coolant channel ligament corresponding to the constraints laid out in Table 5.1. The creep damage rate is restrained within the prescribed constraints, and the accumulated creep damage in the coolant channel ligament is monotonically decreased as the constraint is made stronger. Therefore, the service life of main thrust chamber can be extended by imposing the constraints on the creep damage rate. For the same initial creep damage in the ligament, the creep damage rates near the final equilibrium state are almost identical for all three cases in Table 5.1; and the growth rates of creep damage accumulation are not much different except during the initial transition period. The peak of the creep damage rate occurs between about 10 ms and 30 ms, which follows the dynamic response of input variables to the creep damage life prediction model, i.e., the temperature and pressure loading on the coolant channel ligament.

Fig. 5.3 presents the input variables to the creep damage model, namely, the hot-side wall temperature, cold-side wall temperature, and pressure difference acting on the ligament. It is the temperature and pressure variations that cause the creep ratcheting and progressive thinning of the ligament as discussed in Chapter 4. To reduce the creep damage accumulation in the ligament, the transient oscillations of the thermo-mechanical loading (i.e., wall temperatures and pressures) need to be controlled by constraining the creep damage rate. The oscillations in the cold-side wall temperature are indeed reduced for the constrained cases as seen in Fig. 5.3, and similar effects are observed for the pressure difference and the hot-side wall temperature.

The transients of the mean stress, fatigue damage rate, and fatigue damage accumulation for the fuel and oxidizer turbine blades are shown in Figs. 5.4 and 5.5, respectively, under different creep damage constraints on the ligament. The peak of mean stress in the fuel turbine blades occur at about 15 ms for the unconstrained case 1A, and at about 35 ms and 90 ms for the

constrained cases 1B and 1C as shown in Fig. 5.4. Similar results are observed for the oxidizer turbine in Fig. 5.5. The rationale is that the mean stress and stress amplitude in the blades are directly related to the turbine torque and turbine shaft speed. Since the fatigue damage rate in the turbine blades is largely determined by instantaneous values of the mean stress and stress amplitude, peaks of the fatigue damage rate occur in synchronism with the peaks of the mean stress. Following the mean stress transients, the accumulated fatigue damage is reduced and slowed down for the constrained cases as seen in Figs. 5.4. and 5.5. The optimization results also indicate that constraining the creep damage rate in the coolant channel ligament has a direct effect on the fatigue damage in the fuel and oxidizer turbine blades although no fatigue damage constraints are imposed on the turbine blades. By imposing a constraint on the creep damage rate, the service life of the coolant channel is increased along with simultaneous increase in the service lives of both the fuel and oxidizer turbines. The fatigue damage accumulation in the turbine blades under the creep damage constraint in the ligament (Case 1C) are about one-sixth and one-third of that under the unconstrained case respectively (Case 1A).

Figs. 5.6 and 5.7 show how the plant dynamic performance is influenced by different creep damage constraints in the ligament. The transients of the oxygen flow rates into the main thrust chamber, fuel preburner, and oxidizer preburner are presented in Fig. 5.6. The overall system response becomes more sluggish as the damage rate constraint is made stronger. The resulting transients of the key process variables, namely, O_2 / H_2 mixture ratio and the hot-gas pressure and temperature in the main thrust chamber, are shown in Fig. 5.7. As expected, for a given initial damage, both pressure and temperature dynamics tend to become slower as the service lives of the main thrust chamber and turbines are increased. The thrust chamber pressure is seen to rise monotonically in all cases except for a small dip during early transients. For a given preburner pressure, a reduction in the thrust chamber pressure causes an increase in the turbine torque which, in turn, increases the pressure load acting on the turbine blades. Therefore, the dip in the thrust chamber pressure at about 10 ms in Fig. 5.7 is also responsible for the peak mean stress in the fuel turbine blades for the unconstrained case. Furthermore, the net excursion of the O_2 / H_2 ratio is in the range of 5.9 to 6.4 for the unconstrained case, and is improved to 5.9 to 6.04 for the constrained case during the up-thrust transients of the rocket engine. The overshoot in the thrust chamber hot-gas temperature at about 10 ms for the unconstrained case is reduced and shifted to about 40 ms and 90 ms for the constrained cases 1B and 1C.

5.3.2 Different Initial Values of Creep Damage in the Coolant Channel Ligament

This section presents three cases with different initial creep damage under the same constraint of the creep damage rate in the coolant channel ligament. The initial fatigue damage and the damage rate constraints for the fuel and oxidizer turbine blades are kept the same for all three cases. The initial values of creep damage accumulation in the ligament, $D_{o,Cr}$, represent the damage conditions at the end of the 1st, 100th, and 200th firing cycles, respectively, as discussed in Chapter 4. These constraints are listed in Table 5.2.

Table 5.2. Damage rate constraints $\beta(t)$ and initial damage $\mathbf{D_o}$ under Simulation Condition 2

Simulation Condition 2	H_2 Turbine $\beta_{H_2}(t)$ / D_{o,H_2}	O_2 Turbine $\beta_{O_2}(t)$ / D_{o,O_2}	Coolant Channel Ligament $\beta_{Cr}(t)$ / $D_{o,Cr}$
Case 2A	Unconstrained / 0.1	Unconstrained / 0.1	1.3×10^{-3} sec^{-1} / **0.008759**
Case 2B	Unconstrained / 0.1	Unconstrained / 0.1	1.3×10^{-3} sec^{-1} / **0.189305**
Case 2C	Unconstrained / 0.1	Unconstrained / 0.1	1.3×10^{-3} sec^{-1} / **0.459618**

The results generated under the simulation condition 2 in Table 5.2 are presented in Figs. 5.8 to 5.13. The creep damage rate and accumulation in the ligament is shown in Fig. 5.8 for different initial creep damage. The growth of creep damage accumulation for a larger initial damage is faster than that for a smaller initial damage under a given constraint of the creep damage rate. The rationale is that, under a severe thermo-mechanical loading condition, structural behavior of the ligament is nonlinear due to a combination of geometric deformation and viscoplasticity. Specifically, initial conditions of the inelastic strain state vector and initial creep damage based on the current shape of the ligament are responsible for this nonlinear creep damage behavior. The above results indicate that the ligament shape is a critical factor for the creep damage model developed in the Chapter 3 and Chapter 4.

Figs. 5.9 and 5.10 exhibit the transients of mean stress and fatigue damage in the fuel and oxidizer turbine blades for different initial creep damage in the ligament. The accumulated fatigue damage in the turbine blades for larger initial creep damage (Case 2C) is about half of that for a smaller initial damage (Case 2A) under the identical constraint. The reason for this behavior is that, for a given creep damage rate constraint, the plant response shown in Figs. 5.11 to 5.13 become more restricted due to the increasing creep damage rate for a larger initial damage as seen in Fig. 5.8. Consequently, the fatigue damage accumulation in the turbine blades are reduced due to the restricted plant operations as seen in Figs. 5.9 and 5.10. The transients of the key plant variables are shown in Figs. 5.11 to 5.13 for different initial creep damage under the same creep damage rate constraints in the ligament. In general, the plant response becomes more sluggish for larger initial creep damage in the ligament, which is similar to what was discussed for the constrained cases in the previous simulation.

The above observations suggest that both initial damage and constraints are critical factors in the synthesis of a damage mitigating control law. The damage constraints in the critical components should be selected based on the corresponding initial damage. For example, if the goal is to maintain the plant performance at a constant level, then the damage constraints have to relaxed as the initial damage increases. In that case, the remaining service life will be depleted faster as the damage accumulates. On the other hand, if the goal is to maintain a constant depletion rate of the service life, the constraints need to be made stronger as the initial damage increases. In that case, the plant performance will be degraded as the damage accumulates.

5.3.3 Different Fatigue Damage Constraints on the Fuel and Oxidizer Turbine Blades

Ray et al. (1994c) have reported the simulation results using a similar rocket engine model for different fatigue damage rate constraints on the fuel and oxidizer turbine blades without considering the creep damage in the coolant channel ligament. This section expands these previous results by including the effects of ligament creep damage. The initial creep damage and constraints on the creep damage rate of the ligament are identical for all three cases. The constrained damage rates and initial damage are listed in Table 5.3.

Table 5.3. Damage rate constraints $\beta(t)$ and initial damage $\mathbf{D_o}$ under Simulation Condition 3

Simulation Condition 3	H_2 Turbine $\beta_{H_2}(t)$ / D_{o,H_2}	O_2 Turbine $\beta_{O_2}(t)$ / D_{o,O_2}	Coolant Channel Ligament $\beta_{Cr}(t)$ / $D_{o,Cr}$
Case 3A	**Unconstrained** / 0.1	**Unconstrained** / 0.1	Unconstrained / 0.008759
Case 3B	**5.0**×10-4 **sec^{-1}** / 0.1	**5.0**×10-4 **sec^{-1}** / 0.1	Unconstrained / 0.008759
Case 3C	**1.0**×10^{-4} **sec^{-1}** / 0.1	**1.0**×10^{-4} **sec^{-1}** / 0.1	Unconstrained / 0.008759

The transients in Figs. 5.14 to 5.19 show the plant performance and damage characteristics corresponding to the different fatigue damage rate constraints in the turbine blades. The plant dynamic response in Figs. 5.14 and 5.15 become slightly slower as the damage rate constraints in

both the fuel and oxidizer turbine blades are imposed. Transients of individual process variables under different constraints are largely similar except for the initial transients. Fig. 5.15 shows the transients of the mixture ratio, gas pressure and temperature in the main thrust chamber for the simulation condition 3 in Table 5.3. These results are qualitatively similar to those under different creep damage rate constraints on the ligament for the simulation condition 1 in Table 5.1. The overshoot in the mixture ratio occurs at about 10 ms when the oxidizer turbopump demands more torque to increase its speed so that the pump pressure can be elevated to generate a higher value of oxygen flow for the desired mixture ratio.

Figs. 5.16 and 5.17 show the transients of the mean stress, maximum fatigue damage rate, and accumulated fatigue damage on the fuel and oxidizer turbine blades. The sharp increase in the blade mean stress is the cause of enhanced damage in the turbine blades. The fatigue damage accumulation in the turbine blades virtually takes place during this short interval (about 0 to 40 ms). The damage accumulation in both the turbine blades for the unconstrained case is seen to be about five times larger than that for the constrained case.

The transients of the creep damage model inputs, namely, wall temperature and pressure difference, and outputs, namely, creep damage rate and accumulation, are shown in Figs. 5.18 and 5.19, respectively. The constraints on turbine blade fatigue damage apparently have no significant bearing on the ligament creep damage.

5.3.4 Different Initial Values of Fatigue Damage in the Fuel and Oxidizer Turbine Blades

The effects of ligament creep damage are included in this section to expand the results of different initial fatigue damage on the fuel and oxidizer turbine blades as reported by Ray et al. (1994c). No constraints are imposed on the creep damage rate. The initial fatigue and creep and damage and constraints on the fatigue damage are listed below in Table 5.4 for three cases.

Table 5.4 Damage rate constraints $\beta(t)$ and initial damage $\mathbf{D_o}$ under Simulation Condition 4

Simulation Condition 4	H_2 Turbine $\beta_{H_2}(t)$ / D_{o,H_2}	O_2 Turbine $\beta_{O_2}(t)$ / D_{o,O_2}	Coolant Channel Ligament $\beta_{Cr}(t)$ / $D_{o,Cr}$
Case 4A	1.0×10^{-4} sec^{-1} / **0.01**	1.0×10^{-4} sec^{-1} / **0.01**	Unconstrained / 0.0087589
Case 4B	1.0×10^{-4} sec^{-1} / **0.05**	1.0×10^{-4} sec^{-1} / **0.05**	Unconstrained / 0.0087589
Case 4C	1.0×10^{-4} sec^{-1} / **0.1**	1.0×10^{-4} sec^{-1} / **0.1**	Unconstrained / 0.0087589

Figs. 5.20 and 5.21 show the transients of the mean stress, fatigue damage rate, and accumulated fatigue damage in the fuel and oxidizer turbine blades. For the initial damage of 0.01, the damage rate for both turbines is less than the limit of the constraint even though the peak of mean stress is the largest. This phenomenon is a consequence of a relatively small slope in the nonlinear damage curve at early stages of the fatigue life in high-strength materials which implies that, for a given stress amplitude, the fatigue damage rate increases with as the fatigue damage accumulates. This dependence on the initial fatigue damage is due to the γ-parameter in the nonlinear fatigue damage model presented in Section 3.1.

The transients in Figs. 5.22 and 5.23 show the plant performance for different initial fatigue damage in the fuel and oxidizer turbine blades, respectively. The overall system response becomes slightly sluggish as the initial damage on both the turbine blades increase for the reason stated earlier in Section 5.3.2. The transients of the wall temperature, pressure difference across the ligament, and the creep damage rate and accumulation of the ligament are shown in Figs. 5.24 and 5.25. The observation is that different values of initial fatigue damage on turbine blades have no significant influence on the ligament creep damage.

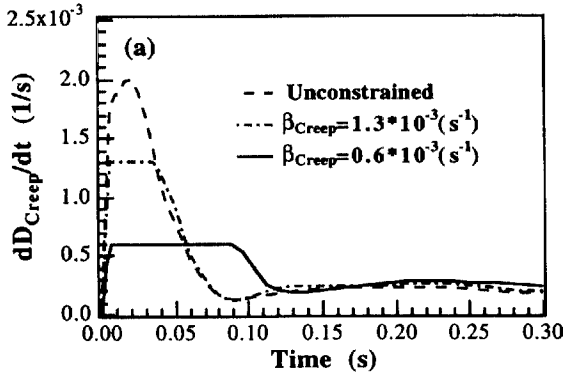

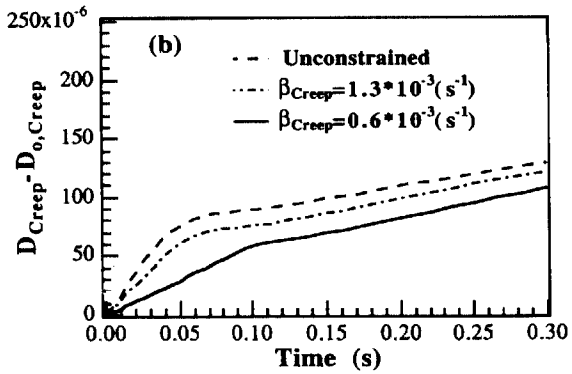

Fig. 5.2 Transients of creep damage of the ligament
(a) creep damage rate dD_{Creep}/dt (1/s)
(b) increment in accumulated creep damage

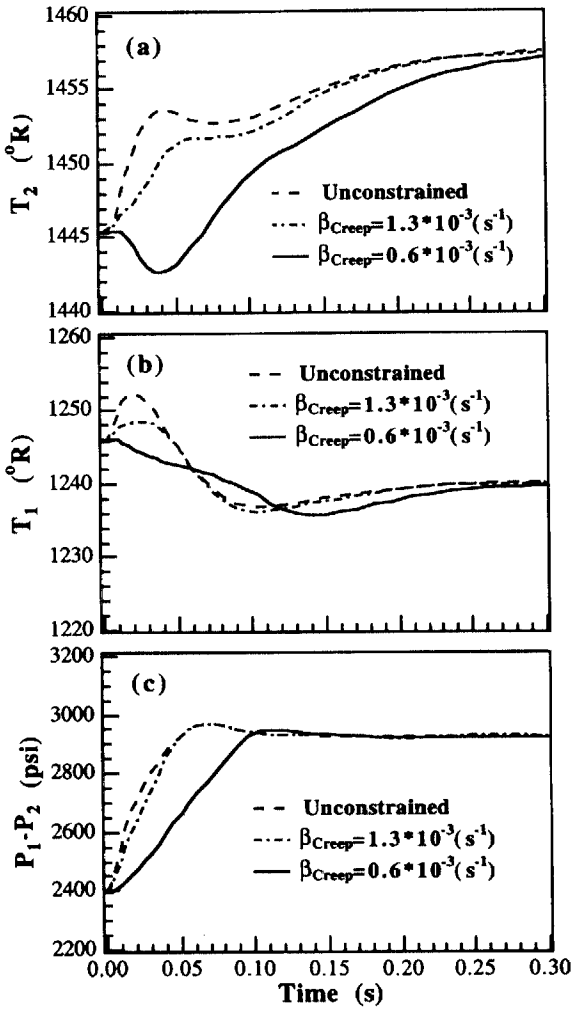

Fig. 5.3 Transients of inputs to creep damage model
(a) hot-side wall temperature T_2 (°R)
(b) cold-side wall temperature T_1 (°R)
(c) pressure diff. across the ligament $P_1 - P_2$ (psi)

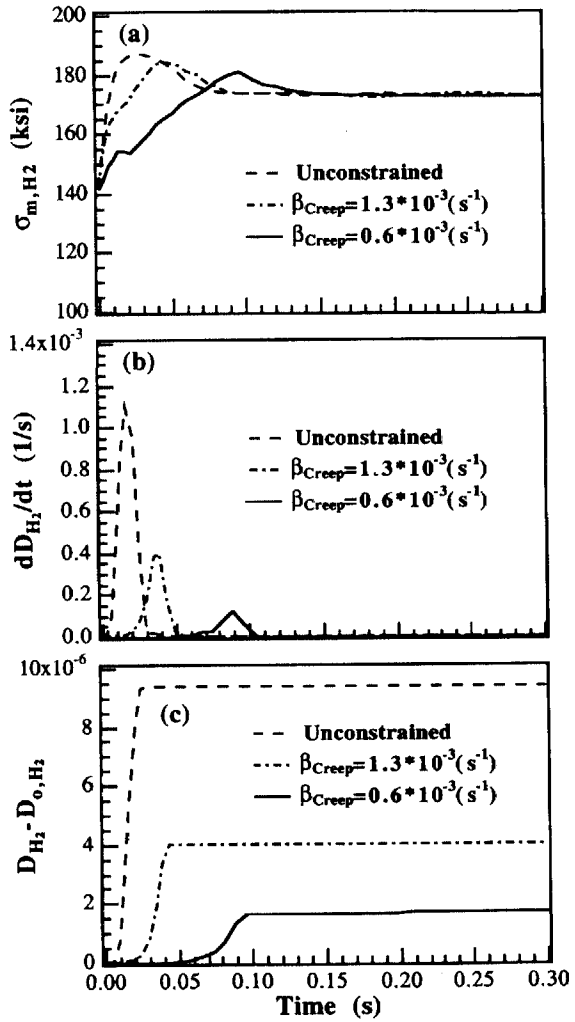

Fig. 5.4 Transients of hydrogen turbine
(a) mean stress σ_{m,H_2} (ksi)
(b) maximum fatigue damage rate (1/sec)
(c) increment in accumulated fatigue damage

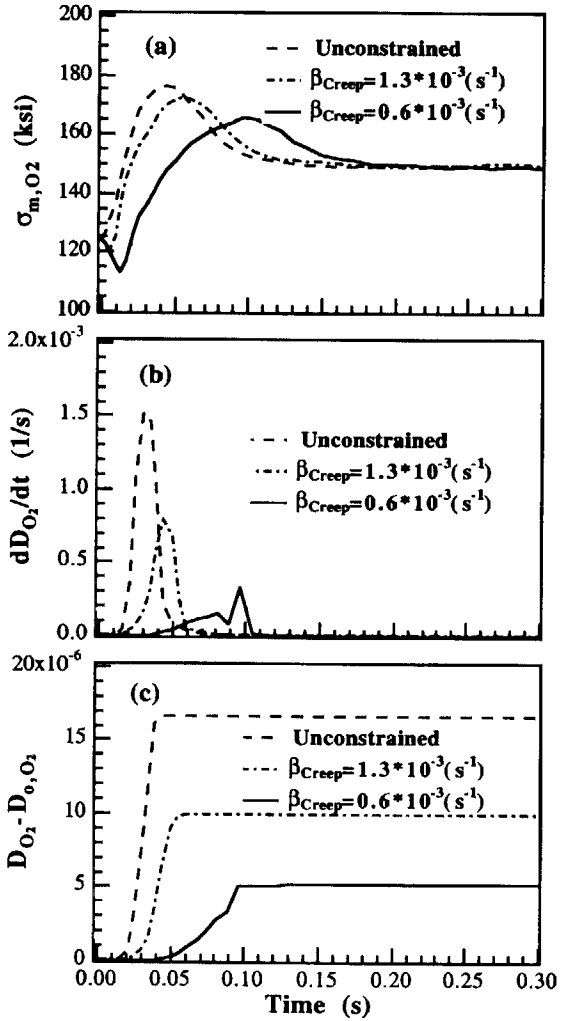

Fig. 5.5 Transients of oxidizer turbine

(a) mean stress σ_{m,O_2} (ksi)
(b) maximum fatigue damage rate (1/sec)
(c) increment in accumulated fatigue damage

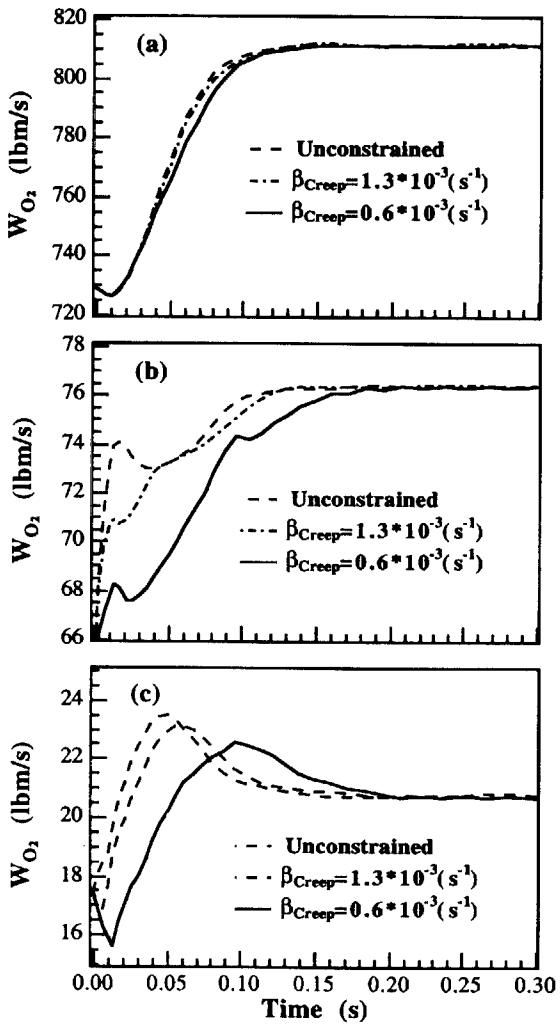

Fig. 5.6 Transients of oxygen flow rate W_{O_2} (lbm/s)

(a) into main combustor
(b) into fuel preburner
(c) into oxidizer preburner

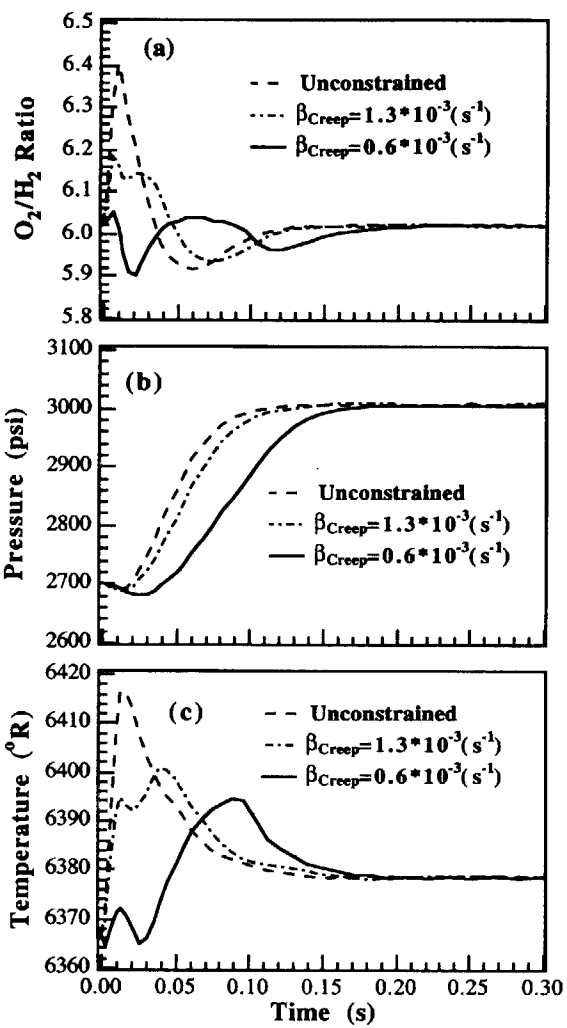

Fig. 5.7 Transients of plant performance

(a) oxygen/hydrogen ratio
(b) main combustor hot-gas pressure (psi)
(c) main combustor hot-gas temperature (°R)

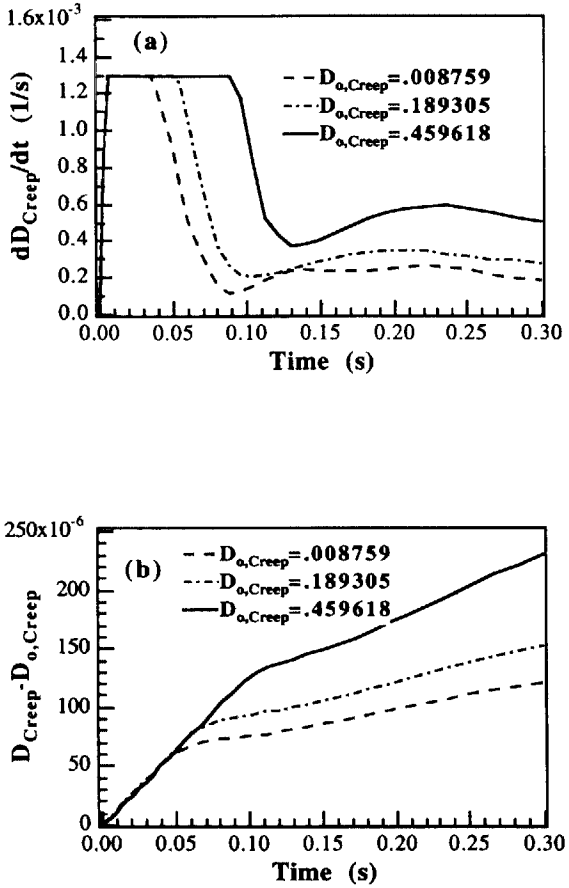

Fig. 5.8 Transients of creep damage of the ligament
(a) creep damage rate dD_{Creep}/dt (1/sec)
(b) increment in accumulated creep damage

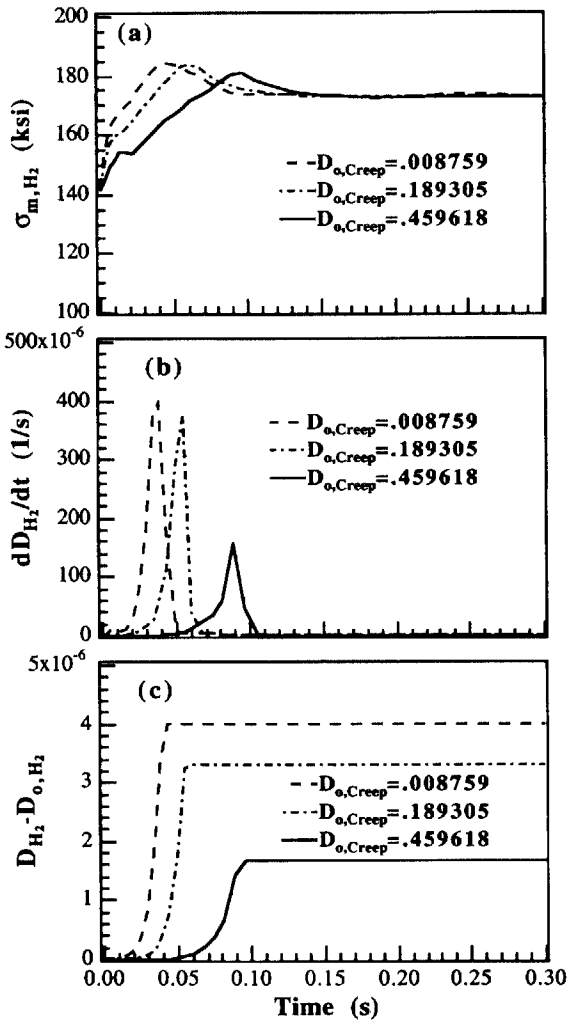

Fig. 5.9 Transients of hydrogen turbine
(a) mean stress σ_{m,H_2} (ksi)
(b) maximum fatigue damage rate (1/sec)
(c) increment in accumulated fatigue damage

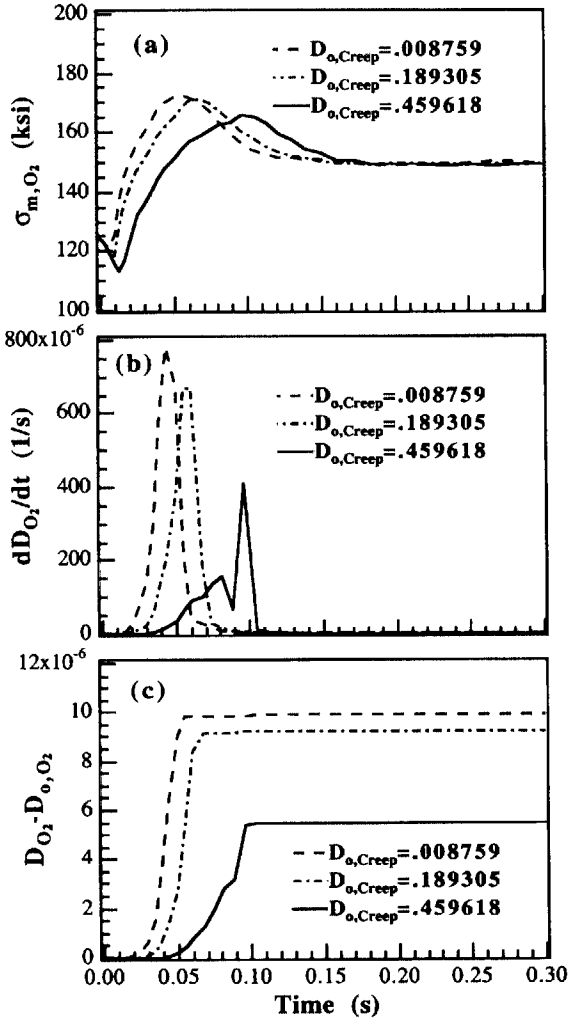

Fig. 5.10 Transients of oxidizer turbine
(a) mean stress σ_{m,H_2} (ksi)
(b) maximum fatigue damage rate (1/sec)
(c) increment in accumulated fatigue damage

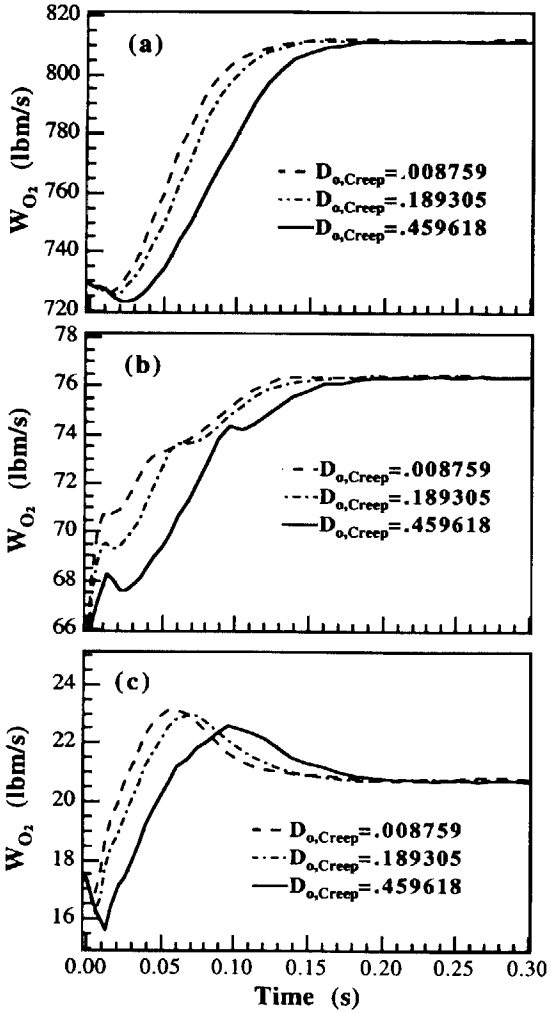

Fig. 5.11 Transients of oxygen flow rate W_{O_2} (lbm / s)

(a) into main combustor
(b) into fuel preburner
(c) into oxidizer preburner

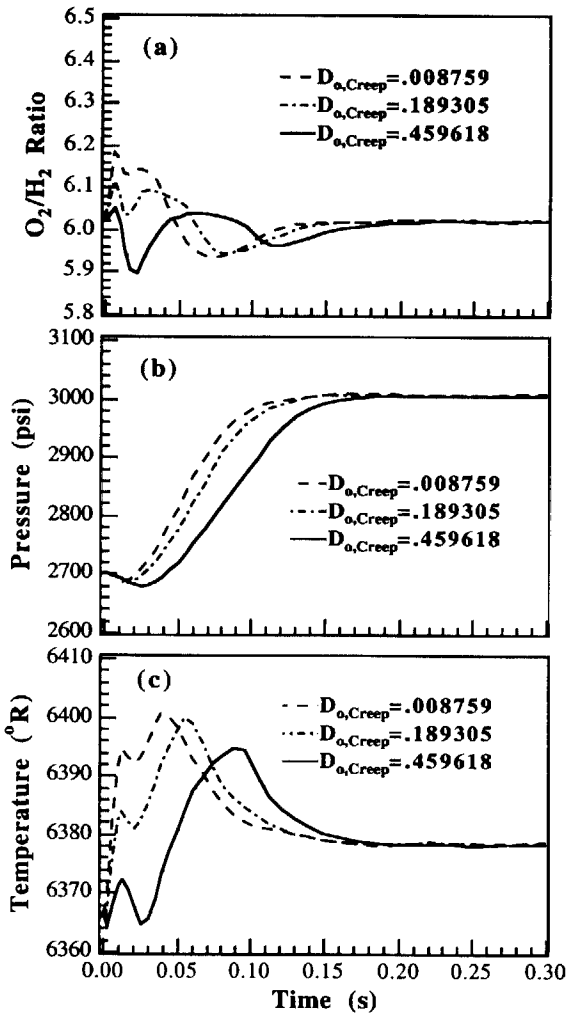

Fig. 5.12 Transients of plant performance

(a) oxygen/hydrogen ratio
(b) main combustor hot-gas pressure (psi)
(c) main combustor hot-gas temperature (°R)

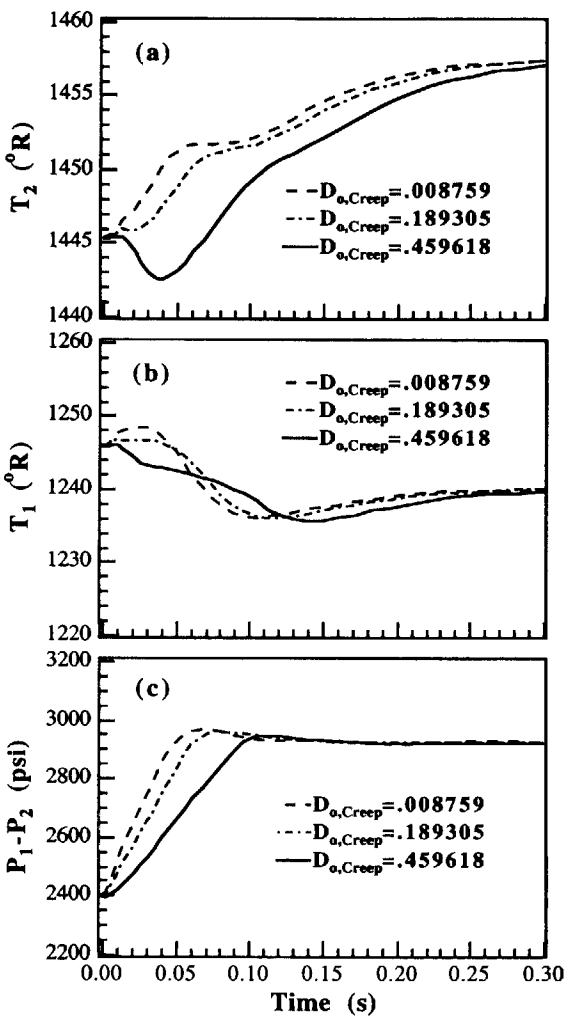

Fig. 5.13 Transients of inputs to creep damage model

(a) hot-side wall temperature T_2 (°R)
(b) cold-side wall temperature T_1 (°R)
c) pressure diff. across the ligament $P_1 - P_2$ (psi)

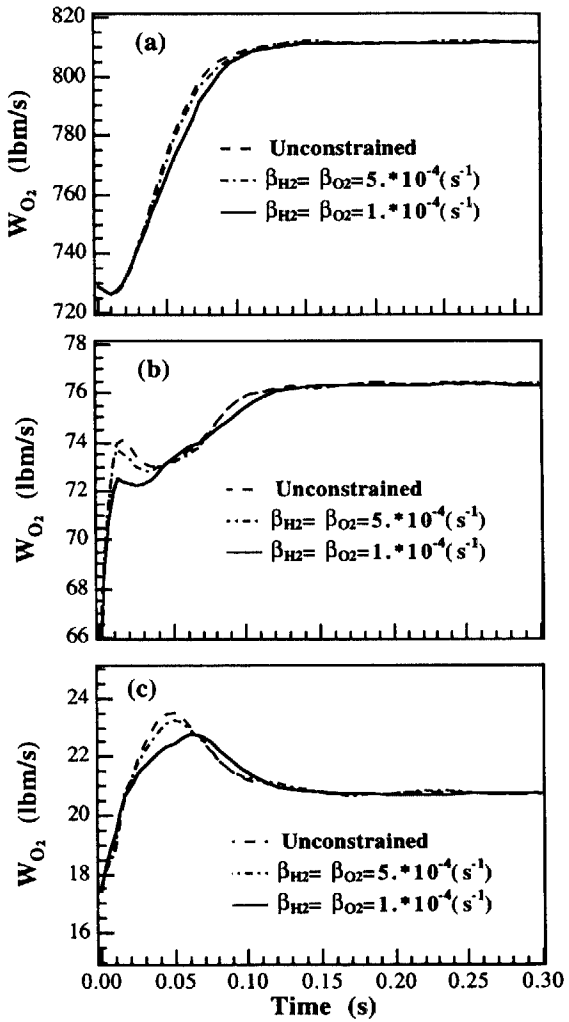

Fig. 5.14 Transients of oxygen flow rate W_{O_2} (lbm / s)

(a) into main combustor

(b) into fuel preburner

(c) into oxidizer preburner

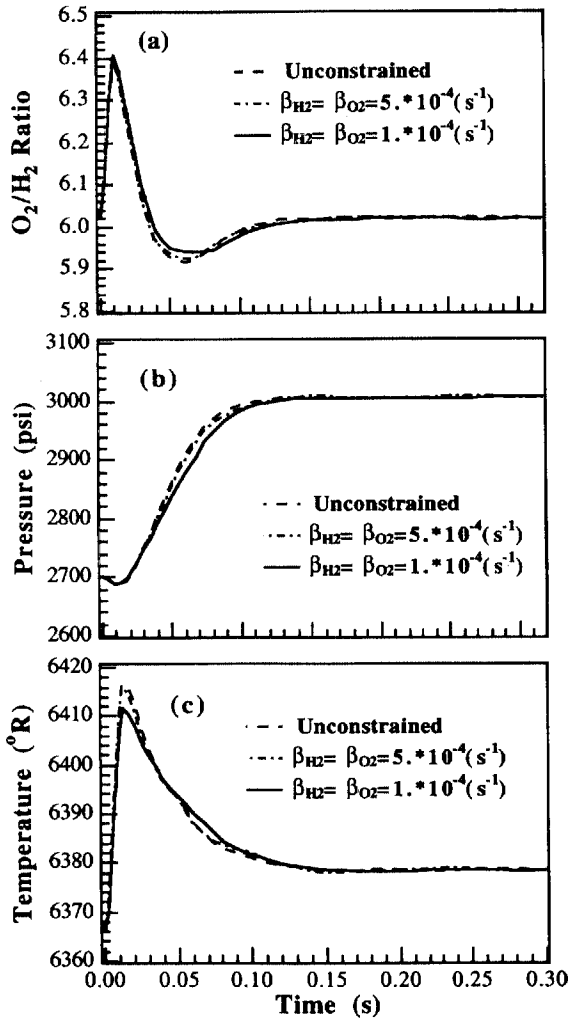

Fig. 5.15 Transients of plant performance

(a) oxygen/hydrogen ratio

(b) main combustor hot-gas pressure (psi)

(c) main combustor hot-gas temperature (°R)

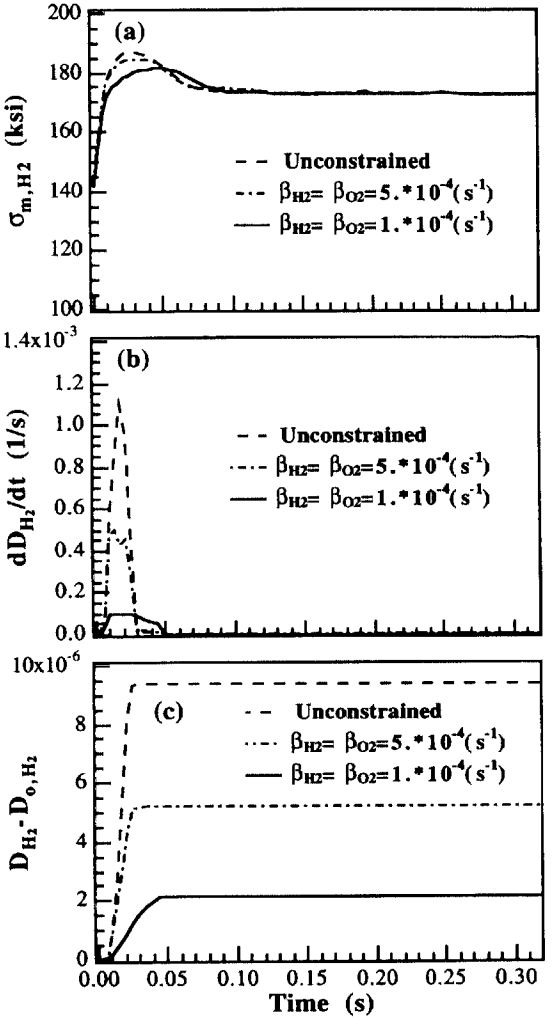

Fig. 5.16 Transients of hydrogen turbine

(a) mean stress σ_{m,H_2} (ksi)

(b) maximum fatigue damage rate (1/sec)

(c) increment in accumulated fatigue damage

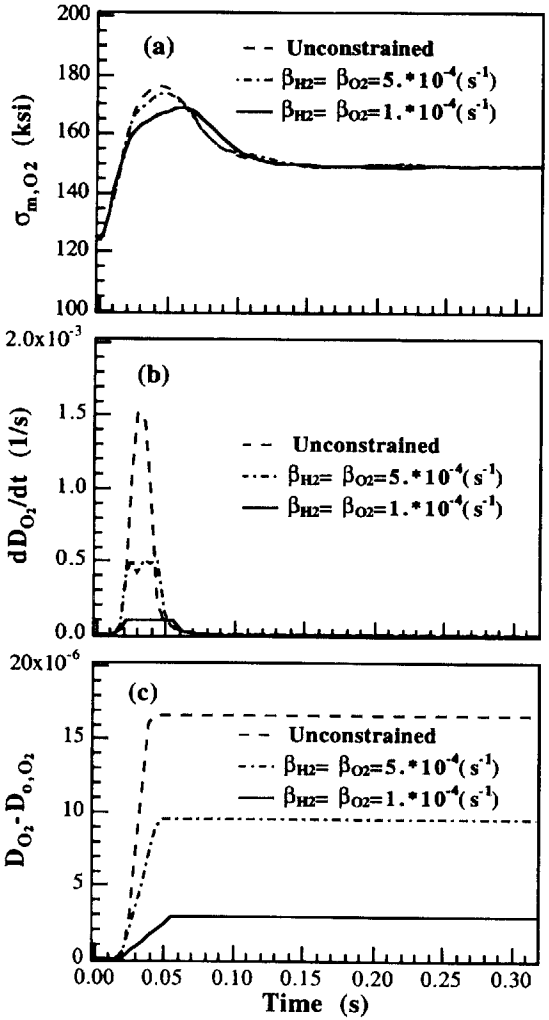

Fig. 5.17 Transients of oxidizer turbine
(a) mean stress σ_{m,H_2} (ksi)
(b) maximum fatigue damage rate (1/sec)
(c) increment in accumulated fatigue damage

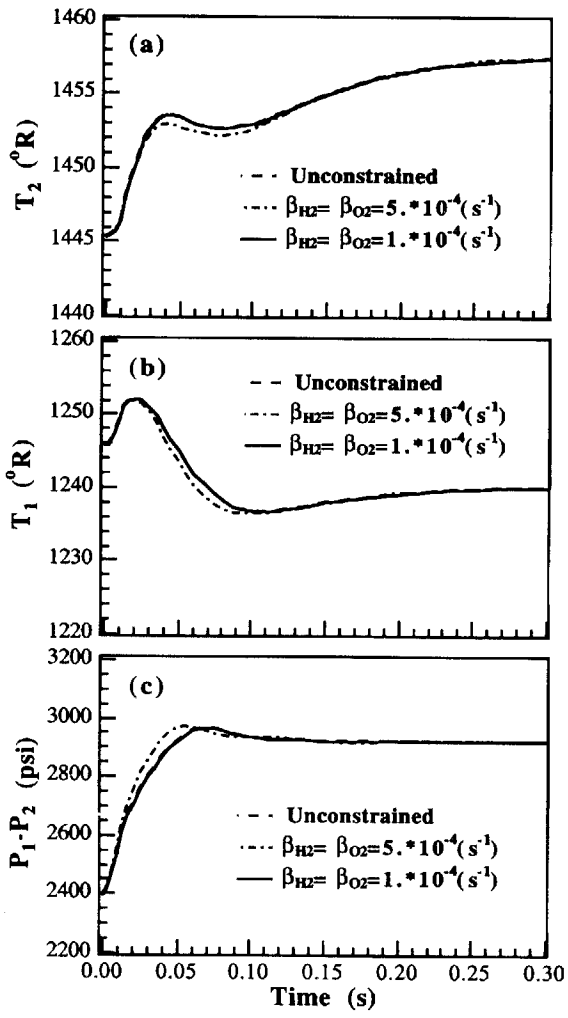

Fig. 5.18 Transients of inputs to creep damage model
(a) hot-side wall temperature T_2 (^{o}R)
(b) cold-side wall temperature T_1 (^{o}R)
(c) pressure diff. across the ligament P_1 - P_2 (psi)

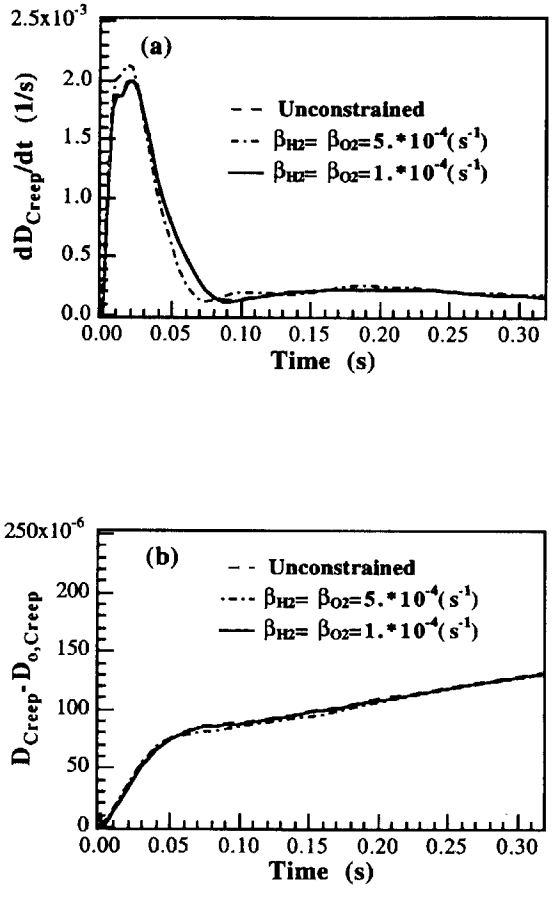

Fig. 5.19 Transients of creep damage of the ligament
(a) creep damage rate dD_{Creep} / dt (1/sec)
(b) increment in accumulated creep damage

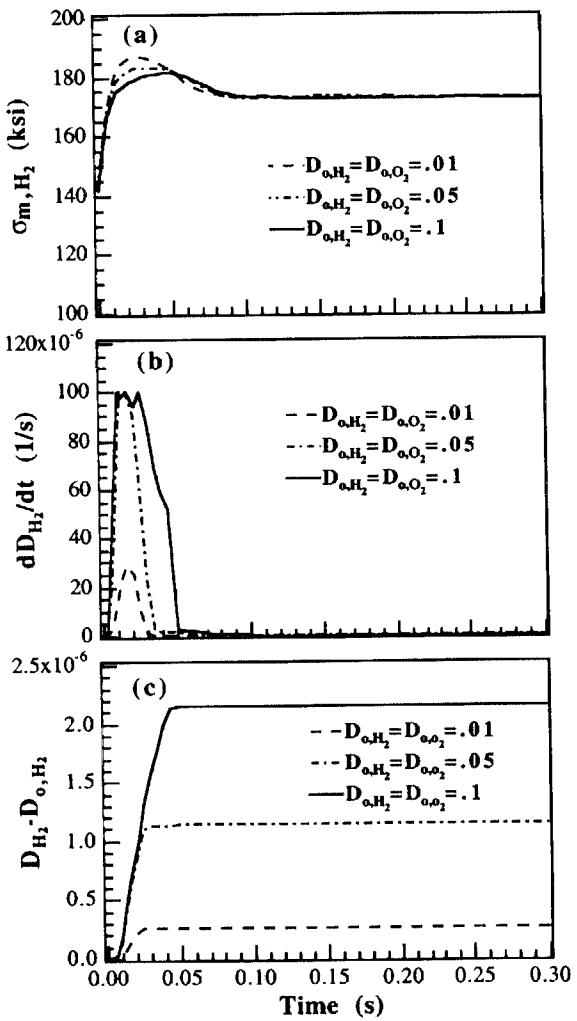

Fig. 5.20 Transients of hydrogen turbine

(a) mean stress σ_{m,O_2} (ksi)

(b) maximum fatigue damage rate (1/sec)

(c) increment in accumulated fatigue damage

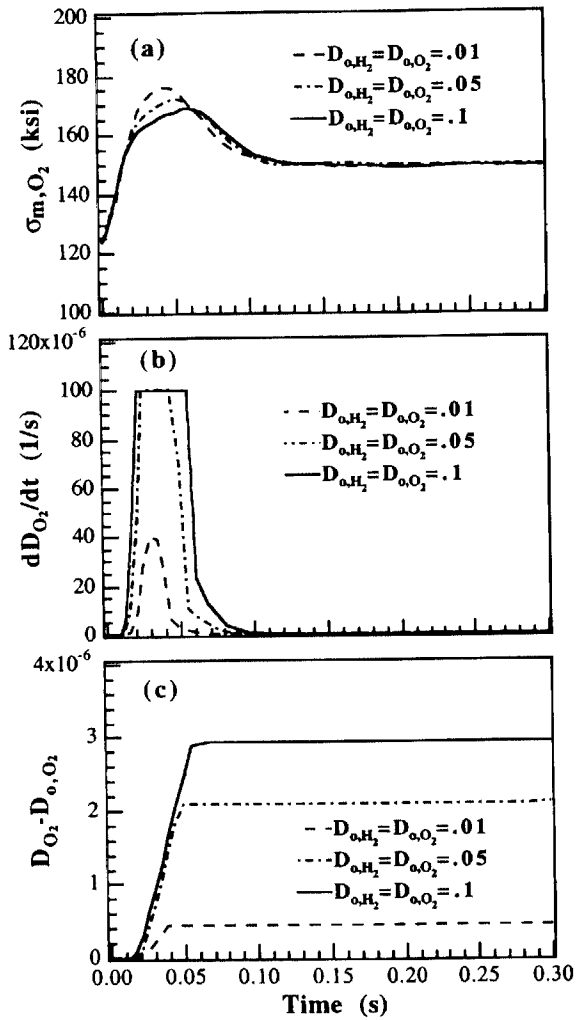

Fig. 5.21 Transients of oxidizer turbine

(a) mean stress σ_{m,O_2} (ksi)

(b) imaximum fatigue damage rate (1/sec)

(c) increment in accumulated fatigue damage

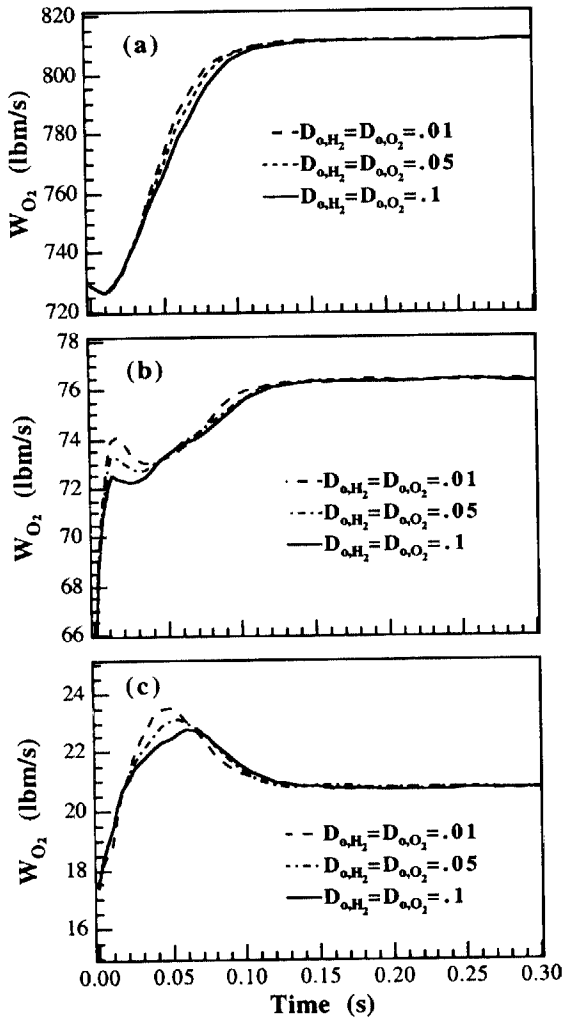

Fig. 5.22 Transients of oxygen flow rate W_{O_2} (lbm/s)

(a) into main combustor

(b) into fuel preburner

(c) into oxidizer preburner

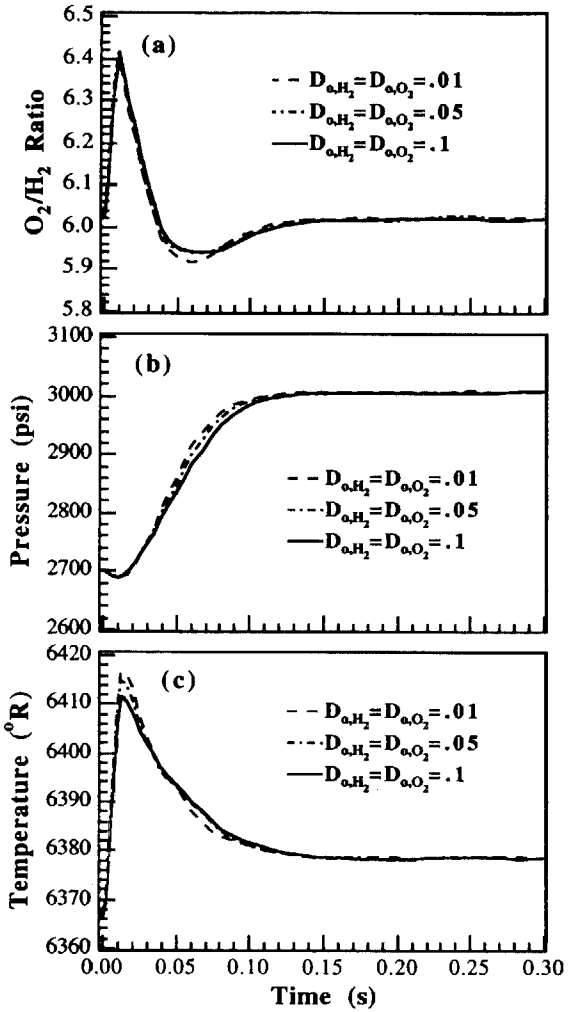

Fig. 5.23 Transients of plant performance
(a) oxygen/hydrogen ratio
(b) main combustor hot-gas pressure (psi)
(c) main combustor hot-gas temperature (°R)

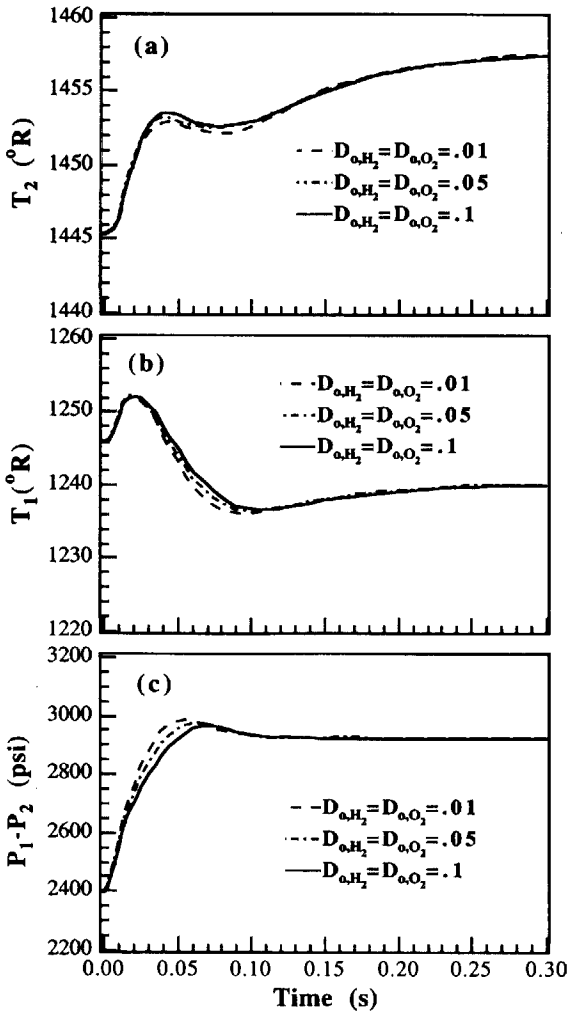

Fig. 5.24 Transients of inputs to creep damage model
(a) hot-side wall temperature T_2(°R)
(b) cold-side wall temperature T_1(°R)
(c) pressure diff. across the ligament P_1 - P_2 (psi)

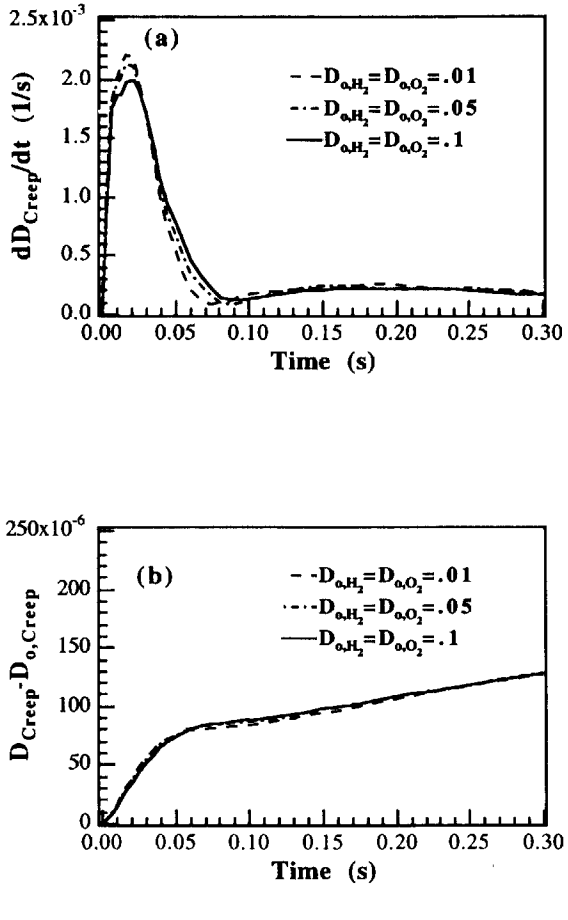

Fig. 5.25 Transients of creep damage of the ligament
(a) creep damage rate dD_{Creep}/dt (1/sec)
(b) increment in accumulated creep damage

5.4 Parametric Studies on Feedforward Optimal Control Policy

A series of optimization studies were conducted to examine the dynamic performance of the rocket engine while the creep damage rate on the coolant channel ligament were constrained under the different initial creep damage values, where no fatigue damage constraints were imposed on the fuel and oxidizer turbine blades, and the initial fatigue damage therein was held fixed. The selection of the weighting matrices, numerical methods, and the results are described in detail by Dai and Ray (1994b).

The results of optimization are presented for different initial conditions and constraints of creep damage in the coolant channel ligament while the fatigue damage in the oxidizer and fuel turbine blades are unconstrained. Pertinent results are presented in a condensed form in Fig. 5.26 for 15 cases with five different creep damage rate constraints on the coolant channel ligament for three different initial values of creep damage. The initial fatigue damage in the fuel and oxidizer turbine blades are set to $D_{o,H_2} = D_{o,O_2} = 0.1$, and no fatigue damage constraints are imposed in each of these cases listed in Table 5.5.

Table 5.5 The damage rate constraints $\beta(t)$ and initial damage D_o for 15 cases with five different constraints and three different initial damages

Simulation Condition	H_2 Turbine $\beta_{H_2}(t)$ / D_{o,H_2}	O_2 Turbine $\beta_{O_2}(t)$ / D_{o,O_2}	Coolant Channel Ligament $\beta_{Creep}(t)$ / $D_{o,Creep}$
Case c0A	Unconstrained / 0.1	Unconstrained / 0.1	Unconstrained / 0.008759
Case c1A	Unconstrained / 0.1	Unconstrained / 0.1	1.65×10^{-3} sec^{-1} / 0.008759
Case c2A	Unconstrained / 0.1	Unconstrained / 0.1	1.30×10^{-3} sec^{-1} / 0.008759
Case c3A	Unconstrained / 0.1	Unconstrained / 0.1	0.95×10^{-3} sec^{-1} / 0.008759
Case c4A	Unconstrained / 0.1	Unconstrained / 0.1	0.60×10^{-3} sec^{-1} / 0.008759
Case c0B	Unconstrained / 0.1	Unconstrained / 0.1	Unconstrained / 0.189305
Case c1B	Unconstrained / 0.1	Unconstrained / 0.1	1.65×10^{-3} sec^{-1} / 0.189305
Case c2B	Unconstrained / 0.1	Unconstrained / 0.1	1.30×10^{-3} sec^{-1} / 0.189305
Case c3B	Unconstrained / 0.1	Unconstrained / 0.1	0.95×10^{-3} sec^{-1} / 0.189305
Case c4B	Unconstrained / 0.1	Unconstrained / 0.1	0.60×10^{-3} sec^{-1} / 0.189305
Case c0C	Unconstrained / 0.1	Unconstrained / 0.1	Unconstrained / 0.459618
Case c1C	Unconstrained / 0.1	Unconstrained / 0.1	1.65×10^{-3} sec^{-1} / 0.459618
Case c2C	Unconstrained / 0.1	Unconstrained / 0.1	1.30×10^{-3} sec^{-1} / 0.459618
Case c4C	Unconstrained / 0.1	Unconstrained / 0.1	0.95×10^{-3} sec^{-1} / 0.459618
Case c4C	Unconstrained / 0.1	Unconstrained / 0.1	0.60×10^{-3} sec^{-1} / 0.459618

Fig. 5.26 summarizes the results of synthesizing an optimal policy for open loop control of up-thrust transients of the rocket engine in terms of normalized performance penalty, $J_n \equiv J / J^*$ vs. normalized creep damage, $D_n \equiv (D_{cr} - D_{cr,o}) / (D^*_{cr} - D^*_{cr,o})$ in the coolant channel ligament of the main thrust chamber. The nominal condition, indicated by $*$, corresponds to the rated design condition with no damage constraints as seen in Case c1A of Table 5.5. The three thick lines in Fig. 5.26 correspond to three different initial values of creep damage, 0.008759,

0.189305 and 0.459618, respectively denoted as the cases A, B, and C listed in Table 5.5; and the five dashed lines, denoted by c0, c1, c2, c3 and c4, indicate different creep damage constraints.

As seen in Fig. 5.26, the performance penalty increases and the creep damage accumulation decreases by making the damage constraint more tight for a given initial damage. On the other hand, both the performance penalty and the creep damage accumulation increase for a given damage constraint if the initial damage is larger. In essence, the engine performance is degraded if the service life of the coolant channel ligament is extended by tightening the damage constraint, or if the same constraints are used for a larger initial damage. However, the system performance is optimized for the given constraints and initial damage even though the performance may be degraded.

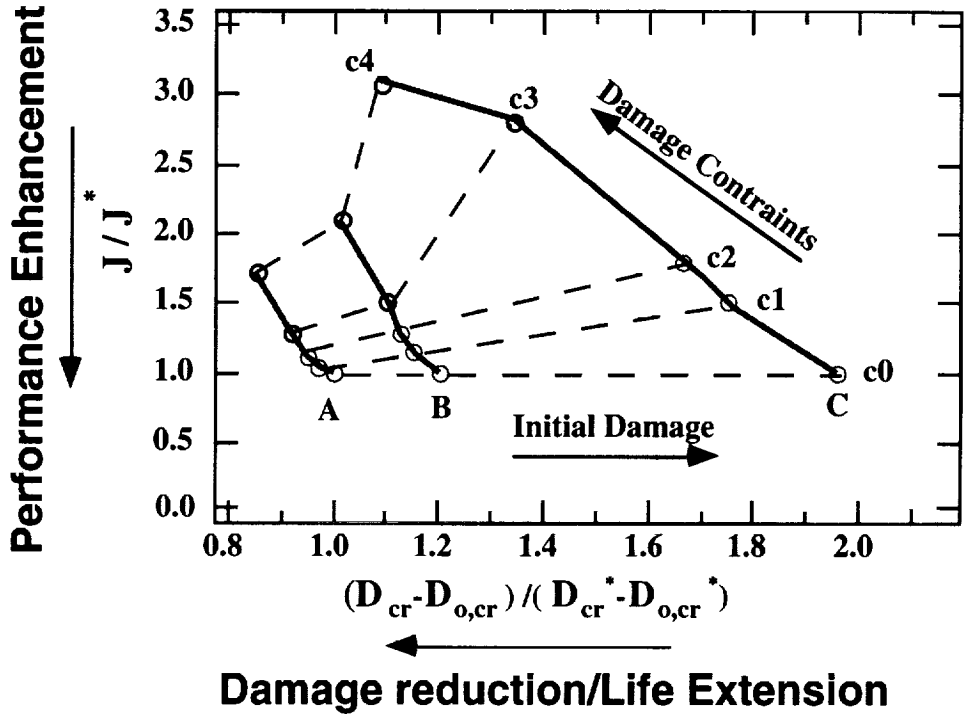

Fig. 5.26 Optimization results of performance vs. damage reduction/life extension

Each point, denoted by a circle in Fig. 5.26 corresponds to the optimal open-loop solutions (i.e., optimal trajectories of control valve actions $\{\mathbf{u}_k\}$, and transients of plant state and output variables $\{\mathbf{x}_k\}$and $\{\mathbf{y}_k\}$) for a given initial creep damage and constraints on the coolant channel ligament for the engine acceleration from the initial state of 2700 psi to the final state of 3000 psi. This optimal law for feedforward control of the up-thrust transients can be formulated, for a predicted initial creep damage in terms of the user-specified creep damage constraints. These constraints, in turn, can be selected based on the mission objectives, service life, performance, and maintenance and operational costs. For example, for meeting the mission objectives, if the system performance is more critical than extension of the service life, then the creep damage constraints may have to relaxed for an older engine. On the other hand, for reduction of the engine life cycle cost, if a small sacrifice in the engine performance can be allowed, then the creep damage constraints should be made more stringent as the engine becomes older.

5.5 Simulation of the Damage Mitigating Control System on a Testbed

The feedforward control policy is generated in Section 5.2 to achieve optimal performance of the rocket engine based on a nominal model of plant and damage dynamics. However, because of modeling uncertainties, sensor noise and external disturbances, the actual response will deviate from nominal trajectory when the plant is excited by the sequence of the feedforward control commands. Therefore, a feedback control system can be used to compensate for these deviations. A robust output feedback controller has been synthesized to maintain the trajectories of the plant output variables close to the respective nominal trajectories.

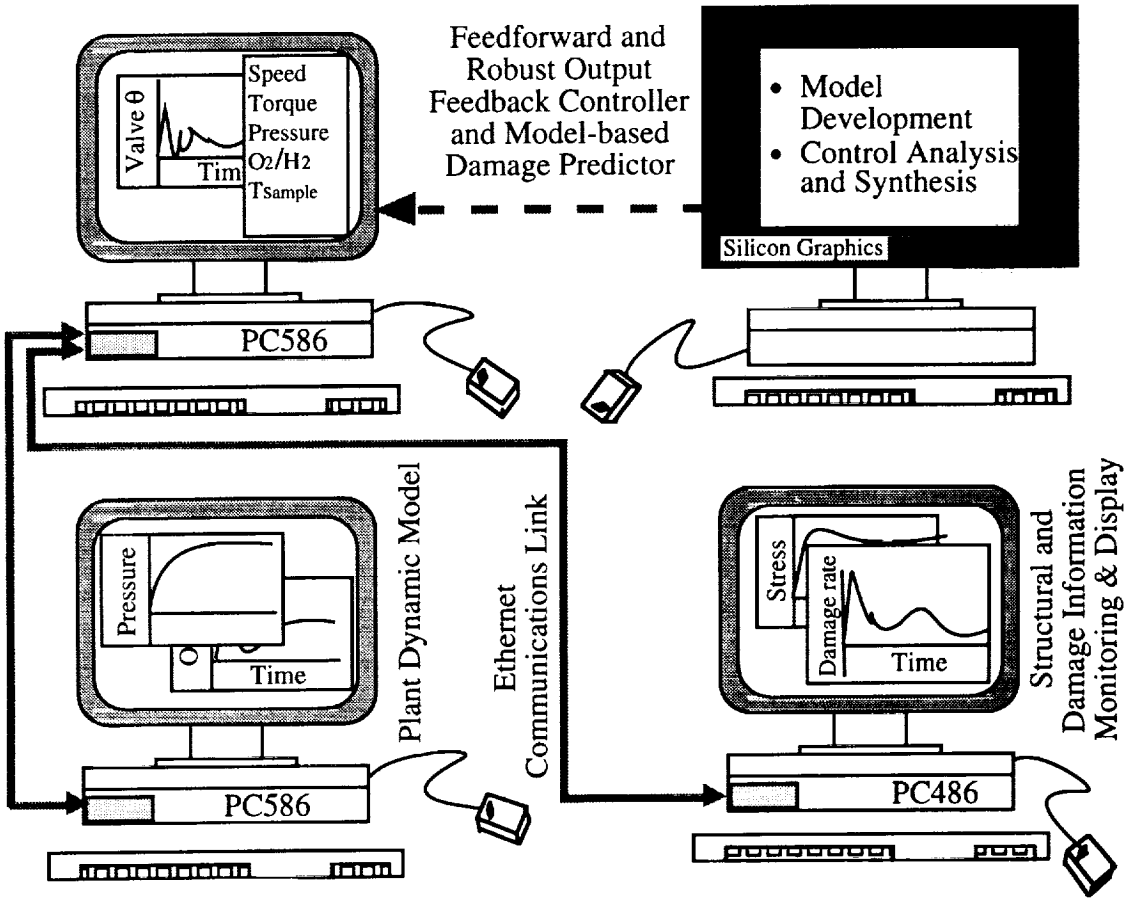

Fig. 5.27 Schematic diagram of the simulation testbed operations

A simulation testbed has been established for evaluation of damage mitigating control systems. The testbed, at this stage, consists of an Silicon Graphics (SGI) Indigo R-4000 workstation, two 586-based and one 486-based PCs which are interconnected via ethernet as shown in Fig. 5.27. The SGI workstation has been used for off-line computations that include model development of both plant and structural & damage dynamics, and analysis and synthesis of both feedforward and robust feedback control policies via nonlinear programming and μ-synthesis (Packard and Doyle, 1993), respectively. The 20th nonlinear plant dynamic model of the rocket engine is simulated on one of the PC-586s, which serves as the real plant. Both the feedforward control policy and the linear robust output feedback control policy are implemented in the second PC-586 along with the analytical structural and life prediction models of the critical components (i.e., fuel and oxidizer turbine blades and main thrust chamber coolant wall). This software for on-line life prediction and control is portable to other machines. All three machines serve as display devices of the selected process and damage variables.

CHAPTER 6

SUMMARY, CONCLUSIONS, AND RECOMMENDATIONS FOR FUTURE WORK

This report investigates the feasibility of damage mitigating control of reusable rocket engines where the objective is to achieve optimized trade-off between the system performance and structural durability. Summary and conclusions of this interdisciplinary research are presented in Section 6.1. Future research for transfer of this space technology to the electric power industry is recommended in Section 6.2.

6.1 Summary and Conclusions

A unified methodology has been proposed for analysis and synthesis of damage mitigating control systems for rocket engines by integrating the disciplines of thermo-fluid dynamics, mechanical structures, and mechanics of materials along with control and optimization of dynamic systems. Research work in each of these disciplines are summarized and concluded in Sections 6.1.1 to 6.1.3.

6.1.1 Plant Dynamic Model of a Reusable Rocket Engine

Plant dynamics of a rocket engine which is similar to the Space Shuttle Main Engine (SSME) have been modeled in Chapter 2 is to represent its steady-state and dynamic characteristics for damage prediction and synthesis of a damage mitigating control policy. The 20th order, nonlinear, time-invariant and deterministic model is formulated in the state-space form, and numerical results are obtained by digital simulation.

Steady-state model results agree closely with those of a more detailed nonlinear model of the SSME reported by Rockwell (1989). Transient responses of the nonlinear plant model are obtained at the full load by initiating independent step disturbances in two input variables. The results show that the two control input valves, FPOV and OPOV, have significant effects on O_2 / H_2 mixture ratio and chamber pressure as discussed by Musgrave (1990). In particular, the chamber pressure is affected to a much greater extent due to the step change in the FPOV than that due to the OPOV. These results are useful for:

(i) Understanding the complex and highly interactive process dynamics;
(ii) Providing the process variables (i.e., turbopump speed and torque, wall temperature and pressure loading) for damage prediction in the critical plant components; and
(iii) Investigating both feedforward and feedback system dynamic performance under various operating conditions.

These results can also be used for prediction of potential operational and control problems of reusable rocket engines.

6.1.2 Structural and Damage Model of the Combustion Chamber Wall

This report presents the development of a creep damage model in the coolant channel ligament of the main thrust chamber during transient operations of a reusable rocket engine such as the SSME. This damage model is based upon the theories of sandwich beam and viscoplasticity. The modeling approach consists of analyzing the incremental bulging-out and progressive thinning of the ligament in each firing cycle by taking the effects of geometric deformation into consideration.

A structural and damage model of the coolant channel wall for the main thrust chamber has been analytically derived and subsequently validated in terms of single-cycle and multi-cycle stress-strain behavior by comparison with finite element models and experimental data for two different materials, namely, OFHC copper and NARloy-Z. The predicted results are in agreement with those obtained from the finite element analyses and experimental observations.

The close agreement with the finite element models indicates that the proposed life prediction model can capture the failure mechanics (i.e., creep rupture) of the main thrust chamber wall by calculating the mid-plane deflection of the ligament. This model has been proven to be numerically much more efficient than the finite element model with comparable accuracy. Validation of this model for both NARloy-Z and OFHC copper materials and its numerical efficiency establish its credibility for on-line life prediction and damage mitigating control of a rocket engine for which the finite-element model is not appropriate. To the best of the author's knowledge, the proposed life prediction model is the only available model which is suitable for both on-line life prediction and damage mitigating control.

The predicted life of the coolant channel wall is influenced by several factors including the ligament material, configuration and design of the channel, chamber pressure, wall temperature, and loading cycle duration. These effects have been investigated through parametric studies, and the following conclusions are derived:

1. The failure phenomena, regardless of whether the material is OFHC copper or NARloy-Z, are characterized by thinning of the center of the ligament. An OFHC copper ligament is potentially more prone to damage because the thinout process accelerates leading to an abrupt rupture. NARloy-Z materials show an improvement in cyclic life over the OFHC copper material at a given thermo-mechanical loading. The deformation of an OFHC copper chamber is predicted to be larger than for that for a less ductile NARloy-Z chamber, which is in agreement with experimental observations.

2. Increasing the number of coolant channels is one of the feasible approaches to life extension of the main thrust chamber.

3. The pressure difference across the coolant channel ligament is a cause of the bulging-out phenomenon, and the ligament thinning increases with the pressure difference.

4. Decreasing the coolant wall temperature is a possible solution to reduce thinning of the main thrust chamber wall. The thermally induced bending resulting from temperature difference across the ligament tends to retard the bulging out process due to the pressure loading, and therefore improves the service life of the main thrust chamber, especially for the OFHC copper material.

5. The magnitude of the bulging-out and thinning of the coolant channel ligament of both OFHC copper and NARloy-Z materials is depended on the duration of the loading cycle. The bulging out process is more pronounced for the extended cycle than for the short loading cycle.

6.1.3 Integrated Life Extension and Control Synthesis

The benefits derived from damage mitigating control of reusable rocket engines, as presented in this report, are summarized below:

- Maximum system performance of rocket engines can be achieved with increased durability of the mechanical structures such that functional lives of critical components are increased.

- On-line life prediction and damage mitigation, based on the available sensory and operational information, will allow reusable rocket engines to be inexpensively maintained, and safely and efficiently steered under diverse operating conditions.

The feasibility of applying this control concept to rocket engines such as the SSME has been investigated in view of fatigue and creep damage in three critical components, namely, the fuel turbine, the oxidizer turbine, and the main thrust chamber. Based on the fatigue damage model and the proposed creep damage model, an optimal feedforward policy has been synthesized for open loop control of up-thrust transients of the rocket engine under the damage constraints on the above three critical components.

The results of optimization studies demonstrate the interactive nature of fatigue damage in the fuel and oxidizer turbine blades, and creep damage in the coolant channel ligament of the main thrust chamber. The damage accumulation in both coolant channel ligament and turbine blades are seen to be significantly influenced by their respective constraints and initial damage. It is observed that the initial damage in the critical components may have a significant impact on service life extension of rocket engines. Therefore, in the synthesis of the control policy, both the constraints and performance cost function need to be selected based on the knowledge of the initial damage in the critical components.

Up-thrust transients of the rocket engine have been simulated for a brief period of 300 ms. Complete operations of a reusable rocket engine over its life include many such transients, and the steady-state operation in a single flight may last for several hundreds of seconds. Although both fatigue and creep damage rates during the steady state are smaller than those during transient operations, the total damage accumulation during steady state operations may not be insignificant. Therefore, during one flight of a reusable rocket engine, the cumulative effects of both transient and steady state operations need to be considered for estimation of total damage accumulation. The optimization studies presented in this report only consider a single point in each of the three critical components. Simultaneous control of damage at several other critical points in the rocket engine might be necessary for damage mitigation and life extension. However, this will make the optimization problem more complex as the dimension of the damage vector will be large compared to the three-dimensional damage vector in the present study.

6.2 Recommendations for Future Work

The concept of damage mitigation, presented in this report, is not restricted to control of rocket engines. It can be applied to any system where structural durability is an important issue. Besides rocket engines, applications of damage mitigating control include a wide spectrum of engineering applications such as fossil and nuclear plants for electric power generation, rotating and fixed wing aircraft, automotive and truck engine/transmission systems, and large rolling mills. In each of these systems, damage mitigating control can enhance safety and productivity accompanied by reduced life cycle cost.

For example, the availability of power plants often suffers from premature failures of steam generator tubes (due to corrosion-fatigue and creep), main steam and reheater steam pipelines (due to creep and fatigue), condenser tubes (due to stress corrosion cracking and flow-induced vibration) and low pressure turbine blades (due to stress corrosion, erosion, and fatigue). A continuous-time damage model will allow timely warnings of these failures, and the resulting decision and control actions may not only avoid an early shutdown but also improve maintainability. A more complex application of the damage mitigation concept is start-up and scheduled shutdown of power plants, and take-off and landing of commercial aircraft, in which the damage information can be utilized for real-time plant control either in the fully automated mode or with human operator(s) in the loop.

The concept of damage mitigating control is of significant importance to power and processing plants. Many components such as steam generators in conventional power and processing plants are exposed to high loads at elevated temperatures, and have been in use beyond the design life of 30 to 40 years. Several preliminary investigations have shown that the cost of life extension of a typical fossil power plant may be only 20 to 30 percent of that of a new construction (Viswanathan, 1989). Therefore, the concept of damage mitigating control is ideally suited to life extension of aging power plants under both steady state and transient operations. The objective is to enhance plant performance, availability and maintainability while simultaneously reducing the structural damage to avoid unscheduled plant shutdown and repair as much as possible. This objective can be achieved via transfer of the technology of damage mitigating control for the rocket engines to power plant applications.

REFERENCES

Allen, D.H. and Beek, J.M., 1984, "On the Use of Internal State Variables in Thermoviscoplastic Constitutive Equations," Symposum on Nonlinear Constitutive Relations for High Temperatur*e Application*, NASA Lewis Research Center, June 15-17, pp. 83-101.

Armstrong, W.H., 1979, "Structural Analysis of Cylindrical Thrust Chamber," *Final Report, Volume* I, *NASA CR-159552*, Contract NAS3-21361, NASA Lewis Research Center, March.

Armstrong, W.H., 1981, "Structural Analysis of Cylindrical Thrust Chamber," *Final Report, Volume* II, *NASA CR-165241*, Contract NAS3-21953, NASA Lewis Research Center, March.

Arnold, S.M., Robinson, D.N. and Saleeb, A.F., "Creep Buckling of Cylindrical Shell Under Variable Loading," *Journal of Engineering Mechanics*, V115, No. 5, May-August,, pp. 1054-1075

Arya, V.K., 1992, "Nonlinear Structural Analysis of Cylindrical Thrust Chambers Using Viscoplastic Models," *Journal of Propulsion and Power*, Vol. 8, No. 3, May-June, pp. 598-604.

Arya, V.K. and Arnold, S.M., 1992, "Viscoplastic Analysis of an Experimental Cylindrical Thrust Chamber Liner," *AIAA Journal*, Vol. 30, No. 3, March, pp. 781-789.

Blackburn, J.F., Reethof, G. and Shearer, J.L., 1960, *Fluid Power Control*, The technology press of Massachusetts Institute of Technology, Dynamic Analysis and Control Laboratory.

Chen, K.S., Lindholm, U.S., Bodner, S.R. and Walker, K.P., 1984, "A Survey of Unified Constitutive Theories," *Symposum on Nonlinear Constitutive Relations for High Temperature Application*, 1984, NASA Lewis Research Center, Ohio, June 15-17, pp. 1-23.

Dai, X. and Ray, A., 1994a, "Damage-Mitigating Control of a Reusable Rocket Engine, Part 1: Life Prediction of the Combustion Coolant Wall," *ASME Winter Annual Meeting*, Chicago, November, and to be published in *Journal of Dynamic Systems, Measurement and Control., Trans. ASME.*

Dai, X. and Ray, A., 1994b, "Damage-Mitigating Control of a Reusable Rocket Engine, Part 2: Formulation of an Optimal Control Policy and Simulation," *ASME Winter Annual Meeting*, Chicago, November, and to be published in *Journal of Dynamic Systems, Measurement and Control., Trans. ASME.*

Duyar, A., Guo, T-H. and Merrill, W.C., 1990, "Space Shuttle Main Engine Model Identification," *IEEE Control System Magazine*, Vol. 10, No. 4, pp. 59-65.

Duyar, A., Eldem, V., Merrill, W.C., and Guo, T-H., 1991, "State Space Representation of the Open-Loop Dynamics of the Space Shuttle Main Engine," *Journal of Dynamic Systems, Measurement, and Control, Trans. ASME.*, December, Vol. 113, pp. 684-690.

Freed, A.D., 1988, "Structure of a Viscoplastic Theory," NASA TM-100749, Lewis Research Center, Cleveland, Ohio, Prepared for the Summer Annual Meeting Symposium: *Constitutive Equations and Life Prediction Models for High Temperature Applications*, sponsored by ASME, Berkeley, California, June 20-22.

Freed, A.D. and Verrilli, M.J., 1988, "A viscoplastic Theory Applied to Copper," NASA TM-100831, Lewis Research Center, prepared for the International Seminar on *The Inelastic Behavior of Solids Models and Utilization*, Sponsored by MECAMAT, Besancon, France, August 30 - September 1.

Gill, P.E., Murray, W., Saunders, M.A. and Wright, M.H., 1991, *NPSOL Version 4.06*, Software Distribution Center, Stanford University, Palo Alto, CA.

Hannum, N. P., Kasper, H.J. and Pavli, A.J., 1976, "Experimental and Theoretical Investigation of Fatigue Life in Reusable Rocket Thrust Chambers," *NASA TM X-73413*, Lewis Research Center, July.

Kasper, H.J., 1984, "Thrust Chamber Life Prediction", *NASA Conference Publication 2372, Advanced high pressure O2/H2 technology*, Proceedings of a conference held at George C. Marshall Flight Center, Huntsville, Alabama, June 27-29, pp. 36-43.

Lorenzo, C.F. and Merrill, W.C., 1991a, "Life Extending Control: A Concept Paper," *American Control Conference*, Boston, MA, June, pp. 1080-1095.

Lorenzo, C.F. and Merrill, W.C., 1991b, "An Intelligent Control System for Rocket Engines: Need, Vision, and Issues," *Control Systems Magazine*, Vol. 12, No. 1. January, pp. 42-46.

Luenberger, D.G., 1984, *Linear and Nonlinear Programming*, 2nd edition, Reading, Mass., Addison-Wesley, Menlo Park, CA.

McDowell, D.L., 1992, "A Nonlinear Kinematic Hardening Theory for Cyclic Thermoplasticity and Thermoviscoplasticity," *International Journal of Plasticity*, Vol. 8, pp. 695-728.

Musgrave, J.L., 1990, "Advanced Control Modes for Space Shuttle Main Engine," *Conference on Advanced Earth-to Orbit Propulsion,* Technology held at NASA George C. Marshall Space Flight Center, Marshall Space Flight Center, Alabama, May 15-17.

Noll, T., Austin, E., Donley, S., Graham, G., Harris, T., Kaynes, I., Lee, B. and Sparrow, J., 1991, "Impact of Active Controls Technology on Structural Integrity," *32nd AIAA/ASME/ASCE/AHS/ASC Structures, Structural Dynamics, and Materials Conference*, Baltimore, MD, April, pp. 1869-1878.

Packard, A. and Doyle, J., 1993, "The Complex Structured Singuler Value," *Automatica*, Vol 29. No. 1, pp. 71-109.

Paris, P.C., and Erdogan, F., 1963, "A Critical Analysis of Crack Propagation Laws," *Journal of Basic Engineering, Trans. ASME,* Vol. D85, pp. 528-534.

Porowski, J.S., O'Donnell, W.J., Badlani, M.L. and Kasraie, B., 1985, "Simplified Design and Life Prediction of Rocket Thrust Chambers," *Journal of Spacecraft,* 1985, Vol. 22, March-April, pp. 181-187.

Pugh, C.E. and Robinson, D.N., 1978, "Some Trends in Constitutive Equation Model Development for High-Temperature Behavior of Fast-Reactor Structural Alloys," *Journal of Nuclear Engineering and Design*, Vol. 48, pp. 269-276.

Quentmeyer, R.J., 1977, "Experimental Fatigue Life Investigation of Cylindrical Thrust Chambers," *NASA TM X-73665*, Lewis Research Center, July 1977.

Ray, A., 1976, *Mathematical Modeling and digital Simulation of a Commercial Scale High Temperature Gas-Cooled Reactor (HTGR) Stream Power Plant*, Ph.D. Dissertation in Mechanical Engineering, Northeastern University, Boston, Massachusetts, June.

Ray, A. and H. F. Bowman, 1978, "Digital Simulation of a High Temperature Gas-Cooled Reactor (HTGR) Steam Power Plant," *IEEE Trans. on Nuclear Science*, August, pp. 1068-1077.

Ray, A., Wu, M-K., Carpino, M., Lorenzo, C., F., 1994a, "Damage-Mitigating Control of Mechanical Systems: Part I - Conceptual Development and Model Formulation," *Journal of Dynamic Systems, Measurement, and Control, Trans. ASME*, Vol. 116, September, pp. 437-447.

Ray, A., Wu, M-K., Carpino, M., Lorenzo, C., F., 1994b, "Damage-Mitigating Control of Mechanical Systems: Part II - Formulation of an Optimal Policy and Simulation," *ASME Journal of Dynamic Systems, Measurement, and Control, Trans. ASME*, Vol. 116, September, pp. 448-455.

Ray, A., Dai, X., Wu, M-K., Carpino, M., Lorenzo and C., F., 1994c, "Damage-Mitigating Control of a Reusable Rocket Engine," *Journal of Propulsion and Power,* Vol. 10, No. 2, March-April, pp. 225-234.

Ray, A., Dai, X., Wu, M-K., Carpino, M., Lorenzo and C. F., 1994d, "Damage-Mitigating Control – An Interdisciplinary Thrust between Controls and Material Science," *American Control Conference*, Baltimore, MD, June-July, pp. 3449-3453.

Ray, A. and Wu, M-K., 1994a, "Damage Mitigating Control of Space Propulsion Systems for High Performance and Extended Life," *NASA CR-194470*, Grant NAG3-1240, NASA Lewis Research Center, March.

Ray, A. and Wu, M-K., 1994b "Fatigue Damage Control of Mechanical Systems," *SMART Materials and Structures*, Vol. 3, No. 1, March, pp. 47-58.

Robinson, D.N. and Swindeman, R.W., 1982, "Unified Creep-Plasticity Constitutive Equations For 2-1/4 Cr-1 Mo Steel At Elevated Temperature," *ORNL/TM - 8444*, Contract No. W-7405-eng-26, October.

Robinson, D.N.and Arnold, S.M., 1990, "Effects of State Recovery on Creep Buckling Under Variable Loading," *Journal of Applied Mechanics, Trans. ASME*, Vol. 57, June, pp. 313-320.

Rockwell International Corporation, 1989, "Engine Balance and Dynamic Model," *Report FSCM No. 02602,* Spec, No. RL00001. Revised version 1.5.

Stubstad, J.M. and Simitses, G.J., 1987, "Creep Analysis of Beams and Arches Based on A Hereditary Visco-Elastic-Plastic Constitutive Law," *Constitutive Modeling for Engineering Materials With Applications*. Vol. 153, pp. 1-15. 1987.

Sutton, G., P., 1992, *Rocket Propulsion Elements, an introduction to the engineering of rockets*, 6th edition, Wiley Interscience, New York, 1992.

Swain, M.H., Everett, R.A., Newman, J.C., Jr. and Phillips, E. P., 1990, "The Growth of Short Cracks in 4340 Steel and Aluminum-Lithium 2090," *AGARD Report, No. 767*, pp. 7.1-7.30.

Vidyasagar, M., 1992, *Nonlinear Systems Analysis*, 2nd ed., Prentice Hall, Englewood Cliffs, NJ.

Viswanathan, R., 1989, "Damage Mechanisms and Life Assessment of High-Temperature Components", *ASM International*, Metals Park, Ohio 44073.

REPORT DOCUMENTATION PAGE

Form Approved
OMB No. 0704-0188

1. AGENCY USE ONLY (*Leave blank*)	2. REPORT DATE	3. REPORT TYPE AND DATES COVERED
	January 1995	Final Contractor Report

4. TITLE AND SUBTITLE
Damage-Mitigating Control of a Reusable Rocket Engine for High Performance and Extended Life

5. FUNDING NUMBERS
WU-505-62-50
G-NAG3-1240

6. AUTHOR(S)
Asok Ray and Xiaowen Dai

7. PERFORMING ORGANIZATION NAME(S) AND ADDRESS(ES)
The Pennsylvania State University
Mechanical Engineering Department
University Park, Pennsylvania 16802

8. PERFORMING ORGANIZATION REPORT NUMBER
E-9336

9. SPONSORING/MONITORING AGENCY NAME(S) AND ADDRESS(ES)
National Aeronautics and Space Administration
Lewis Research Center
Cleveland, Ohio 44135-3191

10. SPONSORING/MONITORING AGENCY REPORT NUMBER
NASA CR-4640

11. SUPPLEMENTARY NOTES
Project manager, Carl F. Lorenzo, Instrumentation and Control Technology Division, NASA Lewis Research Center, organization code, 2500, (216) 433-3733.

12a. DISTRIBUTION/AVAILABILITY STATEMENT
Unclassified - Unlimited
Categories 26 and 31

This publication is available from the NASA Center for Aerospace Information, (301) 621-0390.

12b. DISTRIBUTION CODE

13. ABSTRACT (*Maximum 200 words*)

The goal of damage mitigating control in reusable rocket engines is to achieve high performance with increased durability of mechanical structures such that functional lives of the critical components are increased. The major benefit is an increase in structural durability with no significant loss of performance. This report investigates the feasibilty of damage mitigating control of reusable rocket engines. Phenomenological models of creep and thermo-mechanical fatigue damage have been formulated in the state-variable setting such that these models can be combined with the plant model of a reusable rocket engine, such as the Space Shuttle Main Engine (SSME), for synthesizing an optimal control policy. Specifically, a creep damage model of the main thrust chamber wall is analytically derived based on the theories of sandwich beam and viscoplasticity. This model characterizes progressive bulging-out and incremental thinning of the coolant channel ligament leading to its eventual failure by tensile rupture. The objective is to generate a closed form solution of the wall thin-out phenomenon in real time where the ligament geometry is continuously updated to account for the resulting deformation. The results are in agreement with those obtained from the finite element analyses and experimental observation for both Oxygen Free High Conductivity (OFHC) copper and a copper-zirconium-silver alloy called NARloy-Z. Due to its computational efficiency, this damage model is suitable for on-line applications of life prediction and damage mitigating control, and also permits parametric studies for off-line synthesis of damage mitigating control systems. The results are presented to demonstrate the potential of life extension of reusable rocket engines via damage mitigating control. The control system has also been simulated on a testbed to observe how the damage at different critical points can be traded off without any significant loss of engine performance. The research work reported here is built upon concepts derived from the disciplines of Controls, Thermo-fluids, Structures, and Materials. The concept of damage mitigation, as presented in this report, is not restricted to control of rocket engines. It can be applied to any system where structural durability is an important issue.

14. SUBJECT TERMS	15. NUMBER OF PAGES
Life extending control; Damage modeling; Creep; Creep ratcheting; Fatigue; Optimization	85
	16. PRICE CODE A05

17. SECURITY CLASSIFICATION OF REPORT	18. SECURITY CLASSIFICATION OF THIS PAGE	19. SECURITY CLASSIFICATION OF ABSTRACT	20. LIMITATION OF ABSTRACT
Unclassified	Unclassified	Unclassified	

National Aeronautics and
Space Administration

Lewis Research Center
21000 Brookpark Rd.
Cleveland, OH 44135-3191